creative commons
COMMONS DEED

저작자표시-비영리-변경금지 2.0 대한민국

이용자는 아래의 조건을 따르는 경우에 한하여 자유롭게

- 이 저작물을 복제, 배포, 전송, 전시, 공연 및 방송할 수 있습니다.

다음과 같은 조건을 따라야 합니다:

저작자표시. 귀하는 원저작자를 표시하여야 합니다.

비영리. 귀하는 이 저작물을 영리 목적으로 이용할 수 없습니다.

변경금지. 귀하는 이 저작물을 개작, 변형 또는 가공할 수 없습니다.

- 귀하는, 이 저작물의 재이용이나 배포의 경우, 이 저작물에 적용된 이용허락조건을 명확하게 나타내어야 합니다.
- 저작권자로부터 별도의 허가를 받으면 이러한 조건들은 적용되지 않습니다.

저작권법에 따른 이용자의 권리는 위의 내용에 의하여 영향을 받지 않습니다.

이것은 이용허락규약(Legal Code)을 이해하기 쉽게 요약한 것입니다.

Disclaimer

dCollection

공학박사 학위논문

Multifunctional Cell-Culture-Platforms Integrated with Soft Electronics for Electrophysiological Applications

2017년 8월

유연 전자 소자가 융합된 다기능성 세포 배양 기판 개발과 전기생리학적 활용

서울대학교 대학원

화학생물공학부 에너지환경화학융합기술전공

김 석 주

Multifunctional Cell-Culture-Platforms Integrated with Soft Electronics for Electrophysiological Applications

지도 교수 김 대 형

이 논문을 공학박사 학위논문으로 제출함
2017 년 7 월

서울대학교 대학원
화학생물공학부 에너지환경화학융합기술전공
김 석 주

김석주의 공학박사 학위논문을 인준함
2017 년 7 월

위 원 장 _____ (인)

부위원장 _____ (인)

위 원 _____ (인)

위 원 _____ (인)

위 원 _____ (인)

Abstract

Multifunctional Cell-Culture-Platforms Integrated with Soft Electronics for Electrophysiological Applications

Seok Joo Kim

School of Chemical and Biological Engineering

Chemical Convergence for Energy & Environment

The Graduate School

Seoul National University

Compared to conventional electronic devices, soft electronics offer the proper mechanical properties similar to native tissues and cells. This feature provides not only the promotion of cellular activities during culturing cells *in vitro*, but also the enhancement of biological interfaces between soft electronics and curvilinear surfaces of target organs *in vivo*. The high-quality interface enables effective monitoring and stimulation of electrophysiological signals. In this thesis, fabrications of three types of cell-culture-platforms and

those applications are introduced. Components of all electronics are fabricated based on soft nanomaterials such as inorganic or carbon nanomaterials, and those electronics are transferred onto a biocompatible polymer substrate.

Firstly, soft cell-culture-platform is designed to prepare C2C12 myoblasts sheet for transfer printing and treating the damaged muscle tissue. The platform is instrumented with stretchable nanomembrane sensors for *in situ* monitoring of cellular physiological characteristics during proliferation and differentiation, and with graphene nanoribbon cell aligners for guiding the unidirectional orientation of plated cells, whose system modulus is matched with target tissues. Furthermore, a high-yield transfer printing mechanism can deliver cell sheets for scaffold-free, localized cell therapy *in vivo*.

Secondly, multifunctional cell-sheet-graphene hybrid is developed as stretchable and transparent medical device, which can be implanted *in vivo* to form a high-quality biotic/abiotic interface. The hybrid is composed of C2C12 myoblasts sheet on buckled, mesh-patterned graphene electrodes. The graphene electrodes monitor and stimulate the C2C12 myoblasts *in vitro*, serving as a smart cell culture substrate that controls their aligned proliferation and differentiation. This stretchable and transparent cell-sheet-graphene hybrid can be transplanted onto the target muscle tissue, record

electromyographical signals, and stimulate implanted sites electrically and/or optically *in vivo* without any immune responses. Additional cellular therapeutic effect of the cell-sheet-graphene hybrid is obtained by the integrated C2C12 myobalsts sheet.

Finally, electronic-cell-culture-platform is fabricated to provide multifunctionalities by integrating various types of electronics for monitoring and stimulating important metabolic conditions of culturing cells. This platform is based on an array of soft electronics composed of four types of sensors and two types of stimulators, which is transferred onto a biocompatible polymer substrate designed by a 3D printer. The sensors and stimulators can monitor and regulate the behaviors and activities of the cells cultured on the large area surface of the platform. The multi-layer system of the platform enable to monitor and stimulate the activities of numerous cells effectively without sacrificing any culturing cells.

Keywords: flexible, stretchable, electronic device, cell-culture-platform, graphene, transfer printing, cell therapy

Student Number: 2012-31298

Contents

List of Figures

List of Table

Chapter 1. Introduction

1.1 Soft electronics for cell culturing *in vitro*

Development in electronic devices that serve as a platform for culturing cells has been dramatically increased with the recent advancement in semiconductor industry. In previous studies, multielectrode array (MEA) system was fabricated with inorganic materials (*i.e.,* gold, platinum, etc.) deposited onto Si wafer or glass substrate.[1] This electrode system enabled to monitor and/or stimulate cellular activities of neurons[1,2] or cardiomyocytes,[3,4] where these types of cells have been widely utilized due to their unique electrophysiological properties (**Figure 1.1**). Recently, an advanced microelectronics has been integrated for the analysis and control of the culturing cells.[5-7] For example, two metal electrodes reside next to each other detect the changes of impedance during cellular proliferation or differentiation,[5,6] and antibody conjugated silicon nanowire electrode can detect cancer-derived small molecules.[7] Additionally, the integration of transistor and MEA that are made of high-performance single crystalline silicon can offer the new technology in high-density electrode system for

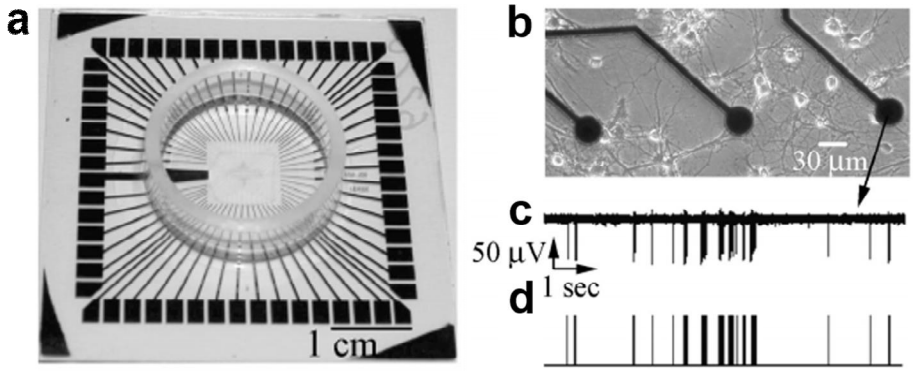

Figure 1.1 Neuronal cells cultured on multielectrode arrays (MEAs)

(a) Photographic image of multielectrode array. (b) Microscopic image of neuronal cells cultured on the multielectrode arrays. (c) Signal of electrophysiological activity from neuronal cells and (d) its raster plot measured by an electrode of the multielectrode array.

monitoring the culturing cells.[8,9] These types of electronic devices, however, have been fabricated conventionally with the rigid inorganic materials.[10,11] Therefore, the cells that are sensitive to the mechanical property[12,13] have limitations for culturing on these types of platforms. Also, these substrates have limitation to be utilized as implantable tissue-engineered scaffold since biocompatibilities of materials for electronic devices are not proved sufficiently.[14]

Recently, developments in soft electronics for bioengineering researches have been drastically increased, in which the flexible[15-17] and stretchable[18,19] electronics may solve the issues in conventional rigid devices. The soft electronics can be widely used in culturing cells for the following issues: i) many different types of electronics are integrated for electrophysiological applications, ii) the structure of electrode is deformed three-dimensionally due to its softness, iii) additional functions are easily added by functional nanomaterials. In past, the flexible and stretchable electronics were usually fabricated using inorganic metal nanomembrane deposited into sub-micron scale with sputter or thermal evaporator and patterned with photolithography into serpentine pattern.[18-20] On the other hand, silicon nanowire[21], organic materials,[15-17,22] graphene,[23,24] and carbon nanotube[25] that are intrinsically soft materials are also utilized for fabricating

flexible and stretchable electronics (**Figure 1.2**). Specifically, high-performance and biocompatible materials are essential in developing advanced soft electronics for bioengineering field.

In this thesis, the fabrication of multifunctional cell-culture-platform with the integration of high-performance electronics and biocompatible substrates will be described. In chapter 2 and 3, impedance sensors made of gold nanomembrane and graphene, respectively, have been transferred onto biocompatible polydimethylsiloxane (PDMS) to fabricate soft and transparent cell-culture-platforms. In chapter 4, various types of electrical/electrochemical sensor and stimulator array made of inorganic materials are transferred onto biocompatible polylactic acid (PLA) substrate for the fabrication of advanced and multifunctional cell-culture-platform.

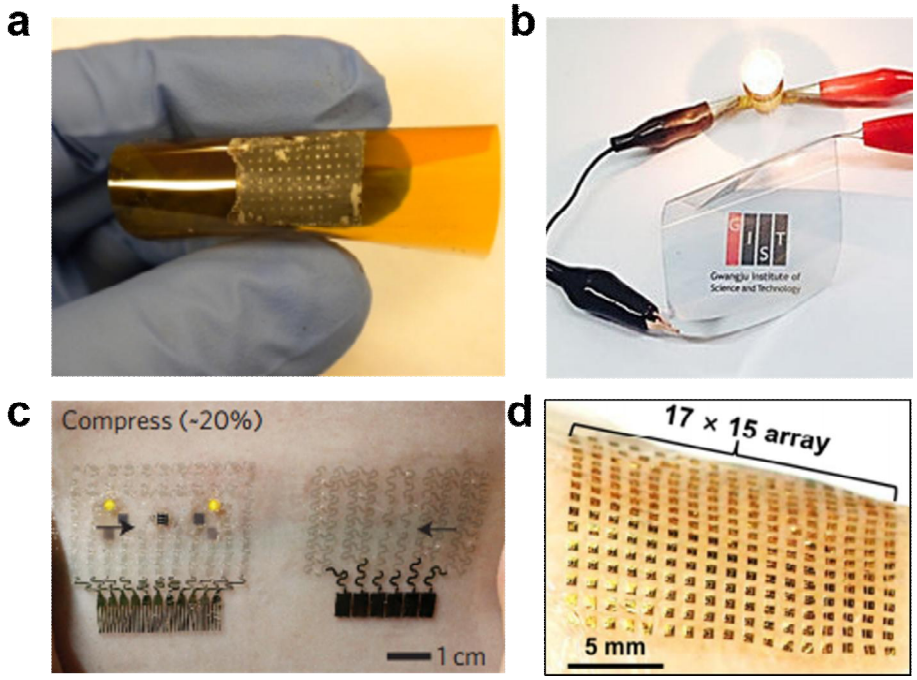

Figure 1.2 Photographic images of soft electronics fabricated using various types of materials

(a) Vertical p-n silicon nanowire array electrodes. (b) PEI/Ag/PEDOT:PSS electrode arrays. (c) Stretchable graphene electrode for biomedical applications. (d) Flexible and wearable flash memory fabricated using carbon nanotubes.

1.2 Biointerfaces of soft electronic devices

To form a high-quality interaction between cells and the substrate, the cells have to recognize the microenvironments including structure and topology of the biocompatible materials and secrete the adhesive extracellular matrix (ECM) protein.[26] Mimicking the features of the native tissue including mechanical and biological properties, therefore, is important issues for the development of multifunctional substrate for culturing cells in order to promote the cellular activities during culturing cells.[27,28] Recently, the changes of cellular activities according to the various types of nanomaterials used in electronic devices including inorganic,[29] organic,[30] and carbon nanomaterials[31-33] have been widely studied by increasing cellular physiological applications of soft electronics.

Furthermore, the cytoskeletal orientation of cells by the micro- or nano-topology of substrate materials have been also regarded as the important cues for guiding cellular activity.[28,34] To encompass these cues into a cell-culture-platform, manipulation of substrate topology[28,34] and ECM protein coating *via* PDMS stamp[35] or chemical conjugation[36] are possible ptions (**Figure 1.3)**. However, these techniques are limited due to the harsh

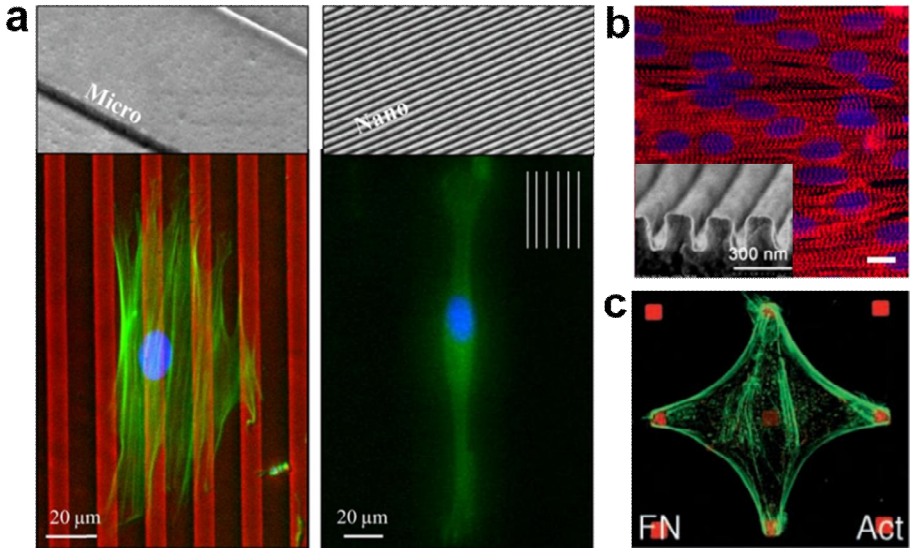

Figure 1.3 Cues for guiding cellular alignments

(a) Microscopic images of cellular alignment according as micro- and nano-topologies of substrates. (b) Anisotropic alignments of confluent neonatal rat cardiomyocytes on sub-micron-patterned wafer substrate. (c) Manipulation of cellular alignments by regulation of protein arrays by PDMS stamp.

environment where acid, base, and organic solvent are prevalent during the fabrication process of electronic devices. Cell-electronics interface has been also promoted through the cell membrane penetration with vertically grown silicon nanowire[37,38] or carbon nanotube[39] which leads, however, to cellular damages (**Figure 1.4**).

Meanwhile, soft electronics that are not fabricated with biodegradable materials often induce acute or chronic inflammatory responses after implantation *in vivo*. While anti-inflammatory drugs are generally used to reduce that problems,[40] the drugs also induce serious side effects on the target tissues and have reload issues.[41] When the implantable device, however, is coated with cells originated from target tissue, the inflammation effect can be minimized due to the formation of high-quality biointerface.[42,43] Also, continuous proliferation and differentiation of the transplanted cells lead to cell therapy for regenerative medicine.[44,45] Therefore, the research for the integration methods of preparing cell-electronics complex and for those interfaces have been consequently studied for enhancing biointerfaces and exploiting intrinsic cellular properties using various types of cells such as neurons,[46] cardiomyocytes,[47] and light-sensitive HeLa cells (**Figure 1.5**).[48]

In this thesis, the guidance of cellular alignment in culturing cells

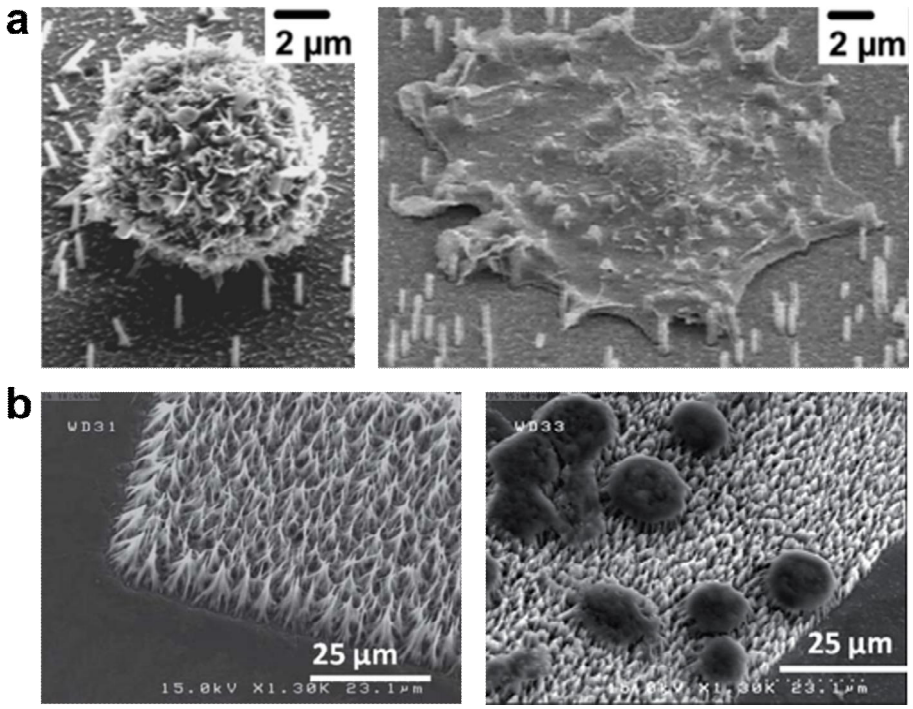

Figure 1.4 Vertical nanowire sensors

(a) SEM images of spherical cell and spreading cell cultured on silicon nanowire array. (b) SEM images of vertical carbon nanowire array and cells cultured on the substrate.

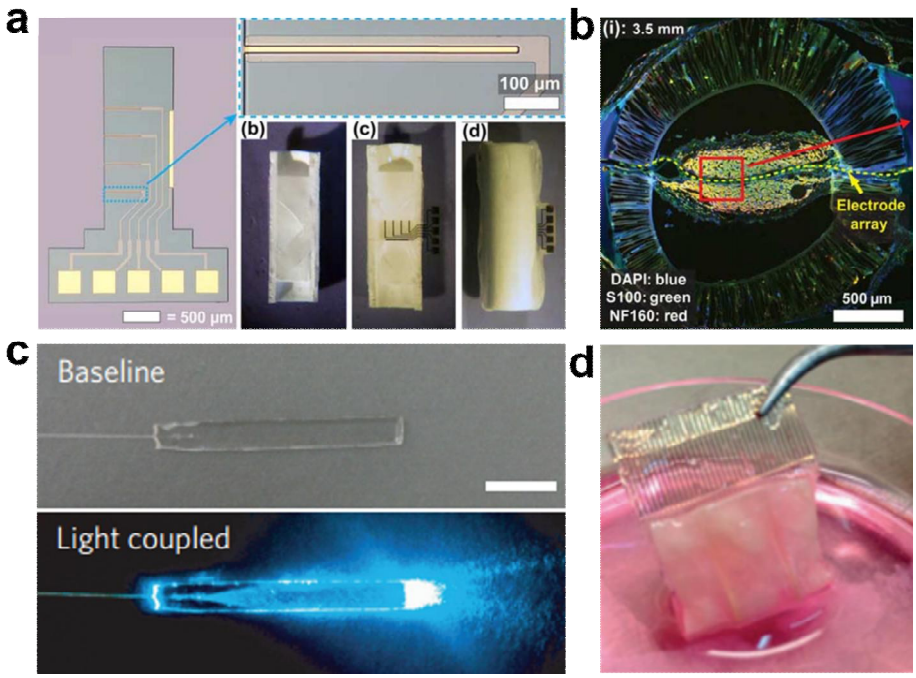

Figure 1.5 Cell-electronics interfaces for biomedical applications

(a) Photographic images of regenerative scaffold electrodes. (b) Neuronal cells on the regenerative scaffold electrodes after implantation during 8 weeks. (c) Light-guiding hydrogel incorporating light-sensitive HeLa cells. (d) Soft electronic device coated with cardiomyocytes for cardiac applications.

for mimicking the native tissue and their activities including adhesion, proliferation, and differentiation that are cultured on multifunctional cell-culture-platform will be described. In chapter 2, micro-patterned graphene nanoribbon is transfer-printed onto the stretchable electronics for guiding anisotropic alignment of C2C12 myoblasts. In chapter 3, the graphene electrodes are formed into buckled structure to bring stretchability of the device and to promote cellular alignment. In chapter 4, the electronic device is coated with non-conductive and patterned graphene oxide nanoparticles to show that the cells can be aligned into a variety of design while the performance of electrodes is maintained.

1.3 Soft electronics for three-dimensional cell culturing

Advanced cell-culture-platform fabricated with three-dimensional (3D) structures have been widely developed for the research in cell therapy or cytotoxicity test in bioengineering.[49] The substrates are usually made of FDA-approved poly(α-hydroxy esters) group including polylactic acid (PLA) and polycaprolactone (PCL) with various types of structures including nanofiber,[50] hydrogel,[51] and porous polymer resin.[52] Recently, a decrease in the cost of high-performance 3D printer and its spread among tissue engineering research have led to the fabrication of substrate with precise structure using a variety of biocompatible materials (**Figure 1.6**).[53,54] Additionally, many studies in finding biocompatible and 3D printable materials,[54,55] effective design for enhancing cellular activities,[56] and efficient method for surface modification using bioactive molecules[57] have been perused to provide multifunctionalities in 3D substrate for culturing cells.

Also, the studies for altering the electrical property of substrate are widely conducted by incorporating functional nanomaterials such as Au nanowire,[58] polyaniline,[59] or carbon nanotube (**Figure 1.7**).[60] However, some limitations such as complexity in fabrication process and heterogeneous

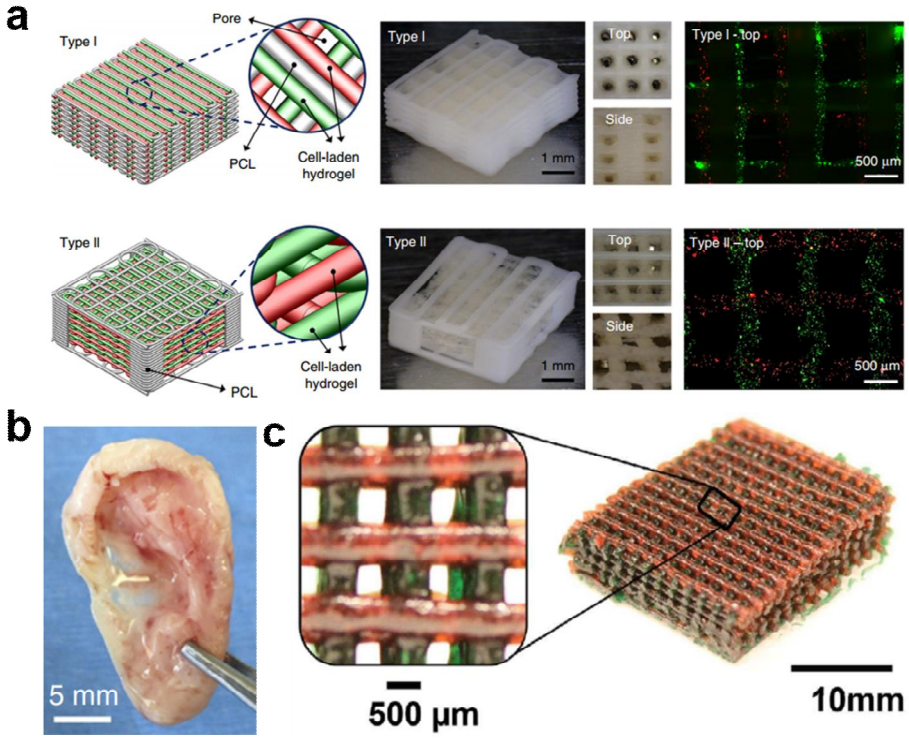

Figure 1.6 Bioengineered scaffolds prepared by high-performance 3D printer

(a) Scheme, photographic, and microscopic images of 3D patterning using biocompatible materials such as cell-laden hydrogel mixed with PCL. (b) Artificial human ear composed of cells and polymer fabricated by 3D printer. (c) Mesh composed of cell laden tough and biocompatible hydrogel prepared by 3D printer.

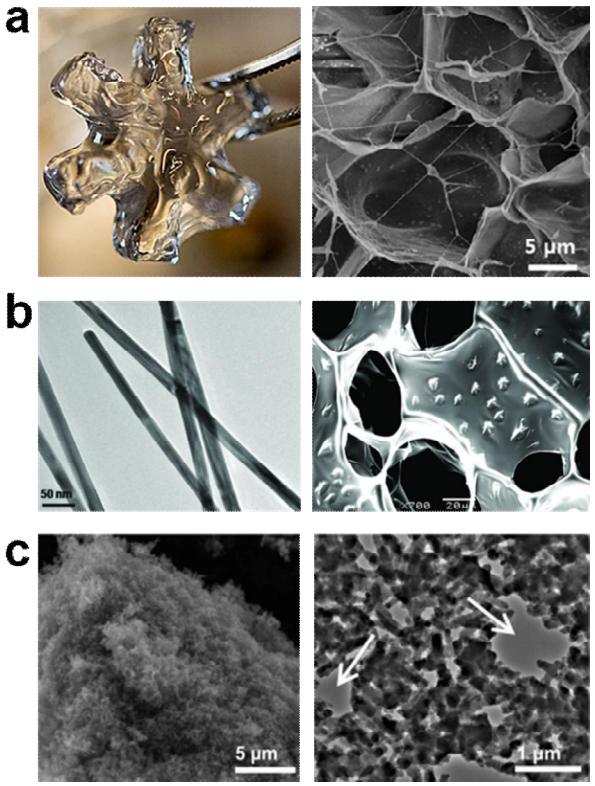

Figure 1.7 Advanced 3D substrate for culturing cells mixed with functional nanomaterials

(a) Photographic and SEM images of implantable alginate hydrogel incorporating single-walled carbon nanotube for sensing the biomarkers *in vivo* applications. (b) TEM (left) and SEM (right) image of gold nanowires (Au NWs) and alginate hydrogel mixed with Au NWs, respectively. (c) SEM (left) and TEM (right) images of polyaniline hydrogel crosslinked by phytic acid.

properties of materials have hindered the prepararation of multifunctional and high-performance cell-culture-platform. Meanwhile, the transfer printing of soft electronics onto the biocompatible substrate designed by a 3D printer can bring the versatile functions during 3D cell culturing. These types of soft electronics can be also rolled[61] or folded[62] to form 3D structure to serve as an electronics-based platform which can achieve *in vitro* analysis devices. Also, these electronics can be integrated onto curved surface of biomedical instruments[19] or injected directly into organs[63] for monitoring the electrophysiological signals of native tissue in 3D environment (**Figure 1.8**).

The soft electronics which can be integrated with 3D substrate can encompass many different types of sensors which can perform real-time and *in situ* monitoring of cellular physiologies and the culturing environment. Consequently, the research in comparing the cellular property of the culturing cells that are either cultured in 2D or 3D substrate can be conducted, and the analysis of cellular behavior for the cells cultured in 3D substrate which previously could not be done with phase contrast microscopy can be realized. In chapter 4, multifunctional electronic-cell-culture-platform that are advanced through the integration of soft electronics and stackable 3D-printed substrate will be discussed.

1.4 References

1. Chen, L., Deng, y., Luo, W., Wang, Z. & Zeng, S. Detection of bursts in neuronal spike trains by the mean inter-spike interval method. *Prog. Nat. Sci.* **19**, 229-235 (2009).
2. Heuschkel, M, O., Fejtl, M., Raggenbass, M., Bertrand, D. & Renaud, P. A three-dimensional multi-electrode array for multi-site stimulation and recording in acute brain slices. *J. Neurosci. Methods* **114**, 135-148 (2002).
3. Qu, Y. & Vargas, H, M., Proarrhythmia risk assessment in human induced pluripotent stem cell-derived cardiomyocytes using the maestro MEA platform. *Toxicol. Sci.* **147**, 286-295 (2015).
4. Pradhapan, P., Kuusela, J., Viik, J., Aalto-Setälä, K. & Hyttinen, J. Cardiomyocyte MEA data analysis (CardioMDA)--a novel field potential data analysis software for pluripotent stem cell derived cardiomyocytes. *PLoS One* **8**, e73637 (2013).
5. Park, H, E., Kim, D., Koh, H, S., Cho, S., Sung, J,-S. & Kim, J, Y. Real-time monitoring of neural differentiation of human mesenchymal stem cells by electric cell-substrate impedance sensing. *J Biomed. Biotechnol.* 485173 (2011).
6. Bagnaninchi, P, O. & Drummond, N. Real-time label-free monitoring of adipose-derived stem cell differentiation with electric cell-substrate

impedance sensing. *Proc. Natl. Acad. Sci. U. S. A.* **108**, 6462-6467 (2011).

7. Zheng, G., Patolsky, F., Cui, Y., Wang, W, U. & Lieber, C, M. Multiplexed electrical detection of cancer markers with nanowire sensor arrays. *Nat. Biotechnol.* **23**, 1298-1301 (2005).

8. Berdondini, L., Imfeld, K., Maccione, A., Tedesco, M., Neukom, S., Koudelka-Hep, M. & Martinoiaac, S. Active pixel sensor array for high spatio-temporal resolution electrophysiological recordings from single cell to large scale neuronal networks. *Lab Chip* **9**, 2644-2651 (2009).

9. Imfeld, K., Neukom, S., Maccione, A., Bornat, Y., Martinoia, S., Farine, P, A., Koudelka-Hep, M. & Berdondini, L. Large-scale, high-resolution data acquisition system for extracellular recording of electrophysiological activity. *IEEE Trans. Biomed. Eng.* **55**, 2064-2073 (2008).

10. Maynard, E, M., Nordhausen, C, T. & Normann, R, A. The Utah intracortical electrode array: a recording structure for potential brain-computer interfaces. *Electroencephalogr. Clin. Neurophysiol.* **102**, 228-239 (1997).

11. Hoogerwerf, A, C. & Wise, K, D. A three-dimensional microelectrode array for chronic neural recording. *IEEE Trans. Biomed. Eng.* **41**, 1136-1146 (1994).

12. Vichare, S., Sen, S. & Inamdar, M, M. Cellular mechanoadaptation to

substrate mechanical properties: contributions of substrate stiffness and thickness to cell stiffness measurements using AFM. *Soft Matter* **10**, 1174-1181 (2014).

13. Engler, A, J., Sen, S., Sweeney, H, L. & Discher, D, E. Matrix elasticity directs stem cell lineage specification. *Cell* **126**, 677-689 (2006).

14. Asghari, F., Samiei, M., Adibkia, K., Akbarzadeh, A. & Davaran, S. Biodegradable and biocompatible polymers for tissue engineering application: a review. *Artif. Cells Nanomed. Biotechnol.* **45**, 185-192 (2017).

15. Kaltenbrunner, M., Sekitani, T., Reeder, J., Yokota, T., Kuribara, K., Tokuhara, T., Drack, M., Schwödiauer, R., Graz, I., Bauer-Gogonea, S., Bauer, S. & Someya, T. An ultra-lightweight design for imperceptible plastic electronics. *Nature* **499**, 458-463 (2013).

16. Khodagholy, D., Rivnay, J., Sessolo, M., Gurfinkel, M., Leleux, P., Jimison, L, H., Stavrinidou, E., Herve, T., Sanaur, S., Owens, R, M. & Malliaras, G, G. High transconductance organic electrochemical transistors. *Nat. Commun.* **4**, 2133 (2013).

17. Khodagholy, D,, Doublet, T., Quilichini, P., Gurfinkel, M., Leleux, P., Ghestem, A., Ismailova, E., Hervé, T., Sanaur, S., Bernard, C. & Malliaras, G, G. In vivo recordings of brain activity using organic transistors. *Nat.*

Commun. **4**, 1575 (2013).

18. Kim, D,-H., Lu, N., Ma, R., Kim, Y,-S., Kim, R,-H., Wang, S., Wu, J., Won, S, M., Tao, H., Islam, A., Yu, K, J., Kim, T,-i., Chowdhury, R., Ying, M., Xu, L., Li, M., Chung, H,-J., Keum, H., McCormick, M., Liu, P., Zhang, Y,-W., Omenetto, F, G., Huang, Y., Coleman, T. & Rogers, J, A. Epidermal electronics. *Science* **333**, 838-843 (2011).

19. Kim, D, H., Lu, N., Ghaffari, R., Kim, Y, S., Lee, S, P., Xu, L., Wu, J., Kim, R, H., Song, J., Liu, Z., Viventi, J., de, Graff, B., Elolampi, B., Mansour, M., Slepian, M, J., Hwang, S., Moss, J, D., Won, S, M., Huang, Y., Litt, B. & Rogers J, A. Materials for multifunctional balloon catheters with capabilities in cardiac electrophysiological mapping and ablation therapy. *Nat. Mater.* **10**, 316-323 (2011).

20. Kim, D, H., Ghaffari, R., Lu, N., Wang, S., Lee, S, P., Keum, H., D'Angelo, R., Klinker, L., Su, Y., Lu, C., Kim, Y, S., Ameen, A., Li, Y., Zhang, Y., de, Graff, B., Hsu, Y, Y., Liu, Z., Ruskin, J., Xu, L., Lu, C., Omenetto, F, G., Huang, Y., Mansour, M., Slepian, M, J. & Rogers, J, A. Electronic sensor and actuator webs for large-area complex geometry cardiac mapping and therapy. *Proc. Natl. Acad. Sci. U. S. A.* **109**, 19910-19915 (2012).

21. Weisse, J, M., Lee, C, H., Kim, D, R. & Zheng, X. Fabrication of flexible

and vertical silicon nanowire electronics. *Nano Lett.* **12**, 3339-3343 (2012).

22. Kang, H., Jung, S., Jeong, S., Kim, G. & Lee K. Polymer-metal hybrid transparent electrodes for flexible electronics. *Nat. Commun.* **6**, 6503 (2015).

23. Choi, M, K., Park, I., Kim, D, C., Joh, E., Park, O, K., Kim, J., Kim, M., Choi, C., Yang, J., Cho, K, W., Hwang, J,-H., Nam, J,-M., Hyeon, T., Kim, J, H. & Kim, D,-H. Thermally controlled, patterned graphene transfer printing for transparent and wearable electronic/optoelectronic system. *Adv. Funct. Mater.* **25**, 7109-7118 (2015).

24. Lee, H., Choi, T, K., Lee, Y, B., Cho, H, R., Ghaffari, R., Wang, L., Choi, H, J., Chung, T, D., Lu, N., Hyeon, T., Choi, S, H. & Kim, D, H. A graphene-based electrochemical device with thermoresponsive microneedles for diabetes monitoring and therapy. *Nat. Nanotechnol.* **11**, 566-572 (2016).

25. Son, D., Koo, J, H., Song, J, K., Kim, J., Lee, M., Shim, H, J., Park, M., Lee, M., Kim, J, H. & Kim D, H. Stretchable carbon nanotube charge-trap floating-gate memory and logic devices for wearable electronics. *ACS Nano* **9**, 5585-5593 (2015).

26. Kim, S, H., Turnbull, J. & Guimond, S. Extracellular matrix and cell signalling: the dynamic cooperation of integrin, proteoglycan and growth

factor receptor. *J. Endocrinol.* **209**, 139-151 (2011).

27. Chandler, E, M., Seo, B, R., Califano, J, P., Andresen, Eguiluz, R, C., Lee, J, S., Yoon, C, J., Tims, D, T., Wang, J, X., Cheng, L., Mohanan, S., Buckley, M, R., Cohen, I., Nikitin, A, Y., Williams, R, M., Gourdon, D., Reinhart-King, C, A. & Fischbach, C. Implanted adipose progenitor cells as physicochemical regulators of breast cancer. *Proc. Natl. Acad. Sci. U. S. A.* **109**, 9786-9791 (2012).

28. Guvendiren, M. & Burdick, J, A. The control of stem cell morphology and differentiation by hydrogel surface wrinkles. *Biomaterials* **31**, 6511-6518 (2010).

29. Bhuyan, M, K., Rodriguez-Devora, J, I., Fraser, K. & Tseng, T, L. Silicon substrate as a novel cell culture device for myoblast cells. *J. Biomed. Sci.* **21**, 47 (2014).

30. Rivnay, J., Leleux, P., Hama, A., Ramuz, M., Huerta, M., Malliaras, G, G. & Owens, R, M. Using white noise to gate organic transistors for dynamic monitoring of cultured cell layers. Sci. Rep. 5, 11613 (2015).

31. Boero, C., Carrara, S., Del, Vecchio, G., Calzà, L. & De, Micheli, G. Highly sensitive carbon nanotube-based sensing for lactate and glucose monitoring in cell culture. *IEEE Trans. Nanobioscience* **10**, 59-67 (2011).

32. Wang, Y., Tang, L., Li, Z., Lin, Y. & Li, J. In situ simultaneous

monitoring of ATP and GTP using a graphene oxide nanosheet-based sensing platform in living cells. *Nat. Protoc.* **9**, 1944-1955 (2014).

33. Fabbro, A., Prato, M. & Ballerini, L. Carbon nanotubes in neuroregeneration and repair. *Adv. Drug Deliv. Rev.* **65**, 2034-2044 (2013).

34. Kim, D, H., Lipke, E, A., Kim, P., Cheong, R., Thompson, S., Delannoy, M., Suh, K, Y., Tung, L. & Levchenko, A. Nanoscale cues regulate the structure and function of macroscopic cardiac tissue constructs. *Proc. Natl. Acad. Sci. U. S. A.* **107**, 565-570 (2010).

35. Lehnert, D., Wehrle-Haller, B., David, C., Weiland, U., Ballestrem, C., Imhof, B, A. & Bastmeyer, M. Cell behaviour on micropatterned substrata: limits of extracellular matrix geometry for spreading and adhesion. *J. Cell Sci.* **117**, 41-52 (2004).

36. Kim, S, J., Jun, I., Kim, D, W., Lee, Y, B., Lee, Y, J., Lee, J, H., Park, K, D., Park, H. & Shin, H. Rapid transfer of endothelial cell sheet using a thermosensitive hydrogel and its effect on therapeutic angiogenesis. *Biomacromolecules* **14**, 4309-4319 (2013).

37. Kim, W., Ng, J, K., Kunitake, M, E., Conklin, B, R. & Yang, P. Interfacing silicon nanowires with mammalian cells. *J. Am. Chem. Soc.* **129**, 7228-7229 (2007).

38. Xie, X., Xu, A, M., Angle, M, R., Tayebi, N., Verma, P. & Melosh, N, A.

Mechanical model of vertical nanowire cell penetration. *Nano Lett.* **13**, 6002-6008 (2013).

39. Abdolahad, M., Taghinejad, M., Taghinejad, H., Janmaleki, M. & Mohajerzadeh, S. A vertically aligned carbon nanotube-based impedance sensing biosensor for rapid and high sensitive detection of cancer cells. *Lab Chip* **12**, 1183-1190 (2012).

40. Hickey, T., Kreutzer, D., Burgess, D, J. & Moussy, F. Dexamethasone/PLGA microspheres for continuous delivery of an anti-inflammatory drug for implantable medical devices. *Biomaterials* **23**, 1649-1656 (2002).

41. Minev, I, R., Musienko, P., Hirsch, A., Barraud, Q., Wenger, N., Moraud, E, M., Gandar, J., Capogrosso, M., Milekovic, T., Asboth, L., Torres, R, F., Vachicouras, N., Liu, Q., Pavlova, N., Duis, S., Larmagnac, A., Vörös, J., Micera, S., Suo, Z., Courtine, G. & Lacour, S, P. Biomaterials. Electronic dura mater for long-term multimodal neural interfaces. Science 347, 159-163 (2015).

42. Zhou, W., Han, C., Song, Y., Yan, X., Li, D., Chai, Z., Feng, Z., Dong, Y., Li, L., Xie, X., Chen, F. & Zhao, Y. The performance of bone marrow mesenchymal stem cell--implant complexes prepared by cell sheet engineering techniques. *Biomaterials* **31**, 3212-3221 (2010).

43. Yu, M., Zhou, W., Song, Y., Yu, F., Li, D., Na, S., Zou, G., Zhai, M. & Xie, C. Development of mesenchymal stem cell-implant complexes by cultured cells sheet enhances osseointegration in type 2 diabetic rat model. *Bone* **49**, 387-394 (2011).

44. Kito, T., Shibata, R., Ishii, M., Suzuki, H., Himeno, T., Kataoka, Y., Yamamura, Y., Yamamoto, T., Nishio, N., Ito, S., Numaguchi, Y., Tanigawa, T., Yamashita, J, K., Ouchi, N., Honda, H., Isobe, K. & Murohara, T. iPS cell sheets created by a novel magnetite tissue engineering method for reparative angiogenesis. *Sci. Rep.* **3**, 1418 (2013).

45. Jun, I., Kim, S, J., Lee, J,-H., Lee, Y, J., Shin, Y, M., Choi, E., Park, K, M., Park, J., Park, K, D. & Shin, H., Transfer printing of cell layers with an anisotropic extracellular matrix assembly using cell-interactive and thermosensitive hydrogels. *Adv. Funct. Mater.* **22**, 4060-4069 (2012).

46. Clements, I, P., Mukhatyar, V, J., Srinivasan, A., Bentley, J, T., Andreasen, D, S. & Bellamkonda, R, V. Regenerative scaffold electrodes for peripheral nerve interfacing. *IEEE Trans. Neural. Syst. Rehabil. Eng.* **21**, 554-566 (2013).

47. Feiner, R., Engel, L., Fleischer, S., Malki, M., Gal, I., Shapira, A., Shacham-Diamand, Y. & Dvir, T. Engineered hybrid cardiac patches with multifunctional electronics for online monitoring and regulation of tissue

function. *Nat. Mater.* **15**, 679-685 (2016).

48. Choi, M., Choi, J, W., Kim, S., Nizamoglu, S., Hahn, S, K. & Yun, S, H. Light-guiding hydrogels for cell-based sensing and optogenetic synthesis in vivo. *Nat. Photonics.* **7**, 987-994 (2013).

49. Chen, C, Y., Ke, C, J., Yen, K, C., Hsieh, H, C., Sun, J, S. & Lin, F, H. 3D porous calcium-alginate scaffolds cell culture system improved human osteoblast cell clusters for cell therapy. *Theranostics* **5**, 643-655 (2015).

50. Stachewicz, U., Qiao, T., Rawlinson, S, C., Almeida, F, V., Li, W, Q., Cattell, M. & Barber, A, H. 3D imaging of cell interactions with electrospun PLGA nanofiber membranes for bone regeneration. *Acta Biomater.* **27**, 88-100 (2015).

51. Rahman, C, V., Kuhn, G., White, L, J., Kirby, G, T., Varghese, O, P., McLaren, J, S., Cox, H, C., Rose, F, R., Müller, R., Hilborn, J. & Shakesheff, K, M. PLGA/PEG-hydrogel composite scaffolds with controllable mechanical properties. *J. Biomed. Mater. Res. B Appl. Biomater.* **101**, 648-655 (2013).

52. Izquierdo, R., Garcia-Giralt, N., Rodriguez, M, T., Cáceres, E., García, S, J., Gómez, Ribelles, J, L., Monleón, M., Monllau, J, C. & Suay, J. Biodegradable PCL scaffolds with an interconnected spherical pore network for tissue engineering. *J. Biomed. Mater. Res. A* **85**, 25-35 (2008).

53. Kang, H, W., Lee, S, J., Ko, I, K., Kengla, C., Yoo, J, J. & Atala, A. A 3D bioprinting system to produce human-scale tissue constructs with structural integrity. *Nat. Biotechnol.* **34**, 312-319 (2016).

54. Hong, S., Sycks, D., Chan, H, F., Lin, S., Lopez, G, P., Guilak, F., Leong, K, W. & Zhao, X. 3D printing of highly stretchable and tough hydrogels into complex, cellularized structures. *Adv. Mater.* **27**, 4034 (2015).

55. Do, A, V., Khorsand, B., Geary, S, M. & Salem, A, K. 3D Printing of Scaffolds for Tissue Regeneration Applications. *Adv. Healthc. Mater.* **4**, 1742-1762 (2015).

56. Gómez, S., Vlad, M, D., López, J. & Fernández, E. Design and properties of 3D scaffolds for bone tissue engineering. *Acta Biomater.* **42**, 341-350 (2016).

57. Lee, S, J., Lee, D., Yoon, T, R., Kim, H, K., Jo, H, H., Park, J, S., Lee, J, H., Kim, W, D., Kwon, I, K. & Park, S, A. Surface modification of 3D-printed porous scaffolds via mussel-inspired polydopamine and effective immobilization of rhBMP-2 to promote osteogenic differentiation for bone tissue engineering. *Acta Biomater.* **40**, 182-191 (2016).

58. Dvir, T., Timko, B, P., Brigham, M, D., Naik, S, R., Karajanagi, S, S., Levy, O., Jin, H., Parker, K, K., Langer, R. & Kohane, D, S. Nanowired three-dimensional cardiac patches. *Nat. Nanotechnol.* **6**, 720-725 (2011).

59. Pan, L., Yu, G., Zhai, D., Lee, H, R., Zhao, W., Liu, N., Wang, H., Tee, B, C., Shi, Y., Cui, Y. & Bao, Z. Hierarchical nanostructured conducting polymer hydrogel with high electrochemical activity. *Proc. Natl. Acad. Sci. U. S. A.* **109**, 9287-9292 (2012).

60. Iverson, N, M., Barone, P, W., Shandell, M., Trudel, L, J., Sen, S., Sen, F., Ivanov, V., Atolia, E., Farias, E., McNicholas, T, P., Reuel, N., Parry, N, M., Wogan, G, N. & Strano, M, S. In vivo biosensing via tissue-localizable near-infrared-fluorescent single-walled carbon nanotubes. *Nat. Nanotechnol.* **8**, 873-880 (2013).

61. Tian, B., Liu, J., Dvir, T., Jin, L., Tsui, J, H., Qing, Q., Suo, Z., Langer, R., Kohane, D, S. & Lieber, C, M. Macroporous nanowire nanoelectronic scaffolds for synthetic tissues. *Nat. Mater.* **11**, 986-994 (2012).

62. Dai, X., Zhou, W., Gao, T., Liu, J. & Lieber, C, M. Three-dimensional mapping and regulation of action potential propagation in nanoelectronics-innervated tissues. *Nat. Nanotechnol.* **11**, 776-782 (2016).

63. Liu, J., Fu, T, M., Cheng, Z., Hong, G., Zhou, T., Jin, L., Duvvuri, M., Jiang, Z., Kruskal, P., Xie, C., Suo, Z., Fang, Y. & Lieber, C, M. Syringe-injectable electronics. *Nat. Nanotechnol.* **10**, 629-636 (2015).

Chapter 2. Soft and Instrumented Cell-Culture-Platform for Monitoring and Transfer Printing of Cell Sheets

2.1 Introduction

Tissue engineering scaffolds, including two dimensional cell-culture-substrates, serve as synthetic extracellular matrices (ECMs) to support cells in culture systems and to assist the regeneration of damaged tissues.[1] Although significant progress in scaffold technology has been made,[2,3] including improvements in materials and structural designs, most scaffolds remain passive, *i.e.* they only provide structural support without any *in situ* and real-time monitoring capability. Passive scaffolds thus need *ex situ* biological assays, which demands the delicate assay techniques and the sacrifice of cells. Therefore, the development of active scaffolds embedded with sensors[4] that continuously monitor cellular physiology *in vitro* and the therapeutic application of cells prepared from such scaffolds *in vivo* represent a new frontier of tissue engineering. Wafer-based electronics have demonstrated such capabilities;[5] however, these rigid, planar wafers are

mechanically incompatible with soft, flexible tissues. To this front, flexible[6,7] and stretchable[8-12] electronics offer a viable solution.

Meanwhile, biodegradability and cytotoxicity of onboard electronic devices may hinder the potential *in vivo* implantation of such electronic scaffolds. Scaffold-free cell sheet application is an attractive approach to overcome these limitations. Cell sheet therapy provides robust benefits in localized treatments by eliciting high paracrine effects and has been successfully used in the cornea,[13] periodontium,[14] and heart.[15] A temperature-sensitive polymer, poly(N-isopropylacrylamide) (PIPAAm), has been widely used to prepare and transfer cell sheets[13-15] to *in vivo* models. However, the electron irradiation process required to precisely control the ultrathin thickness (< 30 nm) of the PIPAAm substrate[16] is highly delicate. Moreover, integrating PIPAAm with high-performance electronics is difficult because of its instability during the fabrication process of electronics (*e.g.* heat, solvent, acid, etching *etc.*). Therefore, a simpler yet more electrically and mechanically engineered platform for scaffold-free cell sheet treatment is needed.

Here, we introduce a soft instrumented cell-culture-platform comprised of ultrathin stretchable gold nanomembrane sensors and patterned graphene-nanoribbon cell aligners on a biocompatible low-modulus (~36.2

kPa) polydimethylsiloxane (PDMS) substrate (**Figure 2.1**). The low-modulus PDMS offers optimal softness that is compatible with native skeletal muscle tissues.[17] Stretchable physiology (impedance and temperature) sensors based on serpentine,[9,18] buckled[19-21] gold nanomembranes (**Figure 2.1a** inset) are fabricated using photolithography (**Figure 2.1c**). Anisotropically micro-patterned (~5 μm lines and spaces) graphene nanoribbons promote cell adhesion,[22,23] alignment,[24] and differentiation.[25] Ultrathin thicknesses of gold nanomembranes and graphene nanoribbons (~150 nm and ~5 nm, respectively) minimize the increase of the system modulus (44.9 kPa, integrated system), which is designed to be matched with target tissues (45.9 kPa, muscle). Intrinsically soft graphenes[12,26] also contribute low system modulus. This soft instrumented cell-culture-platform has four major functions (**Figure 2.2**): i) aligning cells on patterned graphene nanoribbons to promote muscle cell differentiation, ii) real-time physiological monitoring of cells during proliferation and differentiation by integrated sensors, iii) serving as an *in vitro* muscle-on-a-chip[27-29] platform to test the effects of novel nanomaterials or drugs, and iv) *in vivo* transfer printing of differentiated cell layers for scaffold-free cell sheet treatments.

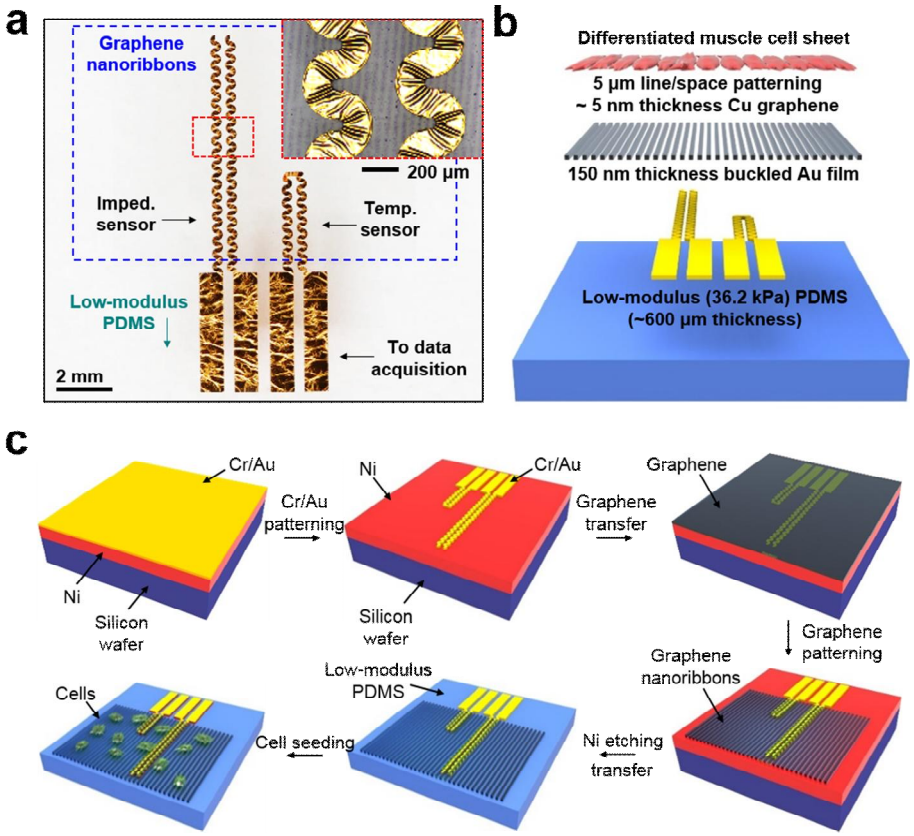

Figure 2.1 Architecture and fabrication process of the instrumented cell-culture-platform

(a) The cell-culture-platform is made of patterned graphene nanoribbons (top layer) and Au nanomembrane impedance/temperature sensors (bottom layer) on a low-modulus PDMS sheet. The top right inset shows the magnified view of serpentine-shaped buckled Au electrodes. (b) Expanded view of each element of the cell-culture-platform. (c) A schematic overview of the fabrication process.

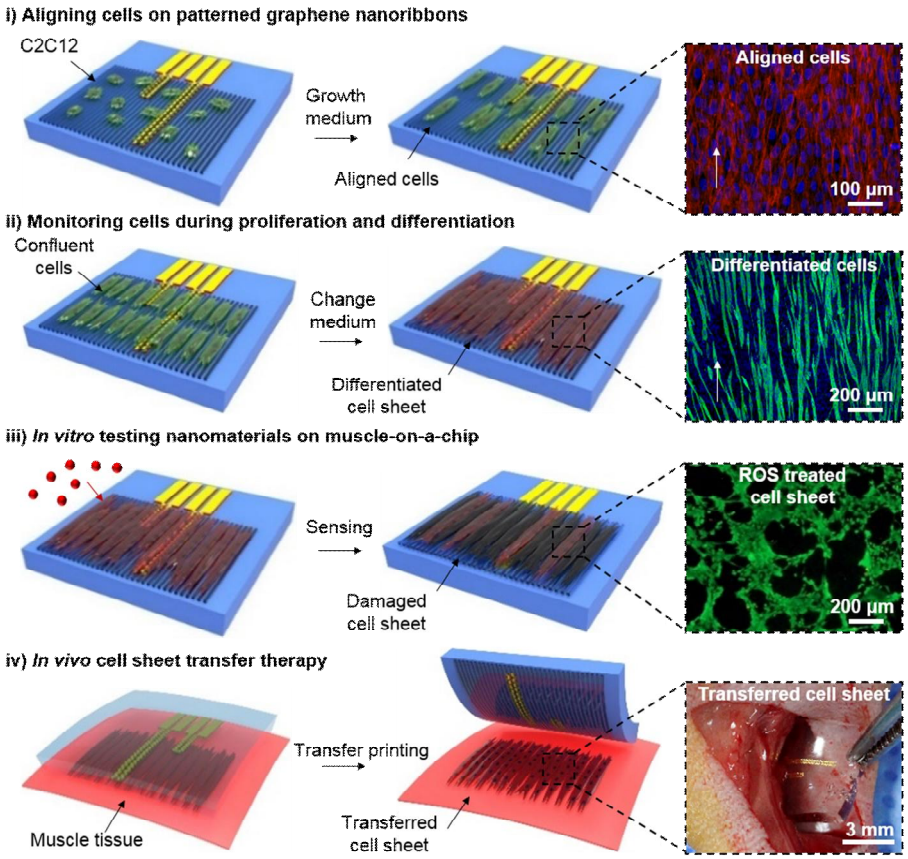

Figure 2.2 Summary of the four key applications of the soft cell-culture-platform: i) aligning C2C12 myoblasts, ii) *in situ* monitoring of proliferation and differentiation, iii) evaluating the effects of novel nanomaterials and drugs *in vitro*, and iv) transfer printing cultured cell sheets onto target sites of animal models *in vivo*.

2.2 Results and Discussion

2.1.1 Cellular activities on the patterned graphene nanoribbons

The graphene nanoribbons are transferred[26] on a low-modulus PDMS substrate. The sheet resistance is approximately 1 kΩ/sq. (measured using a 4-point probe system; CMT-100MP, Advanced Instrument Technology). The atomic force microscopy (AFM) topological images and water contact angle of graphene nanoribbons (approximately 112.38°) are shown in **Figure 2.3**. The π - π interaction and hydrophobicity of the graphene[30] result in six-fold stronger protein adhesion than PDMS alone, as shown in the AFM analysis, in which a fibronectin-coated tip is used (**Figure 2.4a**). The strongly adhesive properties of ECM proteins on graphene facilitate the cell adhesion.[31] Three days after culture, C2C12 myoblasts stained with a LIVE/DEAD Viability Kit (Life Technologies) are preferably adhered and proliferated on the graphene nanoribbons without additional treatments (**Figure 2.4b**).

The widths and spacing of graphene nanoribbons are important for cell alignment. We cultured C2C12 myoblasts for 3 days on graphene-nanoribbon substrates with different feature sizes (**Figure 2.5a**). Cells are considered to be aligned along graphene-nanoribbon patterns when the cell

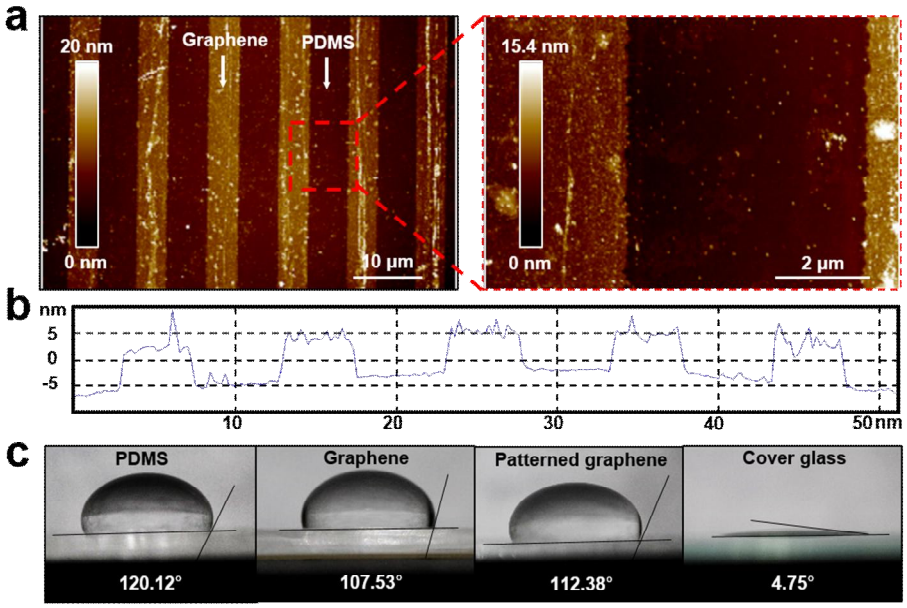

Figure 2.3 Characterizations of patterned graphene nanoribbons

(a) Atomic force microscope (AFM) topological image of the patterned graphene on PDMS. (b) AFM topological graph of patterned graphene on PDMS. (c) Water contact angles of various substrates: PDMS, graphene, patterned graphene (widths of line and spacing; 5 μm), and cover glass.

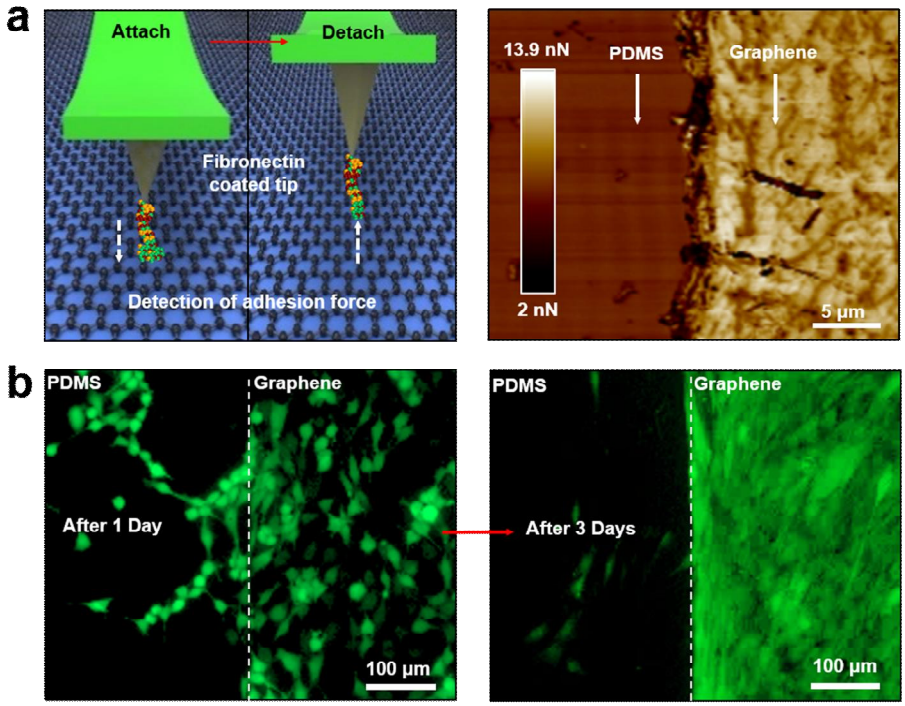

Figure 2.4 Surface properties of graphene nanoribbon for culturing cells

(a) Measurement of the adhesion force between fibronectin molecules and graphene. The left frame shows a schematic illustration of AFM adhesion force measurements using the fibronectin-coated AFM tip, and the right frame presents the force map. (b) Images showing the biocompatible, cell-friendly surface of patterned graphene nanoribbons.

orientation is within the range of -10° to +10° with respect to the ribbon orientation. Graphene patterns with nanoribbon widths and spacing of < ~5 μm show higher alignment ratios than those of 10 ~50 μm, while those of 100 μm show almost no alignment (**Figure 2.5b**). C2C12 myoblast differentiation is enhanced by patterned graphene nanoribbons as indicated by myosin heavy chain (MHC) immunostaining (**Figure 2.6a-c**).[32] C2C12 myoblasts exhibit larger myotube area and higher alignment ratio when grown on patterned graphene (**Figure 2.6d**) than those grown on bare PDMS or non-patterned graphene.

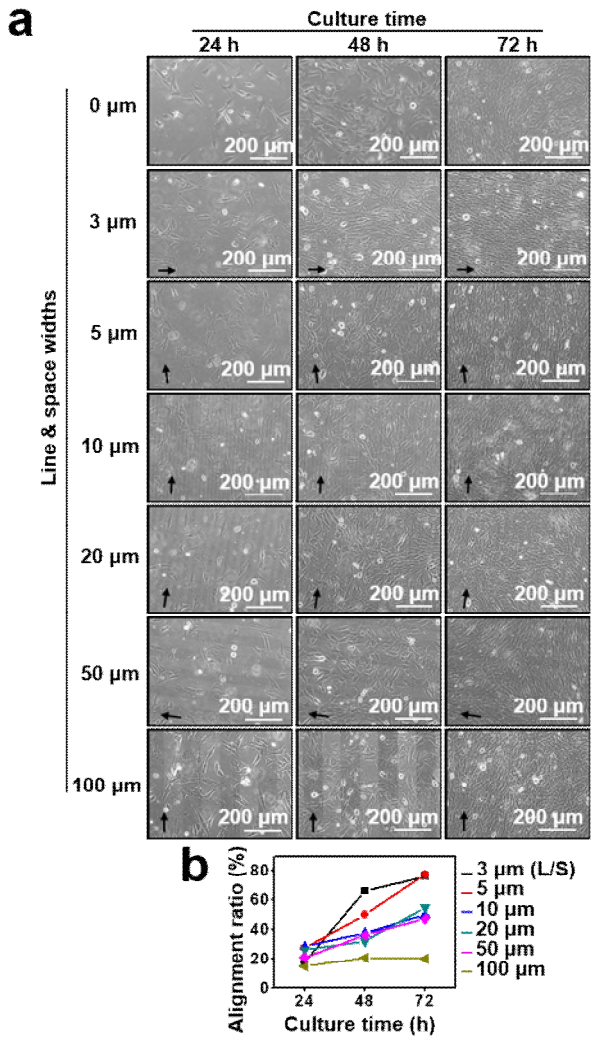

Figure 2.5 Cell alignments in respect to pattern sizes and culture time

(a) C2C12 myoblasts are cultured on the 7 different graphene patterns with different line and space widths (0, 3, 5, 10, 20, 50, and 100 μm) to find the best pattern width for cell alignments. (b) A plot of the cell alignment ratio as a function of culture time for different graphene feature sizes.

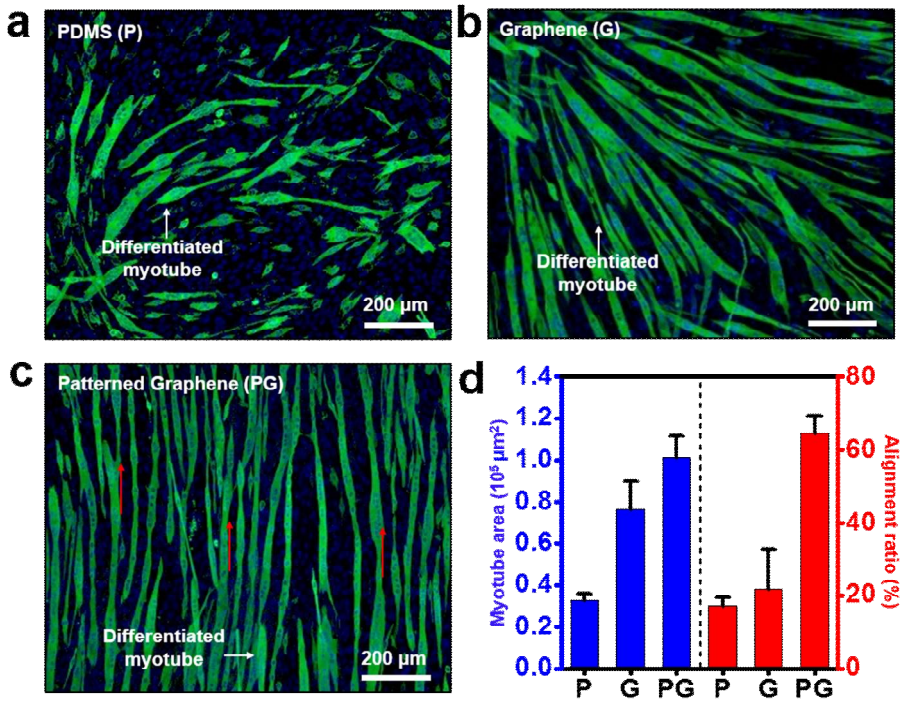

Figure 2.6 Alignment of the C2C12 myoblasts during differentiation on the patterned graphene nanoribbons

(a-c) Myotube formation through myogenic differentiation after 7 days of culture on different substrates, including PDMS (P), graphene (G), and patterned graphene (PG). The red arrows indicate the direction of myotube alignment. (d) A plot of the myotube areas and alignment ratios on different substrates.

2.2.2 Electrophysiological monitoring

Impedance and temperature sensors are also integrated on the low-modulus PDMS substrate, but beneath the patterned graphene nanoribbons, allowing for the *in situ* and real-time monitoring of cellular activities. Cell proliferation and differentiation alter the electrochemical environment around electrodes, and these changes can be detected as impedance or conductance changes.[33] For the impedance sensor, the alternating current (AC) flows through the culture medium between two serpentine electrodes spaced 600 μm apart. For the temperature sensor, we used a resistance temperature detector (RTD)[34] based on a serpentine gold nanomembrane (**Figure 2.7a**). **Figure 2.7b-d** display the calibration curves of the temperature, impedance, and conductance sensors. **Figure 2.8** show changes in impedance during the proliferation and differentiation of C2C12 myoblasts, respectively. The cells on electrodes act as insulating barriers[35] that impede the contact between electrodes and conductive media, thereby increasing the measured impedance while decreasing the measured conductance as cells proliferate (**Figure 2.8a-c**). Formation of myotubes during myogenic differentiation increases conductance and thereby reduces impedance (**Figure 2.8d,e**).[36] **Figure 2.8f** shows time-dependent impedance changes at 17.7 kHz with respect to cell physiology changes. Fibroblasts that

do not form conducting tubular structures[36] are used as a control. Such comparison illustrates that proliferation increases impedance, while differentiation (in growth medium or differentiation medium) decreases impedance. The corresponding conductance measurements exhibit opposite trends (**Figure 2.8g**). Meanwhile, the degree of cellular proliferations for the treatments of growth or differentiation media are similar when cell density is high (**Figure 2.9a**).[37] Therefore, the critical difference in impedance changes after the treatments of the two types of media is due to the effect of myotube formation from differentiations of C2C12 myoblasts (**Figure 2.9b**).

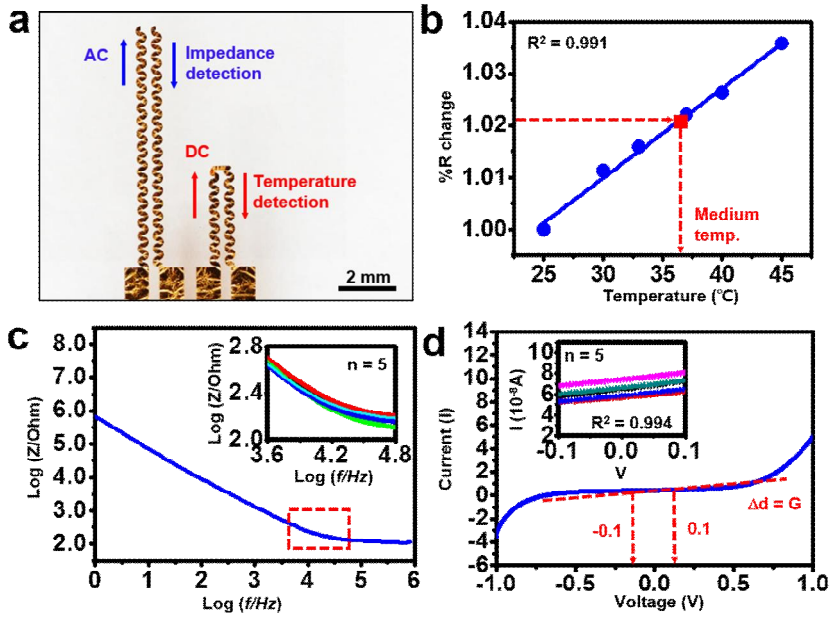

Figure 2.7 Impedance and temperature sensors of the platform

(a) Impedance and temperature sensors integrated on a PDMS substrate. (b) Calibration curve of temperature sensor: normalized resistance (% R change) as a function of temperature. The red arrow indicates the temperature of the growth medium during the culture. (c) Electrochemical characterization of the impedance sensor in the growth medium at 37 °C. Impedance curve measured from 1 Hz to 1 MHz with a bias voltage of 0.01 V. The inset shows the magnified view of the red-dotted region. Repeated measurements show minor deviations. (d) The current-voltage (I-V) curve, whose slope indicates the conductance. The inset shows the magnified view. Repeated measurements confirm the stability of the sensor.

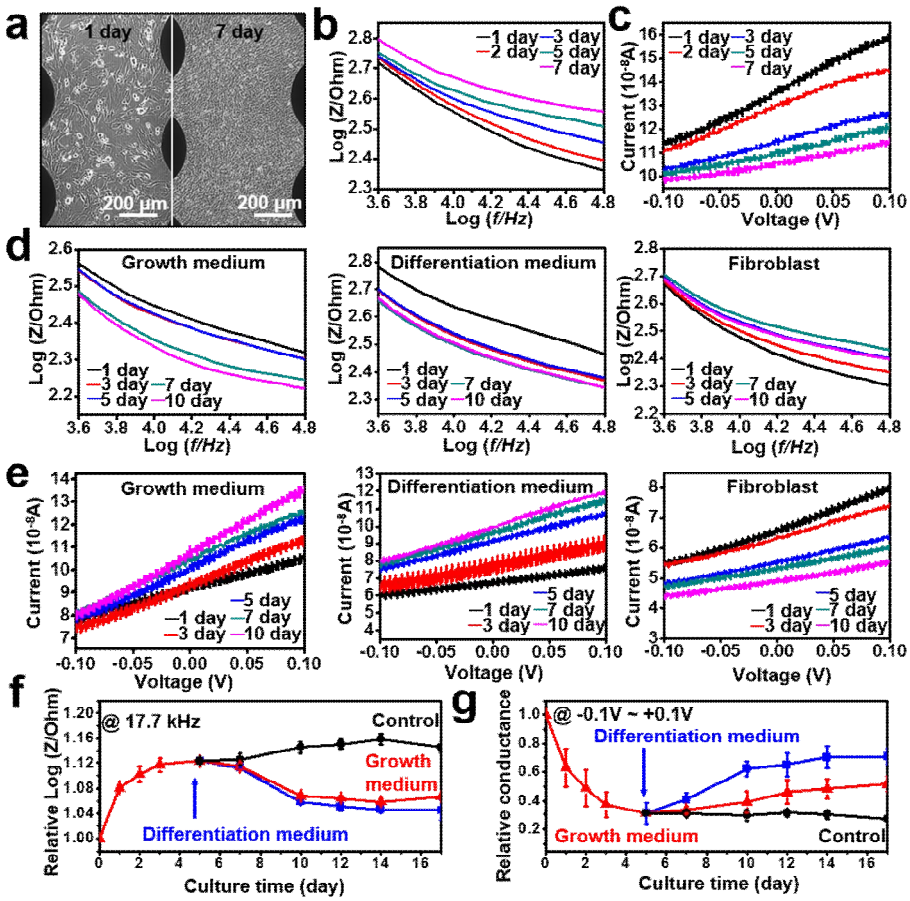

Figure 2.8 Impedance and conductance change during proliferation and differentiation of C2C12 myoblasts

(a) Phase contrast microscope images of C2C12 myoblasts proliferating on the instrumented cell-culture-platform after 1 and 7 days of culture. (b,c) Time-dependent changes of (b) impedance and (c) I-V curve as the C2C12 myoblasts proliferate. (d) Time-dependent impedance change during the differentiation of C2C12 myoblasts cultured in the growth medium (left) and

differentiation medium (middle). The right frame shows the impedance change of fibroblast in the growth medium (control). (e) Time-dependent I-V curve changes during the differentiation of C2C12 myoblasts cultured in the growth medium (left), and differentiation medium (middle). The right frame shows the I-V curve change of fibroblast in growth medium (control). (f) The impedance value measured at 17.7 kHz as the culture proceeded. (g) Conductance values calculated from I-V curves with a range from -0.1 to +0.1 V.

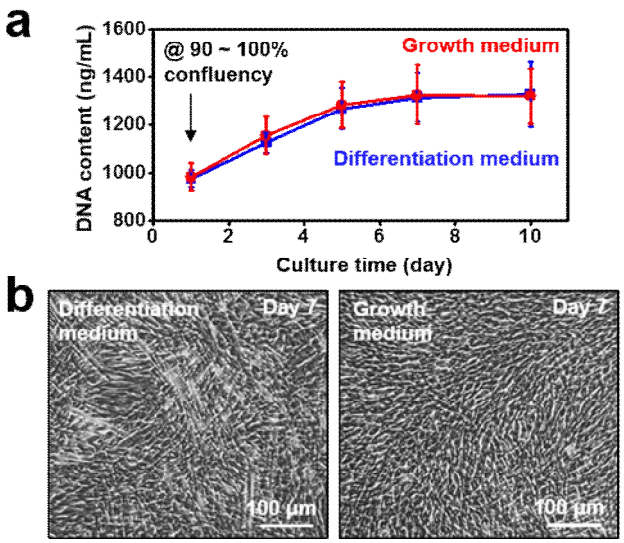

Figure 2.9 Cellular activities after treating two types of media

(a) DNA contents and (b) myotube formations of C2C12 myoblasts after treating growth or differentiation media.

2.2.3 Testing novel nanomaterials on a muscle-on-a-chip *in vitro.*

Testing novel biomolecules or pharmaceutical materials without sacrificing animals is an important goal that many researchers have been pursuing.[27–29] The cell-culture-substrate equipped with electronic sensors can provide quantitative information about changes in cellular condition within a short period of time which cannot be obtained by a microscope. As a demonstration, we design a skeletal muscle ischemia model using C2C12 myoblasts. The C2C12 myoblasts cultured on the cell-culture-platform for a concept of muscle-on-a-chip was aligned for mimicking *in vivo* native condition. Ischemia-induced reactive oxygen species (ROS) decrease cell viability and cause inflammation;[38] therefore, scavenging ROS is important. Several nanomaterials and molecules have been proposed to suppress ROS generation.[39] Ceria nanoparticles are an attractive candidate for this purpose (**Figure 2.10a**).[40] The relevant concentrations of hydrogen peroxide (H_2O_2) and ceria nanoparticles are optimized as shown in **Figure 2.10b-d**. Then, C2C12 myoblasts are exposed to 5 mM of H_2O_2 to simulate ischemia-induced ROS, and fluorescence images (**Figure 2.11a**) are obtained. The use of ceria nanoparticles improves cell viability, and quantitative comparison of living cells (**Figure 2.11b**) confirms the effects of ceria nanoparticles on ROS scavenging. This cell viability, represented by the impedance change,

can be monitored by the instrumented cell-culture-platform (**Figure 2.11c**). Treatment with 5 M H_2O_2 in differentiated C2C12 cells causes instant death in the majority of cells, resulting in a sudden, dramatic increase in impedance. Then impedance slowly decreases over 30 min as dead cells gradually detach from the substrate and conductive media flows between dead cells and electrodes. Treatment with 5 mM H_2O_2 induces similar but slower changes in impedance. However, treatment with 5 mM H_2O_2 in the presence of ceria nanoparticles yields only minimal changes in impedance.

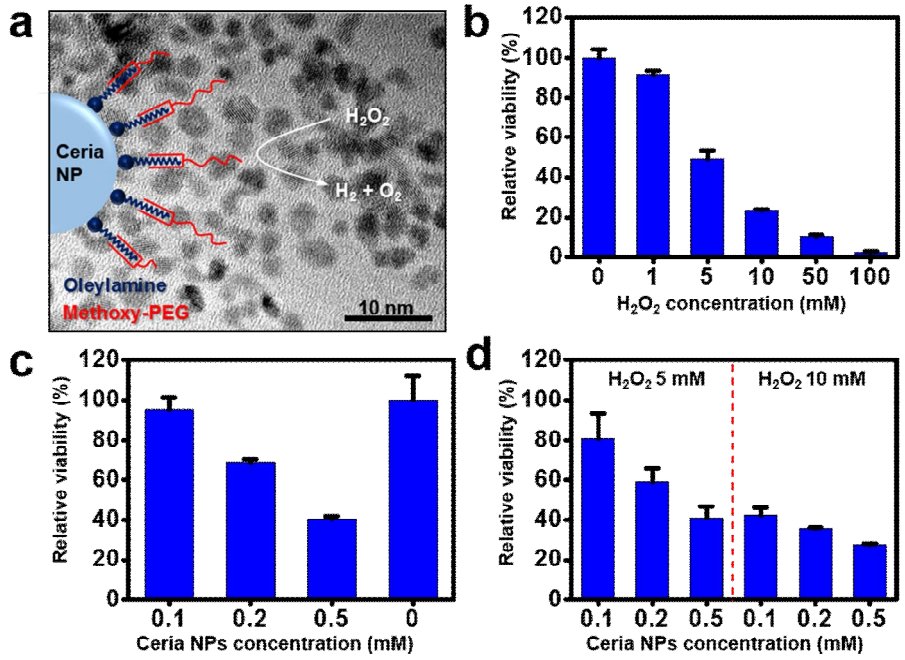

Figure 2.10 Function of ceria nanoparticles and optimization of those effects on cellular viability

(a) Schematic illustration and TEM image (background image) of ROS scavenging ceria nanoparticles. (b,c) A plot of relative viability of cells depending on the concentration of (b) hydrogen peroxide (H_2O_2) and (c) ceria nanoparticles (Ceria NPs). (d) A graph of relative viability of cells versus concentrations of Ceria NPs with 5 mM and 10 mM of H_2O_2 treatments. All data are acquired after treating H_2O_2 and Ceria NPs for 30 min, then the samples are incubated in the MTT solution for 3 h.

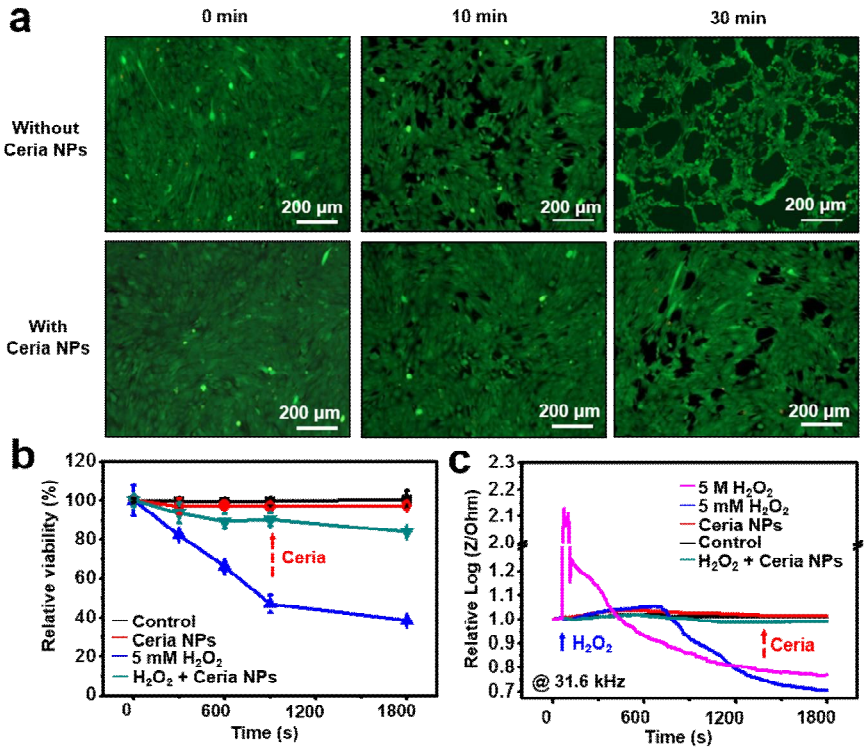

Figure 2.11 *In vitro* tests of the efficacy of ROS scavenging nanoparticles

(a) Fluorescence images (stained by LIVE/DEAD Viability Kit) of H_2O_2-exposed C2C12 cells with/without Ceria NPs at different time periods. (b) Relative viability plot from fluorescence images. (c) Plots of impedance as a function of time in different treatment groups.

2.2.4 Transfer printing cultured cell sheets *in vitro.*

Cell sheets cultured and differentiated on our soft instrumented cell-culture-platform can be applied to *in vivo* therapies *via* scaffold-free localized treatments. Through continuous monitoring of cells during the preparation of cell sheets, the cell condition and degree of differentiation can be confirmed before applying the cell sheets to biological systems, which can be carried out using transfer printing.[41] The transfer printing process of the cell sheet from the cell-culture-platform to the receiving substrate (protein-coated glass) is shown in **Figure 2.12**. The protein-coated glass can be assumed as the membrane of living tissue which is composed of proteins, where the slide glass is coated with 5 μg/cm^2 concentration of fibronectin. The complete process consists of two steps, preparation (on tissue culture polystyrene for 30 s) and transfer (on the receiving substrate for 90 s) step. The well-structured configuration and high viability of the transferred C2C12 cell sheet are observed by staining cells with hematoxylin and conducting viability assays (**Figure 2.13b and inset**). Differentiation characteristics are also maintained after the transfer printing (**Figure 2.13b**). **Figure 2.13c,d** present the effects of contact time during the transfer step (changes in cell-to-protein adhesion) and cell culture time (changes in cell density) on transfer yields, respectively. High transfer yields (~90%) are

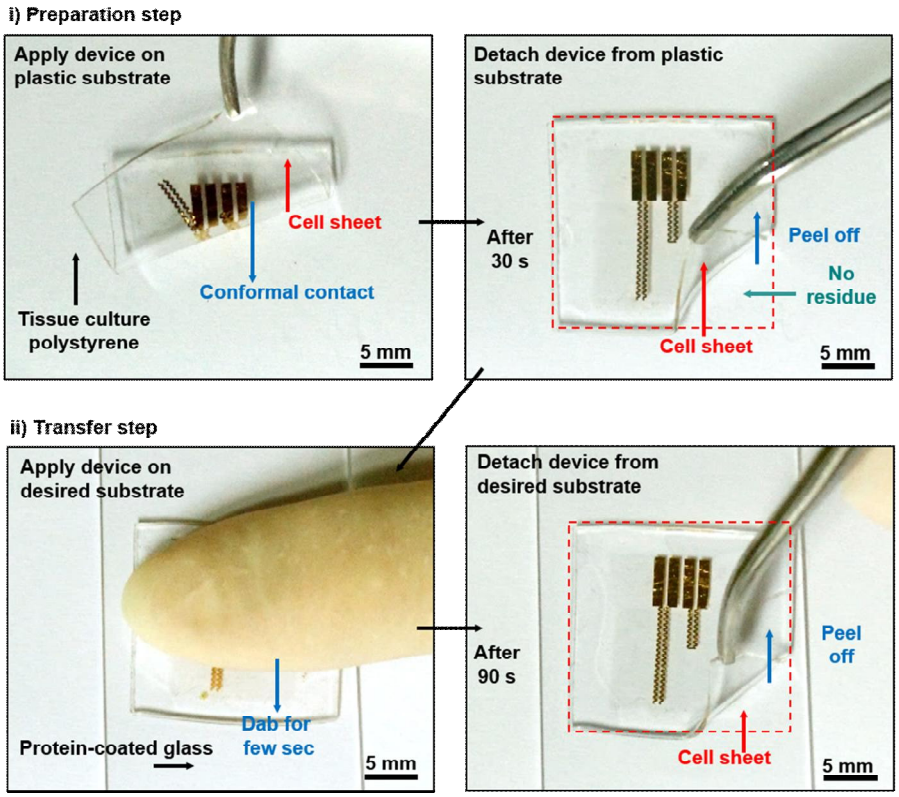

Figure 2.12 Images of the cell sheet transfer printing process. Two steps including preparation and transfer step are needed for transfer printing of C2C12 myoblast sheets.

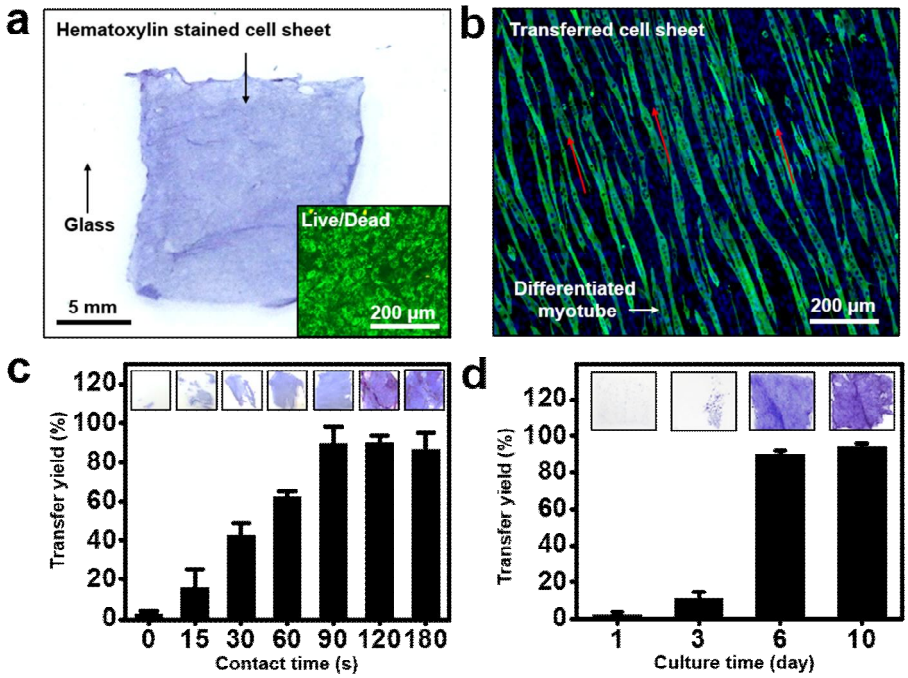

Figure 2.13 Transfer printing of C2C12 myoblast sheet

(a) Image of the transferred cell sheet stained with hematoxylin on the protein-coated glass substrate. The inset shows its LIVE/DEAD viability assay image. (b) The myosin heavy chains are maintained after the cell sheet transfer. The red arrows indicate the aligned orientation. (c,d) Plot of the transfer yields of cell sheets as a function of contact time in the transfer step (c) or as a function of culture time (d). The insets show images of transferred cell sheets.

obtained with contact time longer than 90 s and culture time longer than 6 days. **Figure 2.14** provide a schematic illustration of a triple-layered cell sheet prepared using multiple transfer printings and confocal microscope images of these sheets, respectively.

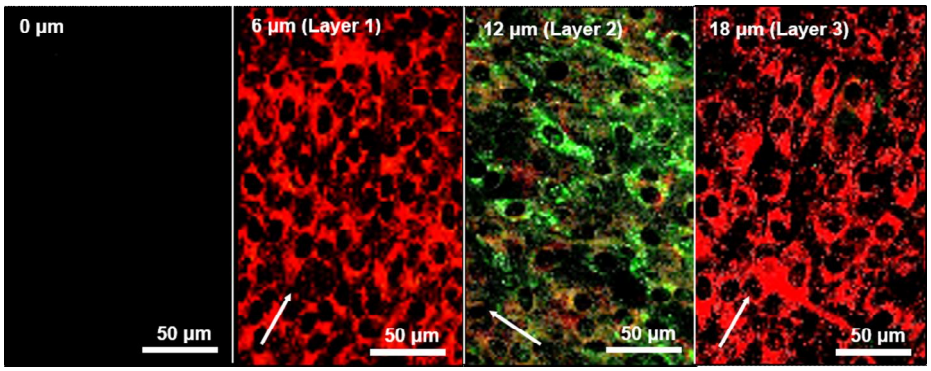

Figure 2.14 Three cell sheets transferred layer by layer with orthogonal orientations. Confocal images of the three-layered cell sheets. Images are captured at a depth interval of 6 µm. The white arrows indicate the direction of cell alignments

2.2.5 *In vivo* cell sheet transfer printing for the cell sheet therapy.

To investigate the therapeutic effects of *in vivo* cell sheet transfer printing on scarred muscles in mice, we use green fluorescent protein (GFP)-transfected C2C12 myoblasts and observing modalities to evaluate tissue organization. We graft aligned and differentiated monolayer or 5-layered C2C12 myoblast sheets onto the scarred area on the hindlimbs of mice (surgical procedure is described in **Figure 2.15**). The temperature changes during the cell sheet transfer printing are measured by the temperature sensor of the instrumented cell-culture-platform (**Figure 2.16**). Fast transfer printing (~90 s) causes minimal body temperature changes (~1.5 °C).

Transplanted cell sheets are labeled with a cell tracer (DiD) and monitored over time by measuring the fluorescence. Fluorescence is detected on the scar area, even after 7 days, while no signal is observed in the opposite hindlimb sites (see fluorescence data of 5-layered cell sheet in **Figure 2.17a;** IVIS Spectrum instrument (Perkin Elmer)). Fluorescence microscope images of sectioned tissue slices from transferred sites show the growth of the transplanted 5-layered cell sheets 7 days after transfer printing (**Figure 2.17b**), which is consistent with *in vivo* fluorescence imaging results. The capability to maintain the organization and function of transplanted cell

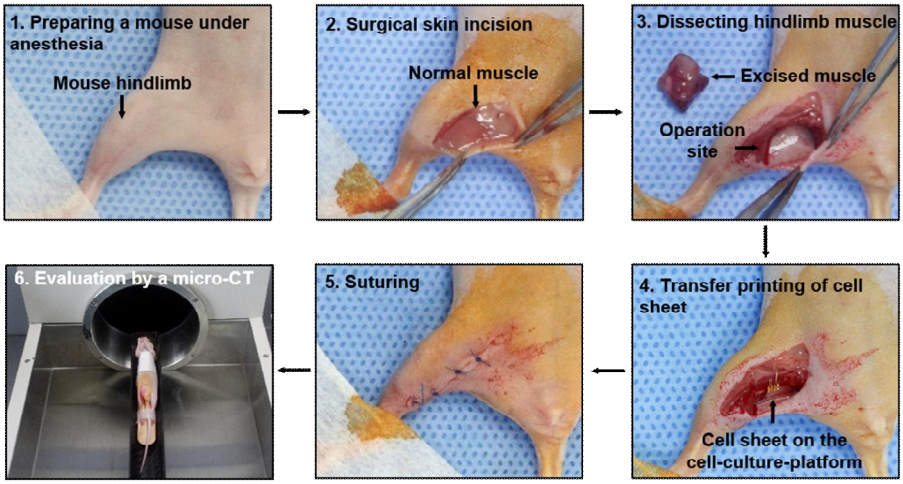

Figure 2.15 Images of surgery and cell sheet transfer printing in the scarred muscle model of a mouse

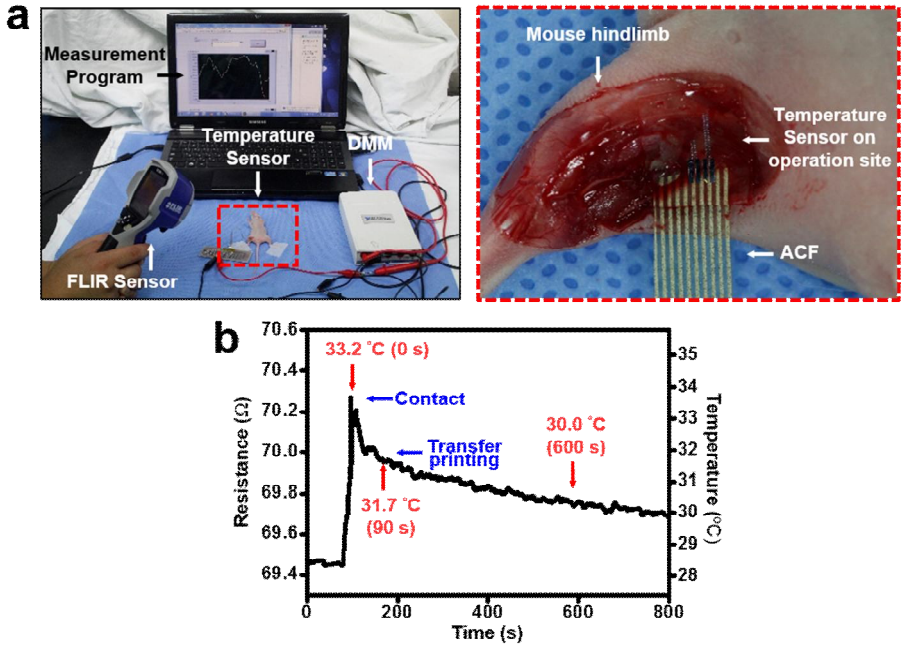

Figure 2.16 Measurement of temperature change with the instrumented cell-culture-platform during transfer printing of the cell sheet *in vivo*

(a) Images of the temperature sensing experiment. After dissecting muscle, the ACF-connected instrumented cell-culture-platform is placed on the operation site. (b) A plot of the time-dependent resistance change of the temperature sensor. The time-dependent temperature is also measured simultaneously by the commercial optical thermometer which is indicated by red arrows.

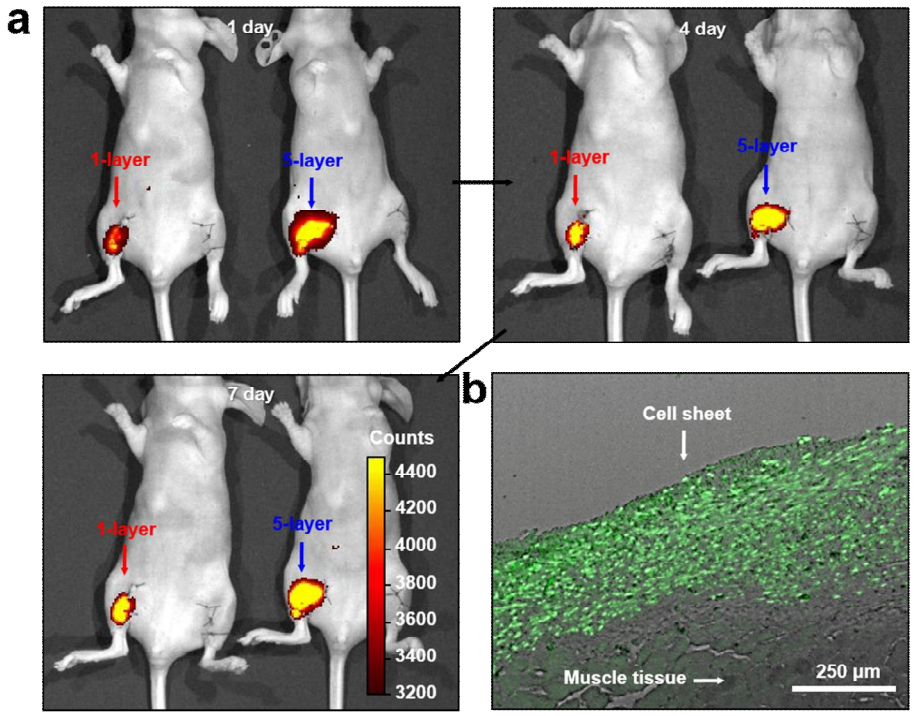

Figure 2.17 Maintenances and behaviors of C2C12 myoblasts after transfer printing *in vivo*

(a) Fluorescence imaging at 1 day (left) and 7 days (right) after transfer printing of the 5-layered C2C12 myoblast sheets labeled with cell tracers (DiD). (b) The proliferation of transfer-printed cells (GFP-expressing C2C12 myoblasts) at the operation site 7 days after transplantation.

sheet can maximize the therapeutic effect of localized cell therapy at the wound site.

Micro-computed tomography (micro-CT) also confirms the growth of muscular tissues in the transplanted region (**Figure 2.18a**). The white arrows indicate the operation site. Comparison between the first and second frame of **Figure 2.18a** highlights removed muscle tissues. Importantly, 7 days after transplantation of the cell sheet, muscle tissues are regenerated (**Figure 2.18a** third frame), while no recovery is observed without cell sheet transfer after the surgery (**Figure 2.18a** fourth frame; the inset shows the pre-operation image of negative experiment group). Hematoxylin and eosin staining images reveal that the 5-layered cell sheets have grown at transferred sites (**Figure 2.18b**). On the other hand, atrophic changes in muscles occur in the scarred muscles without cell sheet transplantation (**Figure 2.18c**). The abundant proliferation and differentiation of C2C12 myoblasts in 5-layered cell sheets transferred into scarred muscle sites are observed through the detection of GFP expression, as shown in **Figure 2.18d,e**. Vascularization is also observed by CD31 staining (**Figure 2.18f**).

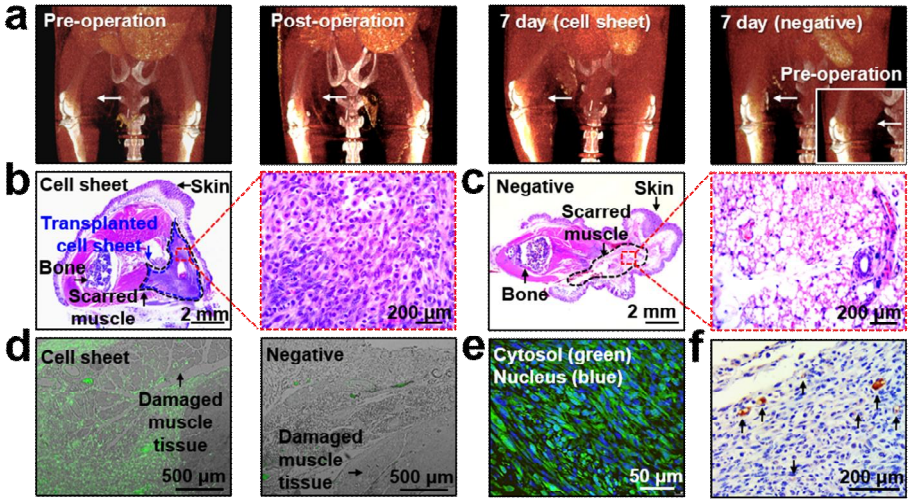

Figure 2.18 Investigation of therapeutic effects

(a) CT images of the operated mice: (from left to right) pre-operation, post-operation, 7 days after cell sheet transplantation (5-layered), and negative control (no cell sheet transplantation). The white arrows indicate the operation site. The inset shows the pre-operation image of the negative experiment group. (b,c) Hematoxylin and eosin staining of the operated hindlimb 7 days after transplantation of the cell sheet and without the cell sheet transplantation (negative control) for morphological observations. (d) Proliferation of the cell sheet around the damaged muscles, as shown by expression of GFP. (e) Differentiation of the cell sheet around the damaged muscles. (f) Vascularization (black arrows) in the region of transferred cell sheets 7 days after transplantation.

2.3 Conclusion

Our soft instrumented cell-culture-platform provides not only its originally dedicated function (acting as an ECM for tissue engineering) but also novel functions, such as aligning plated cells, monitoring physiological cues, testing new nanomaterials *in vitro*, and transfer printing cell sheets to *in vivo* systems. In our study, graphene nanoribbons had enhanced cell adhesion, promoted differentiation, and led to anisotropic arrangement of C2C12 myoblasts, mimicking the native muscle tissue. Additionally, the characteristics of cultured cells could be monitored by integrated sensors (impedance, conductance, and temperature). We have also used the muscle-on-a-chip platform to ascertain the effects of ceria nanoparticles on ROS scavenging. By engineering the interface between the current platform and cell sheet through a preparation step, we have successfully developed a safe, simple, and highly efficient protocol for *in vitro* and *in vivo* cell sheet transfer printing. The theoretical analysis enlightens the underlying mechanics and physics of the transfer printing protocol, which can provide fundamental insights on the transfer printing of cell sheet for broader users, such as clinicians. In summary, the soft instrumented cell-culture-platform delivers innovative multipurpose cell culture systems and contributes for the research and development of the tissue engineering. It broadens the range of

in vitro applications, such as deliberate cell regulations, *in situ* and real-time physiological monitoring, and simple yet precise drug screening, as well as enables clinically effective *in vivo* therapeutic applications. Further work will focus on new applications of the current platform to other disease models.

2.4 Experimental

2.4.1 Fabrication of the soft instrumented cell-culture-platform

Graphene was synthesized using the chemical vapor deposition (CVD) growth process[42] and was grown on copper foil (Alfa Aesar) at 1000 °C with a mixture of methane (20 sccm, 1.6 torr) and hydrogen (8.4 sccm, 0.8 torr). Ni was deposited onto the Si wafer (test grade, 4Scinece) by thermal evaporation. Next, 7 nm of Cr and 150 nm of Au were deposited onto Ni-deposited Si wafers by thermal evaporation, and patterned by photolithography and wet etching. Then, the graphene was transferred onto the sample and patterned with 5 μm lines and 5 μm spaces with photolithography and reactive ion etching (RIE) using O_2 plasma (O_2 flow rate of 100 sccm, chamber pressure of 100 mtorr, 150 W RF power for 25 s). The sample was spin coated with poly(methyl methacrylate) (PMMA; A4, Microchem; ~300 nm) at 3000 rpm for 30 s and was then immersed in Ni etchant for 30 min. The sample was transferred onto low-modulus PDMS (Sylgard 527, Dow Corning; part A to B in ratio of 1:2; thickness of 600 μm), and dried in an oven at 70 °C for 10 min. Finally, the PMMA was removed with acetone. The elastic modulus of the sample was measured with a digital force meter (Mark-10). Electrical measurements by impedance and

temperature sensors were carried out with an electrochemical workstation (CHI660E, CH Instrument) and a parameter analyzer (B1500A, Agilent), respectively, which were connected with anisotropic conductive films (ACFs).

2.4.2 Measurement of the protein interaction force of graphene

All data describing the adhesion forces between fibronectin molecules and graphene were obtained by an atomic force microscope (AFM, Dimension Icon, Bruker). For functionalization of the AFM tip with fibronectin, the tip was cleaned with a UV/ozone cleaner (Yuil Ultra Violet System) for 3 min, following by additional cleaning with acetone. Next, the tip was soaked in fibronectin solution (5 μg/mL in distilled water; Invitrogen) and completely dried at room temperature. Spring constants of cantilevers (ScanAsyst-Air, Bruker probes) were calibrated using the thermal tune function, and all AFM experiments were conducted in PeakForce QNM mode.

2.4.3 Cell culture

C2C12 myoblasts (CRL-1772; ATCC), human dermal fibroblasts (PCS-201-012; ATCC), and human mesenchymal stem cell (PT-2501;

Lonza) were used for experiments. C2C12 myoblasts and human dermal fibroblasts were cultured in Dulbecco's modified Eagle's medium (DMEM) supplemented with 10% fetal bovine serum (FBS) and 1% penicillin-streptomycin (PS). Human mesenchymal stem cells were cultured in MSCGM^{TM} mesenchymal stem cell growth medium (Lonza). The cells were cultured under the standard culture conditions of 37 °C and 5% CO_2. The cells were seeded onto the cell-culture-platform at different densities according to each experiment: 2×10^4 cells/cm^2 for observation of cellular behaviors on the patterned graphene nanoribbons and measuring electrical signals of cells, or 5×10^4 cells/cm^2 to demonstrate the muscle-on-a-chip and transfer printing of cell sheets.

2.4.4 Cellular characteristics on patterned graphene

The C2C12 cell alignment on the patterned graphene was monitored by the differential interference contrast (DIC) mode using a confocal microscope (TCS SP8 STDE, Leica). DIC images of cell alignment were captured in every 15 min for 48 h while incubating in the standard culture condition. To observe the alignment of cytoskeletal actin, the cells were counter stained with rhodamine phalloidine (1:100 dilution; Life Technologies). To observe myotube formation, the cultured cells were

stained with anti-myosin heavy chain antibodies (1:100 dilution; Abcam). The cells were counter stained with DAPI and observed under a fluorescence microscope (Eclipse Ti, Nikon).

2.4.5 Preparation of ceria nanoparticles

To synthesize ceria nanoparticles, 1 mM (0.4 g) of cerium (III) acetate (98%, Sigma-Aldrich) and 12 mM (3.2 g) of oleylamine (approximate C18 content of 80%–90%, AcrosOrganics) were added to 15 mL xylene (98.5%, Sigma-Aldrich). The mixed solution was sonicated for 15 min at room temperature and then heated up to 90 °C. One milliliter of distilled water was injected into the solution under vigorous stirring at 90 °C, and the solution color changed to an off-white color, indicating that the reaction had occurred. The resulting mixture was aged for 3 h at 90 °C to give a light yellow colloidal solution, which was then cooled to room temperature. Acetone (100 mL) was added to the precipitated ceria nanoparticles. The precipitate was washed with acetone using centrifugation, and the resulting ceria nanoparticles were easily dispersible in organic solvents, *e.g.*, chloroform. For the synthesis of phospholipid-PEG-capped ceria nanoparticles, the ceria nanoparticles dispersed in chloroform were encapsulated by PEG-phospholipid shell. First, 3 mL ceria nanoparticles in

$CHCl_3$ (10 mg/mL) was mixed with 3 mL $CHCl_3$ solution containing 30 mg of mPEG-2000 PE. The solvent was then evaporated using a rotary evaporator and incubated at 70 °C in a vacuum for 1 h to completely remove the chloroform. The addition of 5 mL distilled water yielded a clear and light-yellowish suspension. After filtration, excess mPEG-2000 PE was removed using ultracentrifugation. Purified phospholipid-PEG-capped ceria nanoparticles were dispersed in distilled water.

2.4.6 Multi-layered cell sheet

Three samples of cell sheets were prepared on the cell-culture-platform, where each cell sheet was previously stained with fluorescence dye, colored with DiD (red; two samples; Invitrogen) or DiO (green; one sample; Invitrogen). Each cell sheet was transferred in the order of red, green, red, and sheets were stacked on top of each other. The arrangement of multi-layered cell sheets was observed using a confocal microscope (TCS SP8 STDE, Leica). To clearly visualize each cell sheet, the color intensities of the captured images were modified using the Leica Application Suite (Leica).

2.4.7 Mouse scarred muscle model

All experiments on animals were approved by the animal care

committee at Seoul National University Hospital. Six-week-old male BALB/c nude mice were anesthetized by intraperitoneal injection with a mixture of zolazepam and xylazine. A surgical skin incision (1.5 cm) was made in the ventral aspect of the right thigh beginning near the groin. Subsequently, the medial thigh muscle was dissected 5 mm proximal to and along the course of the deep femoral branch. The dissection continued laterally 5 mm from and along the bundle of the femoral nerve, artery, and vein. The entire medial thigh muscle was excised.

2.4.8 Micro-CT

After the cell sheet transplantation (1 layer, 5 layers, or none; each group N = 4) to the scarred muscles in the hindlimb, the therapeutic effect was monitored over time by micro-CT. The micro-CT was performed using a cone-beam type commercial preclinical CT scanner (NFR-Polaris-G90C, NanoFocusRay) with the following imaging parameters: tube voltage, 50 kVp; tube current, 100 μA; field of view, 35 mm × 35 mm; matrix, 512 × 512; slice thickness, 0.054 mm. Three-dimensional reconstructed images were obtained using OsiriX (version 4.0, 32 bit, OsiriX Foundation).

2.4.9 *In vivo* fluorescent imaging

For fluorescent imaging, Balb/c nude mice (female, ages 6 ~ 8 weeks) were subjected to operation with cell tracer (DiD)-labeled GFP-expressing cell sheets and anesthetized by intraperitoneal injection. Measurements of the fluorescence signal from each cell sheet were made using Living Image Software 4.0 (Perkin Elmer).

2.4.10 Histology

All tissues were embedded in paraffin and sectioned to 4-μm thickness. Histology samples for morphology visualization were stained by hematoxylin and eosin using standard protocols. For immunofluorescence staining, the specimens were then stained with primary anti-GFP antibodies (Santa Cruz Biotechnology) according to the manufacturer's instructions. Protein expression was visualized with Alexa Fluor 488-conjugated secondary antibodies (Invitrogen). All images were acquired using an inverted fluorescence microscope (DM5500 B, Leica). In order to detect vascularization in organized tissues from the cell sheet, immunohistochemistry was performed using the following steps with anti-CD31 antibodies (Novus Biologicals). First, endogenous peroxidase and protein were blocked with a solution of 0.3% H_2O_2 and goat serum (Dako) to prevent nonspecific antibody binding. After 30 min, the tissues were then

incubated with the primary anti-CD31 antibody for 1 h, washed, and incubated with horseradish peroxidase-conjugated goat anti-rabbit secondary antibodies (Santa Cruz Biotechnology) for 1 h. After additional washes, vascularization was evaluated by staining with 3,3′-diaminobenzidine (DAB) peroxidase substrate (Dako).

2.5 References

1. Levenberg, S., Huang, N. F., Lavik, E., Rogers, A. B., Itskovitz-Eldor, J. & Langer, R. Differentiation of human embryonic stem cells on three-dimensional polymer scaffolds. *Proc. Natl. Acad. Sci. U. S. A.* **100**, 12741-12746 (2003).
2. Dvir, T., Timko, B. P., Kohane, D. S. & Langer, R. Nanotechnological strategies for engineering complex tissues. *Nat. Nanotechnol.* **6**, 13-22 (2011).
3. Sun, J. Y., Zhao, X., Illeperuma, W.R., Chaudhuri, O., Oh, K. H., Mooney, D. J., Vlassak, J. J. & Suo, Z. Highly stretchable and tough hydrogels. *Nature* **489**, 133-136 (2012).
4. Tian, B., Liu, J., Dvir, T., Jin, L., Tsui, J. H., Qing, Q., Suo, Z., Langer, R., Kohane, D, S. & Lieber, C. M. Macroporous nanowire nanoelectronic scaffolds for synthetic tissues. *Nat. Mater.* **11**, 969-994 (2012).
5. Straub, B., Meyer, E. & Fromherz, P. Recombinant maxi-K channels on transistor, a prototype of iono-electronic interfacing. *Nat. Biotechnol.* **19**, 121-124 (2001).
6. Sekitani, T., Zschieschang, U., Klauk, H. & Someya, T. Flexible organic transistors and circuits with extreme bending stability. *Nat. Mater.* **9**, 1015-1022 (2010).

7. Viventi, J., Kim, D. H., Vigeland, L., Frechette, E. S., Blanco, J. A., Kim, Y. S., Avrin, A. E., Tiruvadi, V. R., Hwang, S. W., Vanleer, A. C., Wulsin, D, F., Davis, K., Gelber, C, E., Palmer, L., Van, der, Spiegel, J., Wu, J., Xiao, J., Huang, Y., Contreras, D., Rogers, J, A. & Litt, B. Flexible, foldable, actively multiplexed, high-density electrode array for mapping brain activity *in vivo*. *Nat. Neurosci.* **14**, 1599-1605 (2011).

8. Sekitani, T., Noguchi, Y., Hata, K., Fukushima, T., Aida, T. & Someya, T. A rubberlike stretchable active matrix using elastic conductors. *Science* **321**, 1468-1472 (2008).

9. Kim, D,-H., Lu, N., Ma, R., Kim, Y,-S., Kim, R,-H., Wang, S., Wu, J., Won, S, M., Tao, H., Islam, A., Yu, K, J., Kim, T,-i., Chowdhury, R., Ying, M., Xu, L., Li, M., Chung, H,-J., Keum, H., McCormick, M., Liu, P., Zhang, Y,-W., Omenetto, F, G., Huang, Y., Coleman, T. & Rogers, J, A. Epidermal electronics. *Science* **333**, 838-843 (2011).

10. Keplinger, C., Sun, J. Y., Foo, C. C., Rothemund, P., Whitesides, G. M. & Suo, Z. Stretchable, transparent, ionic conductors. *Science* **341**, 984-987 (2013).

11. Son, D., Lee, J., Qiao, S., Ghaffari, R., Kim, J., Lee, J, E., Song, C., Kim, S, J., Lee, D, J., Jun, S, W., Yang, S., Park, M., Shin, J., Do, K., Lee, M., Kang, K., Hwang, C, S., Lu, N., Hyeon, T. & Kim, D, H. Multifunctional

wearable devices for diagnosis and therapy of movement disorders. *Nat. Nanotechnol.* **9**, 397-404 (2014).

12. Park, Y. J., Lee, S. K., Kim, M. S., Kim, H. & Ahn, J. H. Graphene-based conformal devices. *ACS Nano* **8**, 7655-7662 (2014).

13. Nishida, K., Yamato, M., Hayashida, Y., Watanabe, K., Yamamoto, K., Adachi, E., Nagai, S., Kikuchi, A., Maeda, N., Watanabe, H., Okano, T. & Tano, Y. Corneal reconstruction with tissue-engineered cell sheets composed of autologous oral mucosal epithelium. *N. Engl. J. Med.* **351**, 1187-1196 (2004).

14. Iwata, T., Yamato, M., Tsuchioka, H., Takagi, R., Mukobata, S., Washio, K., Okano, T. & Ishikawa, I. Periodontal regeneration with multi-layered periodontal ligament-derived cell sheets in a canine model. *Biomaterials* **30**, 2716-2723 (2009).

15. Miyahara, Y., Nagaya, N., Kataoka, M., Yanagawa, B., Tanaka, K., Hao, H., Ishino, K., Ishida, H., Shimizu, T., Kangawa, K., Sano, S., Okano, T., Kitamura, S. & Mori, H. Monolayered mesenchymal stem cells repair scarred myocardium after myocardial infarction. *Nat. Med.* **12**, 459-465 (2006).

16. Akiyama, Y., Kikuchi, A., Yamato, M., Okano, T. Ultrathin poly(N-isopropylacrylamide) grafted layer on polystyrene surfaces for cell

adhesion/detachment control. *Langmuir* **20**, 5506-5511 (2004).

17. Engler, A. J., Sen, S., Sweeney, H. L. & Discher, D. E. Matrix elasticity directs stem cell lineage specification. *Cell* **126**, 677-689 (2006).

18. Kim, D. H., Song, J., Choi, W. M., Kim, H. S., Kim, R. H., Liu, Z., Huang, Y. Y., Hwang, K. C., Zhang, Y. & Rogers, J. A. Materials and noncoplanar mesh designs for integrated circuits with linear elastic responses to extreme mechanical deformations. *Proc. Natl. Acad. Sci. U. S. A.* **105**, 18675-18680 (2008).

19. Bowden, N., Brittain, S., Evans, A. G., Hutchinson, J. W. & Whitesides, G. M. Spontaneous formation of odered structures in thin films of metals supported on an elastomeric polymer. *Nature* **393**, 146-149 (1998).

20. Khang, D. Y., Jiang, H., Huang, Y. & Rogers, J. A. A stretchable form of single-crystal silicon for high-performance electronics on rubber substrates. *Science* **311**, 208-212 (2006).

21. Jiang, H., Khang, D. Y., Song, J., Sun, Y., Huang, Y., Rogers, J. A. Finite deformation mechanics in buckled thin films on compliant supports. *Proc. Natl. Acad. Sci. U. S. A.* **104**, 15607-15612 (2007).

22. Park, S. Y., Park, J., Sim, S. H., Sung, M. G., Kim, K. S., Hong, B. H. & Hong, S. Enhanced differentiation of human neural stem cells into neurons on graphene. *Adv. Mater.* **23**, H263-H267 (2011).

23. Hong, S. W., Lee, J. H., Kang, S. H., Hwang, E. Y., Hwang, Y. S., Lee, M. H., Han, D. W. & Park, J. C. Enhanced neural cell adhesion and neurite outgrowth on graphene-based biomimetic substrates. *BioMed Res. Int.* **2014**, 212149 (2014).

24. Bajaj, P., Rivera, J. A., Marchwiany, D., Solovyeva, V. & Bashir, R. Graphene-based patterning and differentiation of C2C12 myoblasts. *Adv. Healthc. Mater.* **3**, 995-1000 (2014).

25. Park, J., Park, S., Ryu, S., Bhang, S. H., Kim, J., Yoon, J. K., Park, Y. H., Cho, S. P., Lee, S., Hong, B. H. & Kim, B, S. Graphene-regulated cardiomyogenic differentiation process of mesenchymal stem cells by enhancing the expression of extracellular matrix proteins and cell signaling molecules. *Adv. Healthc. Mater.* **3**, 176-181 (2014).

26. Kim, K. S., Zhao, Y., Jang, H., Lee, S. Y., Kim, J. M., Kim, K. S., Ahn, J. H., Kim, P., Choi, J. Y. & Hong, B. H. Large-scale pattern growth of graphene films for stretchable transparent electrodes. *Nature* **457**, 706-710 (2009).

27. Huh, D., Matthews, B. D., Mammoto, A., Montoya-Zavala, M., Hsin, H. Y. & Ingber, D. E. Reconstituting organ-level lung functions on a chip. *Science* **328**, 1662-1668 (2010).

28. Huh, D., Hamilton, G. A. & Ingber, D. E. From 3d cell culture to organs-

on-chips. *Trends Cell Biol.* **21**, 745-754 (2011).

29. Huh, D., Leslie, D. C., Matthews, B. D., Fraser, J. P., Jurek, S., Hamilton, G. A., Thorneloe, K. S., McAlexander, M. A. & Ingber, D. E. A human disease model of drug toxicity-induced pulmonary edema in a lung-on-a-chip microdevice. *Sci. Transl. Med.* **4**, 159ra147 (2012).

30. Guo, J. J., Yao, X. J., Ning, L. L., Wang, Q. Q. & Liu, H. X. The adsorption mechanism and induced conformational changes of three typical proteins with different secondary structural features on graphene. *RSC Adv.* **4**, 9953-9962 (2014).

31. Sawyer, A. A., Hennessy, K. M. & Bellis, S. L. Regulation of mesenchymal stem cell attachment and spreading on hydroxyapatite by RGD peptides and adsorbed serum proteins. *Biomaterials* **26**, 1467-1475 (2005).

32. Boontheekul, T., Hill, E. E., Kong, H. J. & Mooney, D. J. Regulating myoblast phenotype through controlled gel stiffness and degradation. *Tissue Eng.* **13**, 1431-1442 (2007).

33. Bagnaninchi, P. O. & Drummond, N. Real-time label-free monitoring of adipose-derived stem cell differentiation with electric cell-substrate impedance sensing. *Proc. Natl. Acad. Sci. U. S. A.* **108**, 6462-6467 (2011).

34. Kim, D. H., Ghaffari, R., Lu, N., Wang, S., Lee, S. P., Keum, H.,

D'Angelo, R., Klinker, L., Su, Y., Lu, C., Kim, Y, S., Ameen, A., Li, Y., Zhang, Y., de, Graff, B., Hsu, Y, Y., Liu, Z., Ruskin, J., Xu, L., Lu, C., Omenetto, F, G., Huang, Y., Mansour, M., Slepian, M, J. & Rogers, J, A. Electronic sensor and actuator webs for large-area complex geometry cardiac mapping and therapy. *Proc. Natl. Acad. Sci. U. S. A.* **109**, 19910-19915 (2012).

35. Wegener, J., Keese, C. R. & Giaever, I. Electric cell-substrate impedance sensing (ECIS) as a noninvasive means to monitor the kinetics of cell spreading to artificial surfaces. *Exp. Cell Res.* **259**, 158-166 (2000).

36. Rakhilin, S., Turner, G., Katz, M., Warden, R., Irelan, J., Abassi, Y. A. & Glass, D. J. Electrical impedance as a novel biomarker of myotube atrophy and hypertrophy. *J. Biomol. Screen.* **16**, 565-574 (2011).

37. Murphy, S, M., Kiely, M., Jakeman, P, M., Kiely, P, A. & Carson B, P. Optimization of an in vitro bioassay to monitor growth and formation of myotubes in real time. *Biosci. Rep.* **36**, pii: e00330 (2016).

38. Eltzschig, H. K. & Eckle, T. Ischemia and reperfusion--from mechanism to translation. *Nat. Med.* **17**, 1391-1401 (2011).

39. Karakoti, A., Singh, S., Dowding, J. M., Seal, S. & Self, W. T. Redox-active radical scavenging nanomaterials. *Chem. Soc. Rev.* **39**, 4422-4432 (2010).

40. Kim, C. K., Kim, T., Choi, I. Y., Soh, M., Kim, D., Kim, Y. J., Jang, H., Yang, H. S., Kim, J. Y., Park, H. K., Park, S, P., Park, S., Yu, T., Yoon, B, W., Lee, S, H. & Hyeon, T. Ceria nanoparticles that can protect against ischemic stroke. *Angew. Chem. Int. Ed. Engl.* **51**, 11039-11043 (2012).

41. Carlson, A., Bowen, A. M., Huang, Y., Nuzzo, R. G. & Rogers, J. A. Transfer printing techniques for materials assembly and micro/nanodevice fabrication. *Adv. Mater.* **24**, 5284-5318 (2012).

42. Bae, S., Kim, H., Lee, Y., Xu, X., Park, J. S., Zheng, Y., Balakrishnan, J., Lei, T., Kim, H. R., Song, Y. I., Kim, Y, J., Kim, K, S., Ozyilmaz, B., Ahn, J, H., Hong, B, H. & Iijima, S. Roll-to-roll production of 30-inch graphene films for transparent electrodes. *Nat. Nanotechnol.* **5**, 574-578 (2010).

Chapter 3. Soft Cell-Sheet-Graphene Hybrid Device for Electrophysiological Applications of Skeletal Muscles

3.1 Introduction

Recently, the importance of the diagnosis of electrophysiological status of native muscles is drastically increased for reducing the many motor neuron disorders[1] such as Duchenne muscular dystrophy,[2] spinal muscular atrophy,[3] and Parkinson's disease.[4] Conventional feedback therapeutic actuations by using electrical stimulatior[5,6] and/or drug,[7-9] for relieving those symptoms are commonly accompanied. Although implantable devices play a critical role in the diagnosis and therapy of these neuromuscular disorders, those used in the past were bulky and mechanically rigid. The mechanical mismatch between conventional rigid devices[10] and soft tissues[11,12] with curved shapes has caused non-conformal contacts/interfaces, a low signal to noise ratio, mechanical fatigue, and occasionally inflammation arising from local friction as well as scarring.[13] On this account, soft bioelectronics based on flexible/stretchable devices[14-19] have been highlighted as a potential solution to these issues.

Multi-modal therapeutic functions are another essential feature that should optimally be integrated within an implantable bioelectronic system. Electrical stimulation on the spinal cord[5] and/or neurons[20] has provided effective therapies for limb paralysis. Electrical fatigue, however, sometimes arises from this method.[21] Optical stimulation at target wound sites has been proposed as an alternative strategy and has shown promise for brain stimulation,[17,22,23] although simultaneous electrophysiological recording from optically stimulated tissues with metal electrodes is challenging owing to spatial misalignment of the light source and non-transparent electrodes. Another conventional therapy is to load drugs onto a device, which is then implanted to deliver the cargo to the target area.[24,25] However, the process of drug-incorporation within implantable devices is complicated and multiple drug reloading is difficult.[26,27] The transplantation of cultured cells is thereby emerging as an alternative therapeutic procedure in many diseases and has shown to be effective for tissue regeneration at wound sites.[28,29] In addition, coating muscle cells onto an implantable device improves the interface between the device and adjacent tissues,[30] moving toward the desired high-quality biotic/abiotic interface that would enable efficient stimulation therapy with simultaneous monitoring.

Here, we develop a soft and instrumented cell-sheet-graphene

hybrid made of biocompatible materials.[31-34] The device is composed of a cell-sheet-graphene hybrid, an aligned C2C12 myoblasts sheet (~10 μm)[31] integrated on buckled, Au-doped, and mesh-patterned graphene electrodes (~5 nm),[32] which is mounted on a sub-micron-thick polyimide (PI) membrane (~600 nm)[33] and a soft polydimethylsiloxane (PDMS) substrate (500 μm) (**Figure 3.1a,b**).[34] All materials are stable and biocompatible *in vivo* according to previous reports.[31-34] chronic immune responses in the long-term implantation study should be observed in the future. Serpentine-shaped, mesh-patterned graphene electrodes (~50 μm width; **Figure 3.1c**) are used to improve stretchability and softness of the system. The electrodes also monitor and promote proliferation and differentiation of muscle cells *in vitro*[35,36] as well as serve as an electrical stimulator and electrophysiology sensor *in vivo*. Au doping on the graphene mesh electrodes allows low impedance and high conductivity.[18,37] The anisotropic buckled structure (**Figure 3.1b**) induces cell alignment and incresease softness.[38] The cell-sheet-graphene hybrid is comprised of transparent materials and thereby can be transversed by the visible light (**Figure 3.2**). The stretched system without buckles and light diffraction/scattering shows even better transmittance (**Figure 3.2a,b**). Implantation of the system, which includes a cell sheet, enables cell therapy as well as high-quality bio-interface

formation (**Figure 3.2c**). Transparency allows the genetically modified muscle tissues underneath the hybrid to be excited by optical stimulation (**Figure 3.2d**). We also examine the effectiveness of the integrated system in the diagnosis and therapy of neuromuscular diseases through *in vitro* and *in vivo* studies.

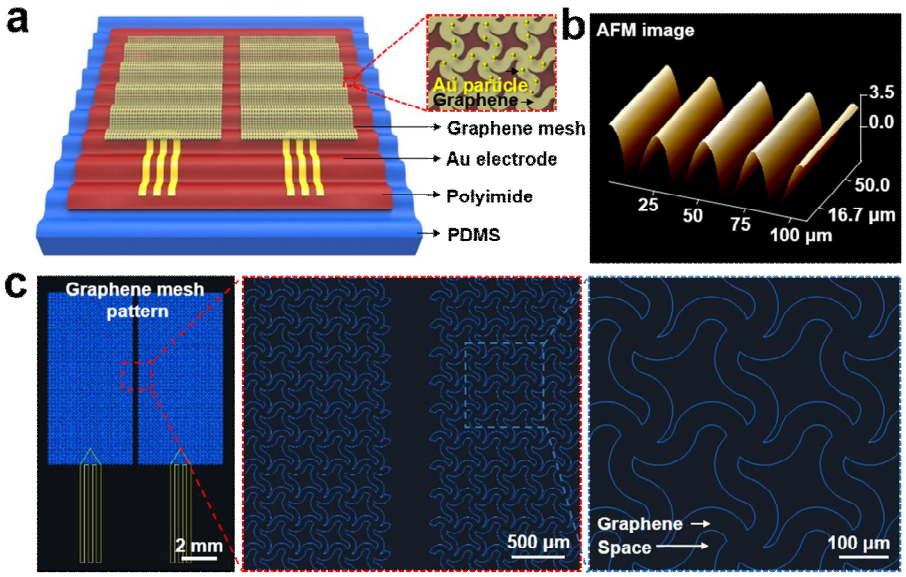

Figure 3.1 Overview of the architecture and detailed electrode design of the soft cell-sheet-graphene hybrid device

(a) The hybrid is composed of a C2C12 myoblasts sheet, an ultrathin graphene mesh, and Au nanomembrane connective electrodes, and is mounted on sub-micron polyimide on a PDMS substrate with buckled topology. The graphene mesh is doped with Au particles (top red box). b) Atomic force microscope (AFM) image of the buckled graphene mesh. (c) AutoCAD designs of mesh-patterned graphene electrodes. Serpentine electrodes (width of 50 μm) patterned into mesh structure. Two mesh electrodes are spaced 300 μm apart.

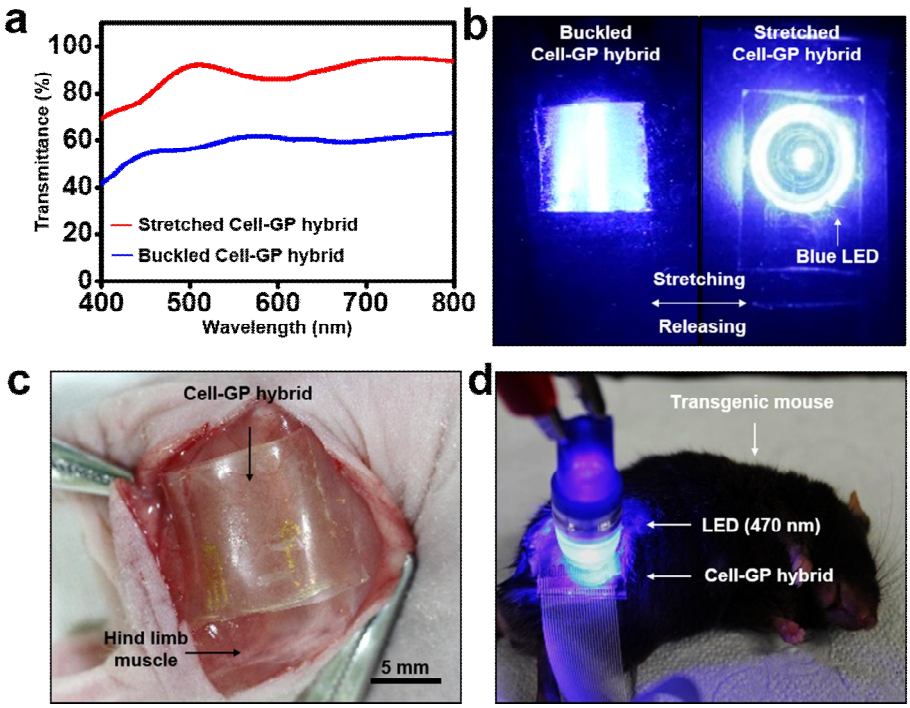

Figure 3.2 Optical properties of the hybrid devices

(a) A plot of optical transmittances (from 400 nm to 800 nm of wavelength). (b) Photographic images (with 470 nm LED) of the hybrid during buckled and stretched states. (c) Implantation of the transparent and soft cell-sheet-graphene hybrid onto target site of a nude mouse *in vivo*. (d) Image of a ChR2-expressing transgenic mouse (*Thy1-ChR2*) and its optogenetic application using the cell-sheet-graphene hybrid device. For optical stimulation, a 470 nm LED is located on top of the transparent cell-sheet-graphene hybrid.

3.2 Results and Discussion

3.2.1 Fabrication of cell-sheet-graphene hybrid

Graphene layers on a copper foil are grown using chemical vapor deposition following protocols described in previous reports.[35,39] A 30 nm Ni layer is deposited onto the Si wafer and, subsequently, 7 nm/70 nm Cr/Au are deposited onto the Ni layer using thermal evaporation. Cr and Au layers are patterned by photolithography and wet etching. Then, the graphene sheet is transferred onto the sample and doped with $AuCl_4$ in nitromethane.[37] The doped sheet is patterned by photolithography and reactive ion etching. The patterned sample is transferred onto the polyimide layer coated on the Ni/Si wafer. The patterned sample on the PI is transferred onto the prestretched (30%) PDMS and dried under 70 °C for 10 min. Then prestrain of the PDMS is slowly released to form the buckled graphene mesh (**Figure 3.3a**). Before seeding C2C12 myoblasts, the buckled graphene mesh is sterilized with 70% ethanol for 15 min under ultraviolet (UV) light and rinsed with PBS solution for 15 min under UV light twice. To prepare cell-sheet-graphene hybrid, C2C12 myoblasts are seeded on the sample with a density of 5×10^4 cells/cm^2 and cultured by using growth and differentiation media (**Figure 3.3b**).[35] The formation of high-quality biotic/abiotic interface enables the

hybrid to electrically/optically stimulate and effectively monitor the electrophysiological characteristics *in vitro* and *in vivo*.

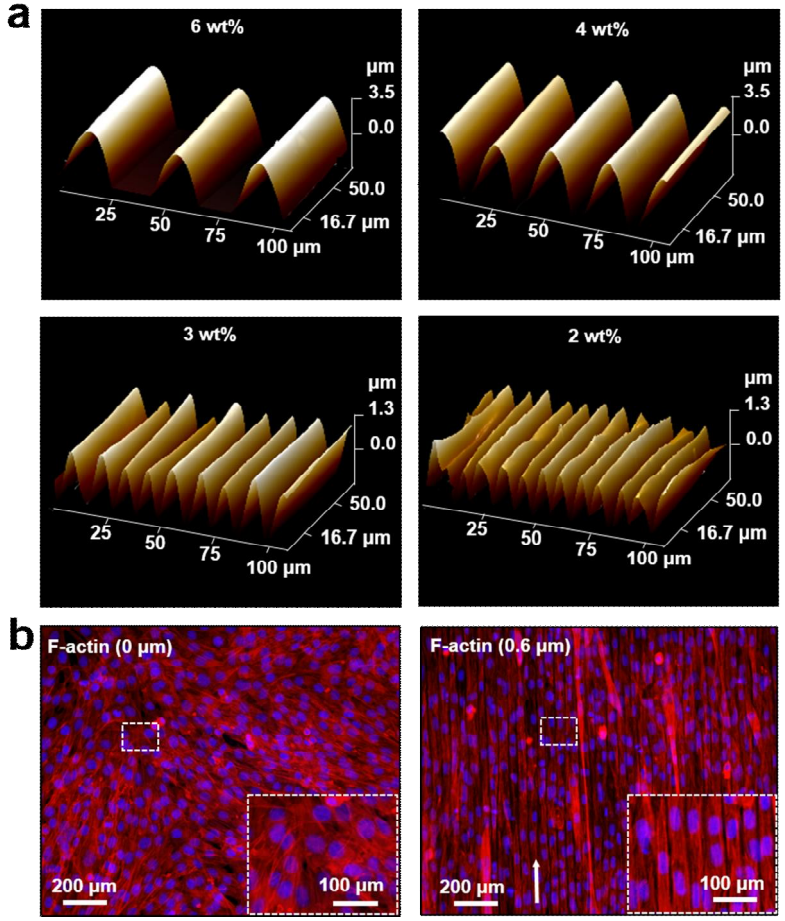

Figure 3.3 Control of wavelengths for guiding cell alignments

(a) AFM images of buckled structure of the hybrid device. The wavelengths of devices are changed by the PI film thickness. (b) Fluorescence microscopic image of aligned C2C12 myoblasts on the buckled mesh-patterned graphene electrode. The bottom right inset shows a magnified view of the white box.

3.2.2 Mechanical property of the cell-sheet-graphene hybrid

By simply controlling the overall thickness between 0.3 μm and 1.4 μm, uniform buckled structures of different wavelengths can be formed. The wavelength and amplitude decrease linearly as the PI/graphene thickness is reduced (**Table 3.1**).[40] To determine the optimized wavelength for cell alignment, we cultured C2C12 myoblasts for 3 days on the buckled graphene mesh of different wavelengths. C2C12 myoblasts cultured on the buckled graphene with a 41 μm wavelength show the best alignment (~98%) as shown in **Table 3.1**. The alignment ratio is determined by the method used in the previous study.[35] The preferred adhesion of proteins and thereby cells to the graphene surface enhances efficiency of the cell culture.[35,41]

The factor that quantifies the softness of bioelectronics is the stretchability. Stretchable devices show superb deformability in bending, twisting, and stretching.[36-44] Minimum electrical hysteresis under deformation is another important advantage of stretchable devices.[16,45] Although both graphene[46] and cells[47,48] are intrinsically soft and stretchy, their stretchabilities may be somewhat limited. The graphene electrodes in the form of a flat sheet, buckled sheet, and buckled mesh are tested under stretching (**Figure 3.4a,b**), compressing (**Figure 3.4c,d**), and bending (**Figure 3.4e,f**) conditions. These deformations mimic the various states of

Table 3.1 Optimization of various factors in buckled structure

	Polyimide/NMP content (wt%)					
	12	**8**	**6**	**4**	**3**	**2**
Thickness (μm)	1.41±0.02	1.09±0.01	0.58±0.01	0.4±0.02	0.34±0.03	0.29±0.02
Wavelength (μm)	187.46±12.55	69.10±5.78	41.12±1.08	25.41±1.82	12.79±1.35	8.82±0.64
Amplitude (μm)	12.18±2.13	11.20±2.33	8.24±2.30	5.15±0.99	2.44±0.31	1.28±0.22
Cell alignment ratio (%)	17.42±1.51	71.44±2.48	98.85±3.91	95.31±3.55	87.44±2.84	73.85±4.51

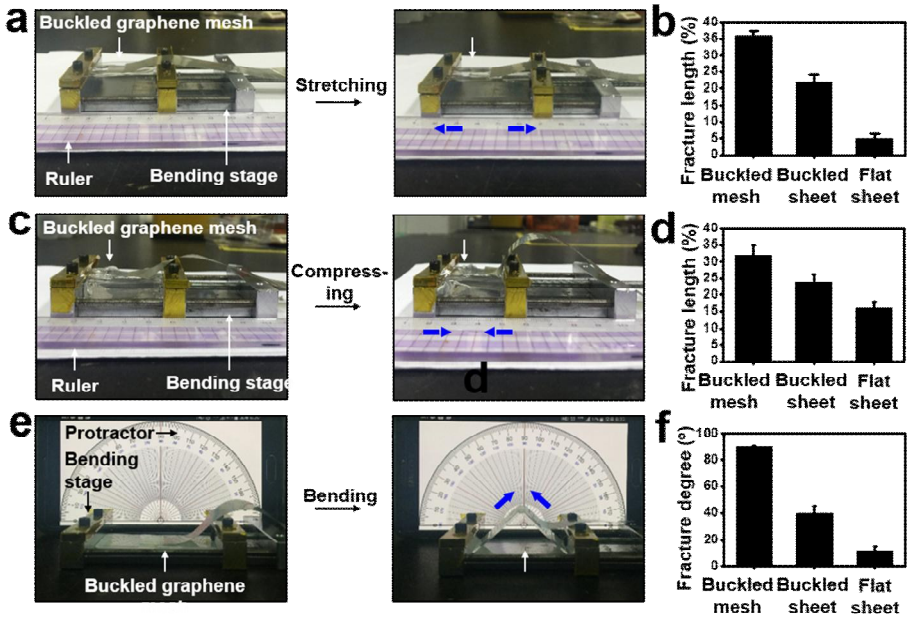

Figure 3.4 Characterization of mechanical properties under applying external strains

(a) Images of experiment setups for stretching test. (b) A plot of fracture lengths of three different samples during stretching conditions. (c) Images of experiment setups for compressing test. (d) A plot of fracture lengths of three different samples during compressing conditions. (e) Images of experiment setups for bending test. (f) A plot of fracture degrees of three different samples during bending conditions.

muscular movements (bending, stretching, and compressing). The results in **Figure 3.4** support that the buckled graphene mesh is mechanically sustainable under the typical deformation range[49] of muscular movements (25% contraction; 20% stretching). Moreover, the system modulus of the hybrid (61 kPa) is comparable with the elastic modulus of muscle tissue (52 kPa; **Figure 3.5**). Overall, the buckled mesh-patterned electrode shows the best electrical reliability and mechanical stretchability. Details of the mechanics including the induced strain distributions under deformation are analyzed through finite element modeling,[6,50] the results of which support the experimental results (**Figure 3.6**). The resistance of the graphene mesh begins to increase at the maximum principal strain of 6.17% in modeling (35% stretching) and the graphene mesh is completely fractured at the strain of 11.8% in modeling (40% stretching).

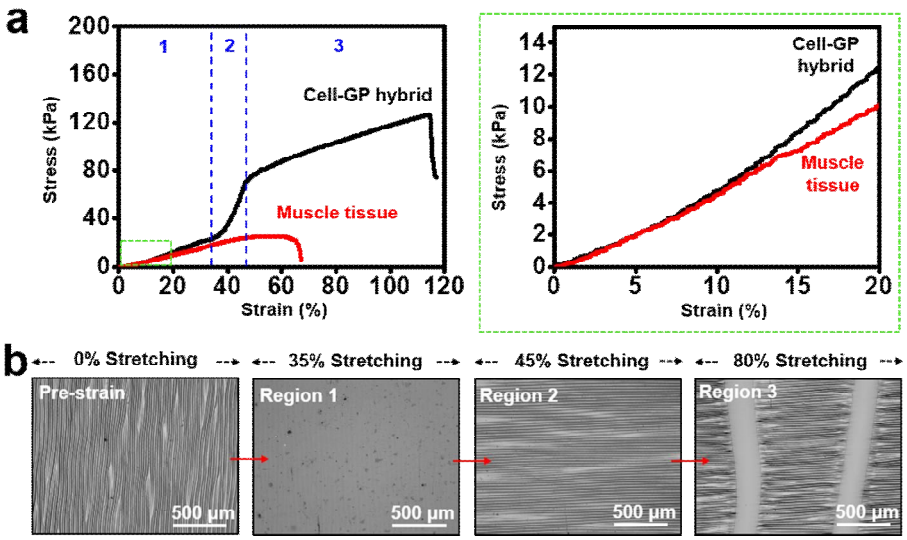

Figure 3.5 System modulus of the hybrid device

(a) Plot of stress-strain curve of cell-sheet-graphene hybrid (Cell-GP hybrid; black) and muscle tissue (red). The hybrid contains 3 distinct regions in the system modulus curve: i) elastic stretching of the hybrid due to buckled topology (~35% of strain), ii) the endurance of polyimide membrane which supports cell sheet and mesh-patterned graphene electrodes (~45% of strain), and iii) the elastic stretching of PDMS after complete fracture of polyimide membrane (~115% of strain). The green-dotted box shows the plot of initial strain region (~20%). (b) Microscopic images of Cell-GP hybrid at each regions in the system modulus curve.

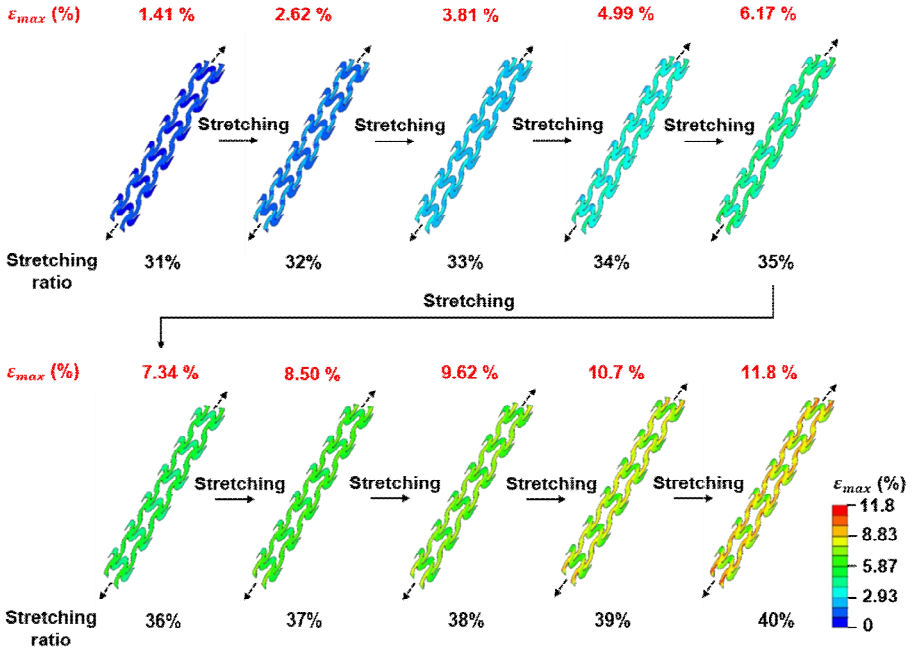

Figure 3.6 Maximum principal strain distribution computed by FEM simulation for the buckled graphene mesh after applying external strain.

3.2.3 Electrochemical characterization of the hybrid device

Au particles are deposited on graphene electrodes by reducing Au ions, which improves electrode's electrochemical properties. Similar electrochemical properties including charge transfer characteristics between doped graphene electrode and gold electrode was shown in previous study.[51] The cell membrane of the cell sheet cultured on the Au-doped graphene electrode, however, may reduce the electrochemical properties. **Figure 3.7a,b** show the impedance change and phase response under frequency range between 1 Hz and 1 MHz. **Figure 3.7c,d** also show the conductance change and charge storage capacity, respectively. The results can support that the cell sheet on the hybrid device can form the conducting tubular structures, in which the electrochemical properties of the hybrid devices is minimally decreased during application *in vitro* and *in vivo*. The impedance of materials and the measurement setups bring an effect on the thermal noise, which is an important factor for the signal-to-noise ratio.[52] The electrode-tissue interface noise, however, is also critical in the measurement of EMG signal particularly in the low frequency range (0.5 Hz to 500 Hz)[52] and high amplification condition (> 100 times). In **Figure 3.7d**, the hybrid device shows larger capacitance than others. This large capacitance minimizes the electrode-tissue interface noise,[53] leading to higher signal-to-noise ratio

(**Figure 3.8**), although this effect cannot be seen in low amplification condition (< 10 times) due to large thermal and equipment noises. These results also agree with a previous report.[18]

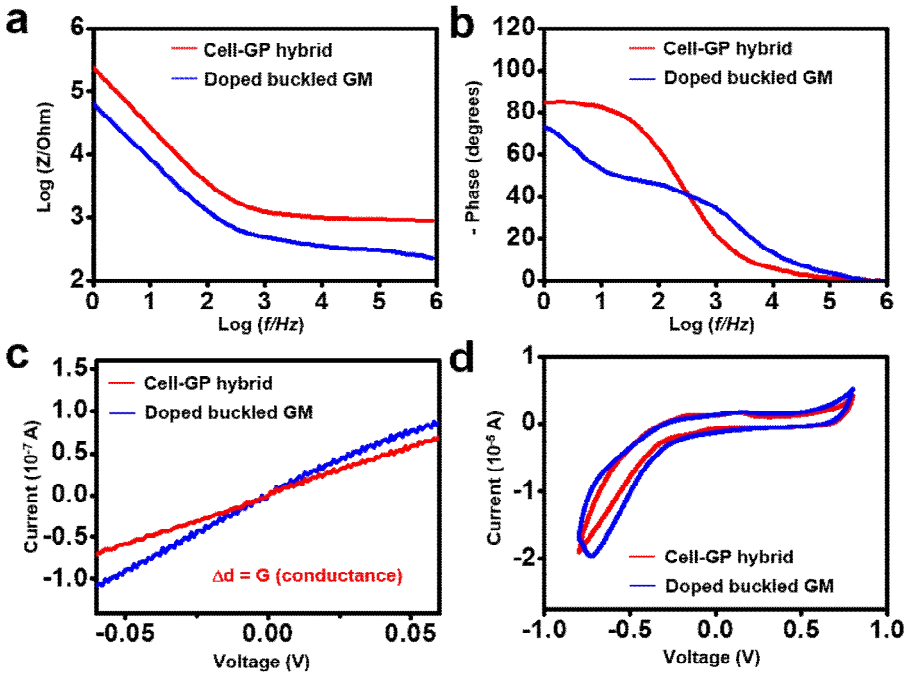

Figure 3.7 Electrochemical characterization of cell-sheet-graphene hybrid

(a,b) Measurements of electrochemical impedance spectroscopy with impedance (a) and phase (b) plots. (c,d) Measurements of conductance and charge storage capacity by plotting of I-V curves (c) and cyclic voltammograms (d). Efficiencies of Cell-GP hybrid in respect to impedance, conductance, and charge storage capacity are 81.9%, 65.6%, and 88.3% of the case without the cell layer (Doped buckled GM), respectively.

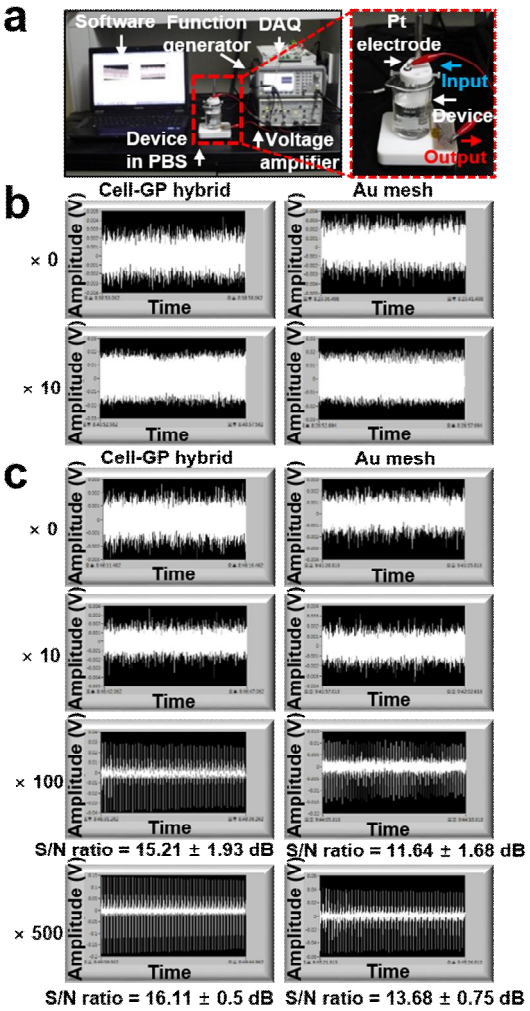

Figure 3.8 Measurement of signal and noise level

(a) Image of experimental setups. The cell-sheet-graphene hybrid (Cell-GP hybrid) and Au mesh electrode are immersed in the PBS solution and connected to the voltage amplifier, DAQ, and computer. Then, the signal and noise levels are recorded with and without applying a 2 mV/10 Hz signal

from the function generator through a separately located Pt electrode. (b) Noise level measured with 0 and 10 times amplification while applying no external signal. (c) Signal and noise levels measured with amplification (0, 10, 100, and 500 times) while applying a 2 mV/10 Hz signal.

3.2.4 Controlled culture and monitoring of cells *in vitro*

Figure 3.9a shows a schematic illustration for the controlled culture of C2C12 myoblasts using electrical stimulation *via* graphene electrodes *in vitro*. Two different monophasic square wave pulses (high 1 V, 1 Hz; low 0.05 V, 1 Hz) are applied to the direction of myotube elongation (red box in Figure 5a) for 3 days as shown in the timetable of **Figure 3.9b**. Elongated and high density culture of myotubes is observed under electrical stimulation using buckled graphene electrodes (10 days culture and 3 days electrical stimulation; **Figure 3.9b**), whereas diminished myotube formation is found in the unstimulated culture (**Figure 3.9c**). The myotubes are detected and imaged by immunostaining of myosin heavy chains. Although the average area per a myotube increases in all groups (0 V, low, and high) from 7 days to 10 days of culture, the increases for electrically stimulated groups are significantly greater than those in the control group (0 V; **Figure 3.9d**). Myotube length changes show similar trends (**Figure 3.9e**).

Cell proliferation and differentiation change the electrochemical environment of cultured cells.[35,36] These changes can be monitored through impedance measurements by using integrated graphene electrodes. Two mesh-patterned graphene electrodes spaced ~300 μm apart serve as an impedance sensor, which continuously monitor impedance changes during

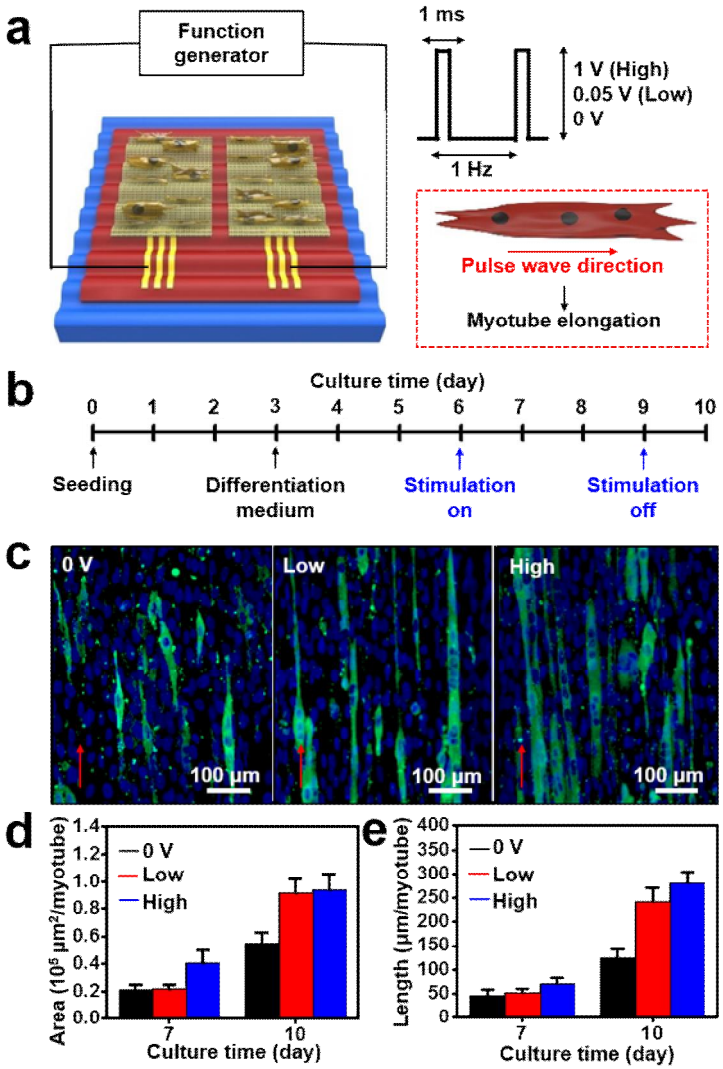

Figure 3.9 Electrical stimulation of C2C12 myoblasts using a buckled mesh-patterend graphene electrode *in vitro*

(a) Schematic illustration of buckled mesh-patterned graphene electrode-mediated electrical stimulation to accelerate the differentiation of C2C12 myoblasts. Monophasic square wave pulses are applied with 3 different

voltages, including 1 V (High), 0.05 V (Low), and 0 V. The red box at the lower right shows that the pulse wave is stimulated in the direction of myotube elongation. (b) Timetable of cell culture. (c) Fluorescence microscopy images of aligned and elongated C2C12 myotubes upon application of three different pulses. The red arrows indicate the direction of the pulse waves. (d,e) Plots of myotube areas (d) and lengths (e) at day 7 (1 day after stimulation begins) and day 10 (1 day after stimulation is removed) differentiation time points.

proliferation and differentiation of skeletal muscle cells controlled by electrical stimulation, as shown in the schematic description in **Figure 3.10a**. The impedance during cell proliferation increases since the electrodes are covered with proliferated cells that act as a high resistance barrier to the conductive medium, whereas the impedance during differentiation decreases because of the formation of conducting myotubes (**Figure 3.10b**). **Figure 3.10c** shows the time-dependent impedance changes (at 0.82 kHz) of myotubes and human dermal fibroblasts (control; hDFBs) during both proliferation and differentiation. The impedance of fibroblasts, however, continuously increases because they do not form conducting tubular structures during differentiation. The effect of electrical stimulation on the differentiation of C2C12 myoblasts is also monitored by the impedance sensor at 0.82 kHz (**Figure 3.10d**). Under high stimulation, faster and greater impedance decreases are observed than other conditions owing to enhanced differentiation and subsequent myotube formation.

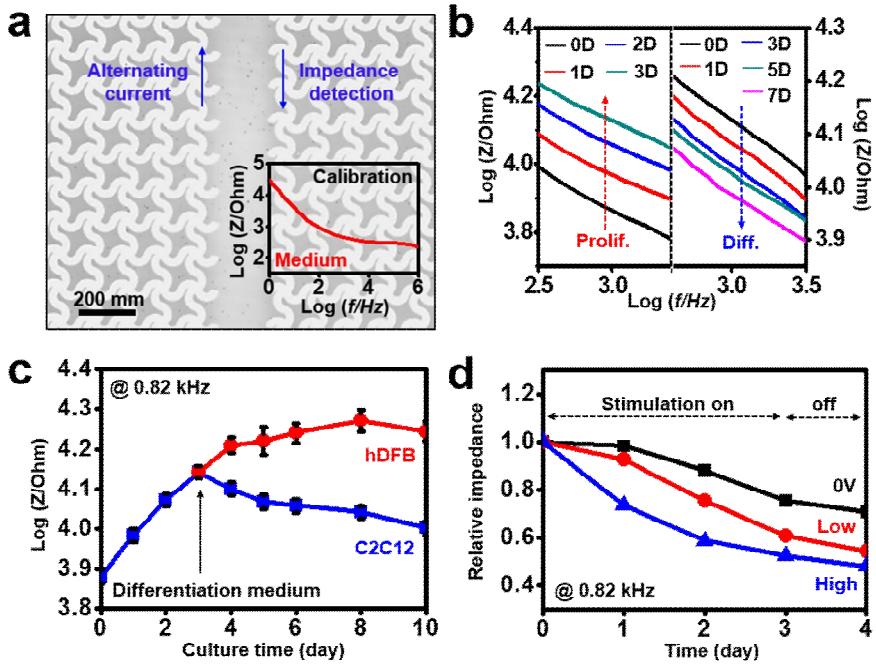

Figure 3.10 Physiological monitoring of C2C12 myoblasts *in vitro*

(a) Optical microscopic image of graphene meshes (background image) and their impedance sensing mechanism. The bottom right inset shows the impedance curve under growth medium measured from 1 Hz to 1 MHz with a bias voltage of 0.01 V. (b) Impedance curve of C2C12 myoblasts according to the proliferation (Prolif.) and the differentiation (Diff.) procedures. (c) The impedance curve of C2C12 myoblasts measured at 0.82 kHz during culture, in comparison with that of human dermal fibroblasts (hDFB). (d) The impedance values measured at 0.82 kHz as the electrical stimulation is applied (three different pulse waves: 0 V, Low (0.05 V), and High (1 V)).

3.2.5 Recording of electrophysiology *in vivo*

Contraction and release of normal skeletal muscle tissues are controlled by depolarization and repolarization of the muscle electrical potential, *i.e.*, EMG changes, which are elicited by action potential signals from the central nervous system. Body movements in daily life are accompanied by muscle contraction/release and changes of EMG. The accurate and continuous recording of EMG through stable and reliable bio-interfaces, therefore, is of high importance in electro-diagnosis of many motion-related neuromuscular diseases. Furthermore, electrical muscle stimulation is a promising procedure to enhance and recover the strength and function of diseased/wounded skeletal muscles.[54] For the electrical muscle stimulation therapy, programed impulses mimicking normal action potential patterns are highly effective.[54] The soft bio-interface formed by the cell-sheet-graphene hybrid system is an appropriate tool for this diagnosis and therapy procedure.

To evaluate the function of the hybrid device *in vivo*, we implanted it onto the hind limb skeletal muscle region of a nude mouse and evaluated effectiveness of its electrical stimulation and EMG sensing function. The electrical stability of the cell-sheet-graphene hybrid under electrically active states (recording and stimulation) is well maintained without degradations of

the electrode and the cell sheet as shown in **Figure 3.11**. Soft nature of the cell-sheet-graphene hybrid forms a high-quality bio-interface. The schematic illustration of experimental setups to test the effectiveness of the EMG monitoring on hind limb skeletal muscles is shown in **Figure 3.12a**. Meanwhile, consideration of extrinsic (*e.g.,* power line noise and cable motion artifact) and intrinsic (*e.g.,* thermal noise and electrode-tissue interface noise) noises during the EMG measurement is important.[55] Improvement of the electrochemical properties (low impedance and high capacitance) of the electrode can reduce the electrode-tissue interface noises.[18,53,55] As shown in **Figure 3.12b**, the cell-sheet-graphene hybrid electrode successfully monitor the EMG signals with high signal-to-noise ratio under same condition of the EMG measurement, particularly in high amplification conditions (**Figure 3.8**). These high efficiencies are achieved with formation of the conducting myotube in the myoblast cell sheet (**Figure 3.7**). The same cell-sheet-graphene hybrid system can be applied for EMG measurements on skin. Because of the conformal integration of the soft cell-sheet-graphene hybrid device with the human epidermis, human EMG signals are successfully measured (**Figure 3.13**).[56]

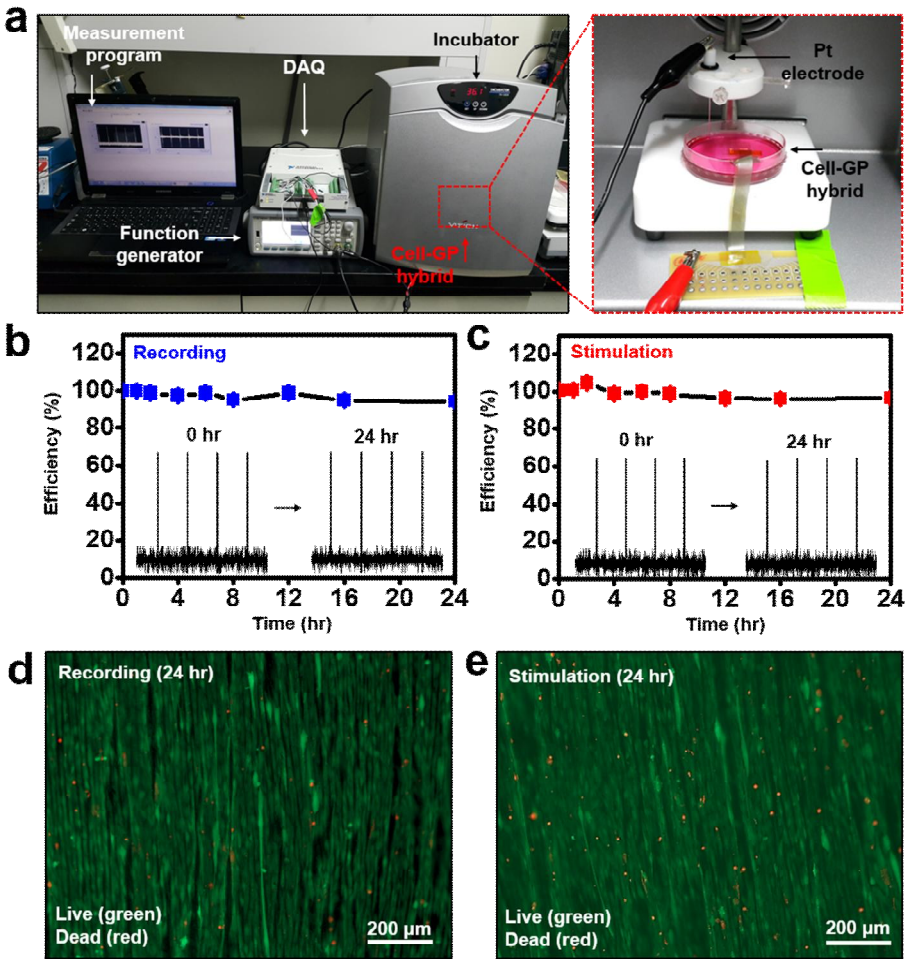

Figure 3.11 Investigation of cell-sheet-graphene hybrid stability under electrical stimulation and recording condition *in vitro*

(a) Image of experimental setups. Each electrode (Cell-GP hybrid or Pt electrode) is connected to either function generator (1 V, 1 Hz) or DAQ accordingly depends on either recording or electrical stimulation experiments. (b,c) Plots of recording (b) and electrical stimulation (c)

efficiencies for the Cell-GP hybrid to investigate its electrical stability within growth medium. (d,e) Fluorescence images of LIVE/DEAD assay for the cell sheet during recording (d) and electrical stimulation (e).

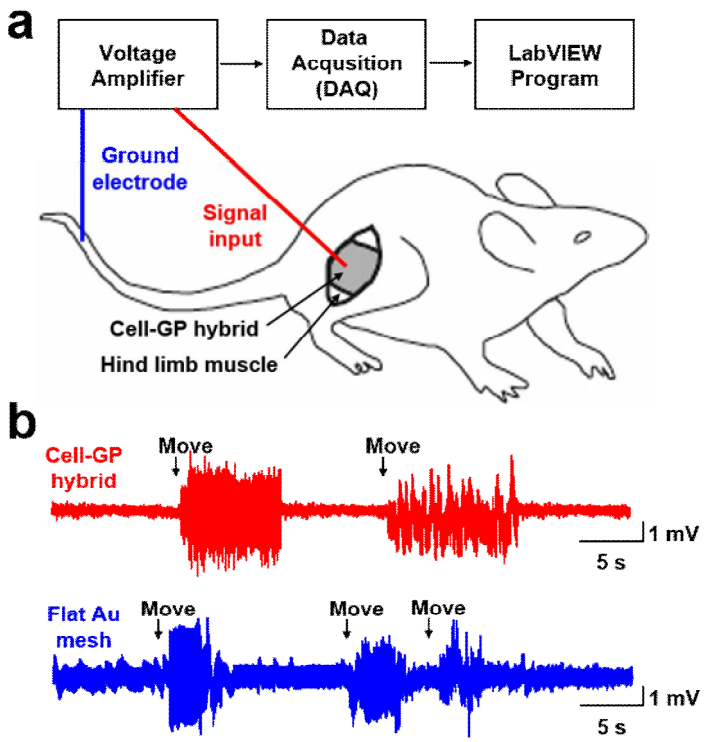

Figure 3.12 EMG monitoring *in vivo* using cell-sheet-graphene hybrid

(a) Schematic illustration of *in vivo* EMG monitoring experiment. (b) Measurement of the EMG signals by the cell-sheet-graphene hybrid (Cell-GP hybrid; red) and flat mesh-patterned Au electrode (Flat Au mesh; blue) during muscle contractions of the murine leg.

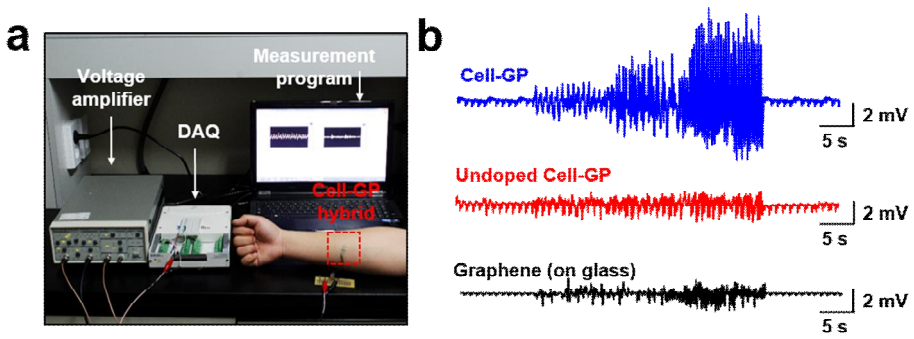

Figure 3.13 Characterization of EMG sensor placed on human skin

(a) Image of experimental setups for EMG sensing on human skin. The hybrid connected with voltage amplifier and DAQ is placed on human skin and its EMG signal is recorded on the program. (b) A plot of EMG signals read on human skin during small, medium, and large muscle contractions *via* cell-sheet-graphene hybrid (Cell-GP), Au-undoped and cell-sheet-graphene hybrid (Undoped Cell-GP), and graphene mesh on glass substrate (Graphene).

3.2.6 Optical stimulation and electrophysiological recording

Optogenetics is an emerging stimulation technique that uses light instead of electrical impulses to excite genetically modified neurons that express light-sensitive proteins such as channelrhodopsin.[17,21,22,57] The optical stimulation of secondary motor cortex and/or peripheral motor neurons, which targets skeletal muscle improvement, provides enhanced therapeutic effects with low fatigue as compared to existing electrical stimulation methods.[21,57] Recording electrophysiological signals from optically stimulated target tissues is another important requirement. Conventional opaque metal electrodes, however, do not allow light to pass through them. Therefore, the intrinsic spatial mismatch between the stimulated tissue positioned immediately below the light source and the electrode position, typically located near the light source, devalues optogenetic approaches. Transparent and conforming electrodes including graphene electrodes have been recently highlighted as providing the spatial overlap of stimulation and recording positions.[18,58] The transparent cell-sheet-graphene hybrid described herein allows high-quality bio-interfacing for real-time recordings as well as spatially synchronized optical stimulations.

To investigate the capabilities of the cell-sheet-graphene hybrid in

optical stimulation and simultaneous recording, it is implanted onto the hind limb muscle region of a ChR2-expressing transgenic mouse (*Thy1-ChR2*)[21] and a blue LED of 470 nm wavelength is placed on top (**Figure 3.14a,b**). The LED is controlled by a function generator to apply optical impulses whose frequency and intensity varied between 5 Hz and 80 Hz and between 8 mW/m^2 and 464 mW/m^2, respectively. The light intensity before and after passing through the device is shown in **Figure 3.14c**, which is high enough to stimulate deep muscles.[59] Optical stimulation-induced muscle activation and EMG signals are recorded simultaneously (40 Hz, 464 mW/m^2 fixed; **Figure 3.14d**). Twitching motions of the transgenic mouse leg are observed during optical stimulations. Optimized conditions of the light impulses for maximum excitation of peripheral motor neurons are experimentally determined through recording EMG signals under different light frequencies and intensities.[21,59] **Figure 3.15** shows the filtered EMG signals to present their amplitudes[60] under different frequencies (464 mW/m^2 is fixed) of light impulses applied to hind limb muscles. We found that 40 Hz optical stimulation shows the highest amplitude of EMG. The plateau potential increases as the frequency of optical stimulation increases.[59] The amplitude of EMG signal at the frequency of 80 Hz, however, is decreased because the depolarization continues from the delay of repolarization.[59] **Figure 3.16**

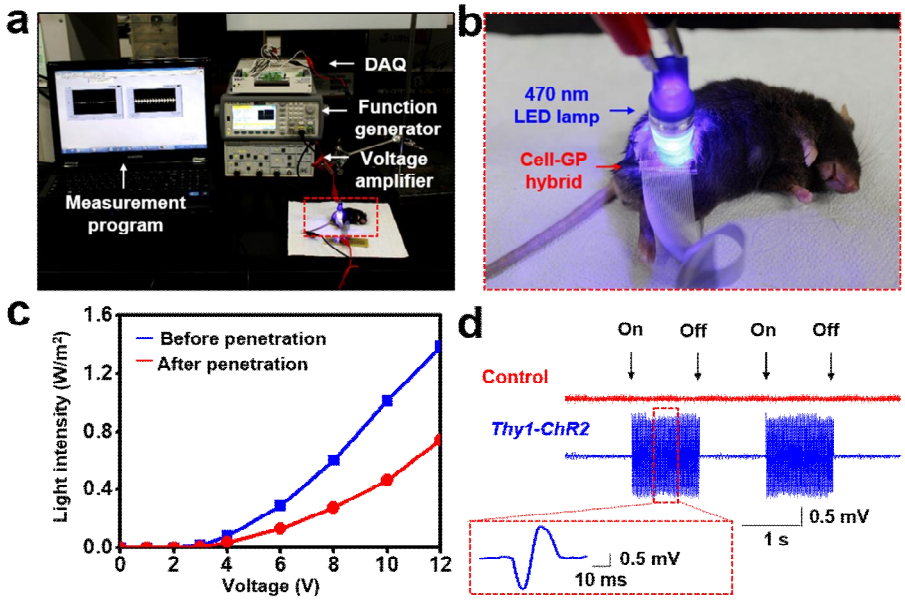

Figure 3.14 Optogenetic application of cell-sheet-graphene hybrid *in vivo*

(a) Images of experimental setups for the optogenetic application. (b) EMG sensing, *via* the cell-sheet-graphene hybrid, of the hind limb muscle of channelrhodopsin 2-expressing transgenic mouse (*Thy1-ChR2*) stimulated by 470 nm blue LED placed on top of the hybrid. (c) Light intensities of 470 nm LED lamp. (d) Raw EMG signals during LED on/off states. The blue and red curves represent the EMG signals from the transgenic and wild type mice, respectively. The red box shows a single unit of EMG signal.

shows the filtered EMG signals of different light intensities (40 Hz is fixed) ranging from 8 mW/m^2 to 464mW/m^2. The light intensity of 464 mW/m^2 shows the highest amplitude of EMG; the amplitude of EMG decreases as the light intensity decreases.[21,59]

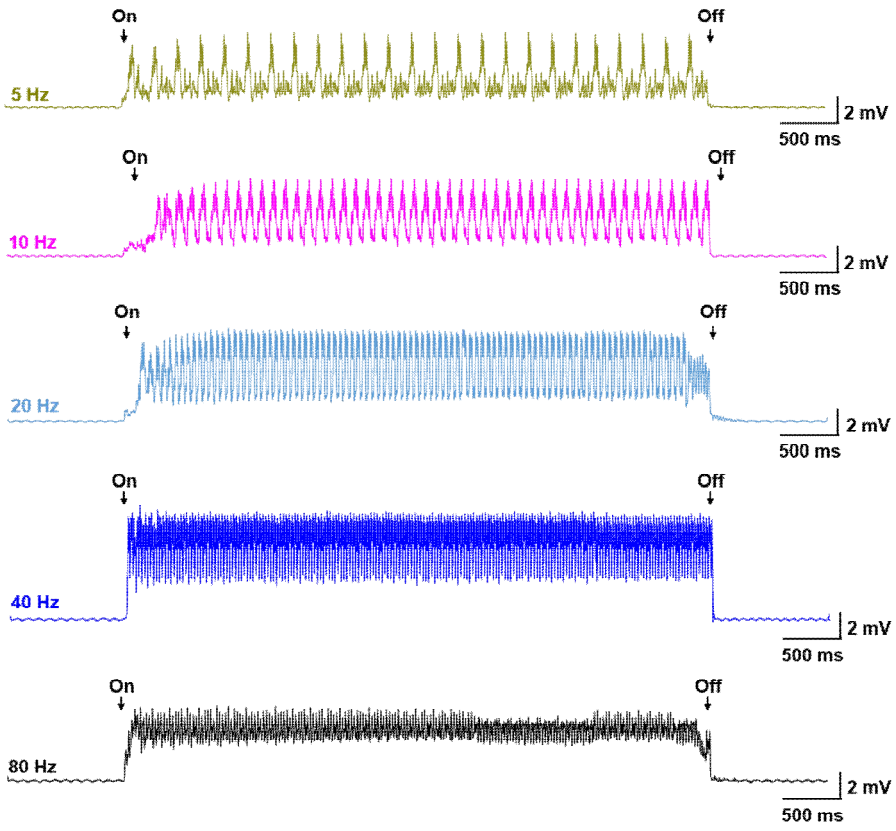

Figure 3.15 Filtered EMG data of cell-sheet-graphene hybrid at various frequencies of optical stimulation. Light intensity is fixed at 464 mW/m^2.

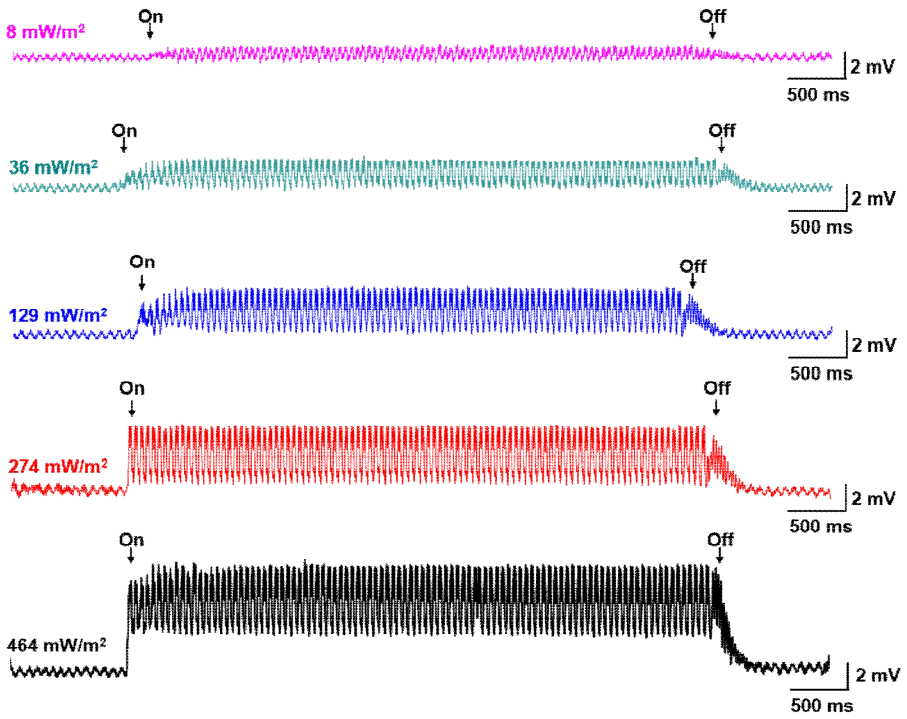

Figure 3.16 Filtered EMG data of cell-sheet-graphene hybrid at various light intensities of optical stimulation. Light frequency is fixed at 40 Hz.

3.2.7 Cell sheet therapy of the hybrid device

The cell sheet in the cell-sheet-graphene hybrid not only enhances the conformal bio-interface but also provides inherent therapeutic effects. We implanted the cell-sheet-graphene hybrid incorporating confluent and well-differentiated C2C12 myoblasts onto the hind limb skeletal muscles of nude mice. **Figure 3.17a** shows the growth of the C2C12 myoblasts at the implanted site. Microscope images of hematoxylin and eosin staining are obtained from sectioned tissue slices. While a single layer of C2C12 myoblasts is detected 1 day after implantation, several layers on the native muscle are observed 7 days after implantation, which confirms the efficient proliferation of transplanted myoblasts from the cell-sheet-graphene hybrid. New vessel formation, *i.e.*, angiogenesis, is essential in this regeneration particularly for nutrition supply and gas exchange. **Figure 3.17b** shows the enhancement of local angiogenesis 7 days after implantation. CD31 staining of angiogenic vessels indicates the growth of the C2C12 myoblasts in/near the implanted sites. The quantified data of the thickness of cell growth and the number of angiogenic vessels from the microscope images are plotted in **Figure 3.17c**, which corroborates the therapeutic effect of the cell-sheet-graphene hybrid. The localization of highly differentiated C2C12 myoblasts in the implanted cell-sheet-graphene hybrid enhances vascularization,

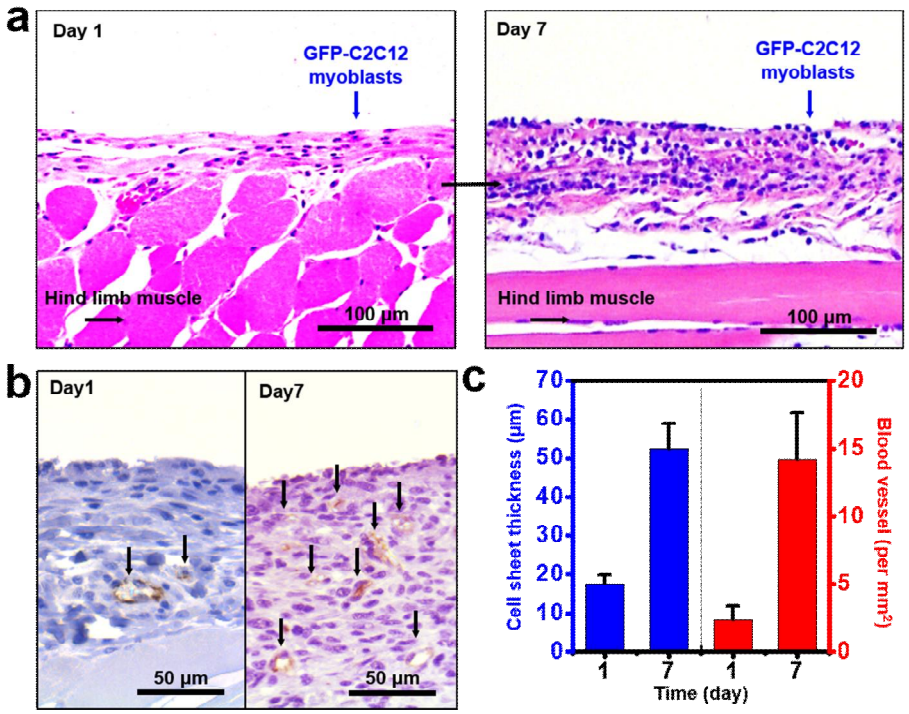

Figure 3.17 Investigation of the therapeutic effect of C2C12 myoblasts sheet on the hybrid device

(a) Hematoxylin and eosin staining of the operated hind limb at 1 day (left) and 7 days (right) after implantations for morphological observation. (b) Formation of new vessels (black arrows) in the region of implantation at 1 day (left) and 7 days (right) after implantation. (c) Plots of cell sheet thickness and the number of angiogenic vessels in the operated hind limb during 1 day and 7 days after implantation.

regeneration of skeletal muscles, and functional recovery.[31,61] Furthermore, the fluorescence images indicate that C2C12 myoblasts on the surface of graphene electrodes suppress the recruitment of CD68-positive macrophages at the implanted site (**Figure 3.18a,b**). Without the cell sheet, the device can cause acute immune responses. Its quantitative data is plotted in **Figure 3.18c**. These results support that the cell-sheet-graphene hybrid is highly effective for both the diagnosis and treatment of skeletal muscle tissue damages.

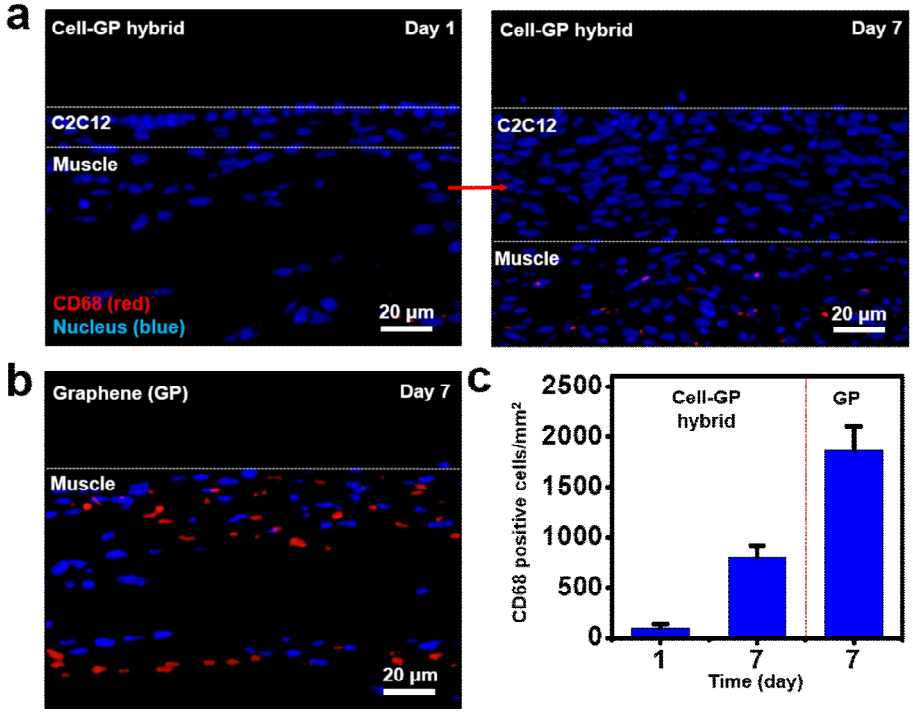

Figure 3.18 Observation of the bio-interface of cell-sheet-grahpene hybrid

(a) Fluorescence images of observing the formation of high-quality bio-interface by immunostaining of operated hind limb muscle using anti-CD68 antibody (red fluorescence; macrophages) and counterstained with DAPI (blue fluorescence; nuclei). (b) A plot of CD68 positive cells from fluorescence images.

3.3 Conclusion

The stretchable and transparent bio-interface using a cell-sheet-graphene hybrid offers a new strategy for multifunctional implantable devices. It features high-quality electrophysiological sensing, electrical and/or optical stimulation treatment, and regeneration therapy by hybridized cells. The integrated system is biocompatible and highly effective as a soft implantable device for skeletal muscle tissue. The buckled graphene mesh aligns the cultured cells and enhances their proliferation and differentiation as well as provides mechanical stretchability to the system. Furthermore, it acts as an electrical stimulator and an impedance sensor for the controlled culture of C2C12 myoblasts and their continuous monitoring *in vitro*. The well fabricated, transparent, and stretchable cell-sheet-graphene hybrid is implanted on the hind limb muscle of mouse for electromyographic monitoring and the treatment of normal and transgenic muscles with electrical and optical stimulation *in vivo*. The cell sheet on the hybrid provides therapeutic function onto implanted tissues as well as forming a high-quality bio-interface without any host immune responses. These advances open a new pathway to the next-generation multifunctional soft bioelectronics.

3.4 Experimental

3.4.1 Electrochemical characteristics

Impedance, conductance and CV were measured by electrochemical workstation (CHI660E, CH Instruments). Measurements of impedance and conductance were conducted with three-electrode configuration (buckled graphene mesh, Ag/AgCl, and Pt electrode), and CV was conducted with two-electrode configuration (buckled graphene mesh and Ag/AgCl electrode) in pH 7.0 PBS solution.

3.4.2 Electrical characteristics of C2C12 myoblasts

For electrical stimulation, monophasic square wave pulses were applied to culturing C2C12 myoblasts *via* the hybrid. The parameters of the pulses, including frequency, duration, and amplitude were controlled by a function generator (33500B, Agilent Technologies). During electrical stimulation, the cells were cultured in an incubator under standard culture conditions. For monitoring the impedance changes, the electrodes of the hybrid were connected and measured using an electrochemical workstation (CHI660E, CH Instruments).

3.4.3 *In vivo* mouse model

The experiments on the animals used for the optogenetics study were approved by the Animal Care Committees at the Korea Institute of Science and Technology. Lab-bred 9–12 week-old *Thy1-ChR2* or C57BL/6 control mice were anesthetized with 2% avertin (tribro-moethyl alcohol/tertiary amyl alcohol), and the hind limb was surgically incised for the implantation. The experiments on the animals used for observations of cellular effects *in vivo* were approved by the Animal Care Committees at Seoul National University Hospital. Six-week-old male BALB/c nude mice were anesthetized with a mixture of zolazepam and xylazine and the hind limb was surgically incised for the implantation.

3.4.4 Electrical and optical characteristics *in vivo*

For electrical stimulation, monophasic square wave pulses were applied to the skeletal muscle and controlled by a function generator. For optical stimulation, the frequency and intensity of a 470 nm LED lamp (1.5W T10 blue LED, Sungetace) on the top of the device was controlled by a function generator. The EMG signal was measured by a data acquisition equipment (DAQ; National Instruments) with the LabVIEW software (encoded with 60 Hz notch filter). A voltage amplifier (Stanford Research

Systems) is additionally used for filtering (10 Hz of high-pass filter and 300 Hz of low-pass filter) and amplifying (×500 of gain) the signals. The EMG signal was processed using MATLAB software (MathWorks). To obtain the root-mean-square signal, the data are treated with filtering (cut off the data at 100 Hz), rectifying (cut off the negative part), smoothing, and root-mean-square processing, sequentially.

3.4.5 Histology

For sample preparation, all tissues were fixed in paraffin and sectioned to 4 mm thickness. The dewaxing, hydrating and treating with protease XXIV is preliminary conducted to visualize myoblasts. Anti-GFP antibodies (Santa Cruz Biotechnology) and Alexa Fluor 488-conjugated secondary antibodies (Invitrogen) were used to visualize protein expression. Images were obtained by an inverted fluorescence microscope. Histology samples for morphology visualization were stained by hematoxylin and eosin using standard protocols, and vascularization detection was performed using immunohistochemistry with anti-CD31 antibodies (Novus Biologicals) followed by staining with a 3,3′-diaminobenzidine (Dako) peroxidase substrate. Macrophages were also immunohistochemically stained with anti-CD68 antibodies (Novus Biologicals) and Alexa Fluor 647-conjugated

secondary antibodies (Invitrogen). The histologic samples were observed using an optical and fluorescence microscope.

3.5 References

1. Khodagholy, D., Doublet, T., Quilichini, P., Gurfinkel, M., Leleux, P., Ghestem, A., Ismailova, E., Hervé, T., Sanaur, S., Bernard, C. & Malliaras, G, G. In vivo recordings of brain activity using organic transistors. *Nat. Commun.* **4**, 1575 (2013).
2. Emeryk-Szajewska, B. & Kopeć, J. Electromyographic pattern in Duchenne and Becker muscular dystrophy. Part I: Electromyographic pattern in subsequent stages of muscle lesion in Duchenne muscular dystrophy. *Electromyogr. Clin. Neurophysiol.* **48**, 265-277 (2008).
3. Hausmanowa-Petrusewicz, I. & Karwańska, A. Electromyographic findings in different forms of infantile and juvenile proximal spinal muscular atrophy. *Muscle Nerve* **9**, 37-46 (1986).
4. Rissanen, S., Kankaanpää, M., Tarvainen, M, P., Nuutinen, J., Tarkka, I, M., Airaksinen, O. & Karjalainen, P, A. Analysis of surface EMG signal morphology in Parkinson's disease. *Physiol. Meas.* **28**, 1507-1521 (2007).
5. Minev, I, R., Musienko, P., Hirsch, A., Barraud, Q., Wenger, N., Moraud, E, M., Gandar, J., Capogrosso, M., Milekovic, T., Asboth, L., Torres, R, F., Vachicouras, N., Liu, Q., Pavlova, N., Duis, S., Larmagnac, A., Vörös, J., Micera, S., Suo, Z., Courtine, G. & Lacour, S, P. Biomaterials. Electronic dura mater for long-term multimodal neural interfaces. Science 347, 159-

163 (2015).

6. Lim, S., Son, D., Kim, J., Lee, Y, B., Song, J., Choi, S., Lee, D, J., Kim, J, H., Lee, M., Hyeon, T. & Kim, D, H., Transparent and stretchable interactive human machine interface based on patterned graphene heterostructures. *Adv. Funct. Mater.* **25**, 375-383 (2015).
7. Son, D., Lee, J., Qiao, S., Ghaffari, R., Kim, J., Lee, J, E., Song, C., Kim, S, J., Lee, D, J., Jun, S, W., Yang, S., Park, M., Shin, J., Do, K., Lee, M., Kang, K., Hwang, C, S., Lu, N., Hyeon, T. & Kim, D, H. Multifunctional wearable devices for diagnosis and therapy of movement disorders. *Nat. Nanotechnol.* **9**, 397-404 (2014).
8. Choi, M, K., Park, O, K., Choi, C., Qiao, S., Ghaffari, R., Kim, J., Lee, D, J., Kim, M., Hyun, W., Kim, S, J., Hwang, H, J., Kwon, S, H., Hyeon, T., Lu, N. & Kim, D, H. Cephalopod-inspired miniaturized suction cups for smart medical skin. *Adv. Healthc. Mater.* **5**, 80-87 (2016).
9. Choi, M, K., Park, I., Kim, D, C., Joh, E., Park, O, K., Kim, J., Kim, M., Choi, C., Yang, J., Cho, K, W., Hwang, J, H., Nam, J, M., Hyeon, T., Kim, J, H. & Kim, D, H. Thermally controlled, patterned graphene transfer printing for transparent and wearable electronic/optoelectronic system. *Adv. Funct. Mater.* **25**, 7109-7118 (2015).
10. Normann, R., McDonnall, D. & Clark, G. Control of skeletal muscle

force with currents injected via an intrafascicular, microelectrode array. *Conf. Proc. IEEE Eng. Med. Biol. Soc.* **7**, 7644-7647 (2005).

11. Xu, L., Gutbrod, S, R., Bonifas, A, P., Su, Y., Sulkin, M, S., Lu, N., Chung, H, J., Jang, K, I., Liu, Z., Ying, M., Lu, C., Webb, R, C., Kim, J, S., Laughner, J, I., Cheng, H., Liu, Y., Ameen, A., Jeong, J, W., Kim, G, T., Huang, Y., Efimov, I, R. & Rogers, J, A. 3D multifunctional integumentary membranes for spatiotemporal cardiac measurements and stimulation across the entire epicardium. *Nat. Commun.* **5**, 3329 (2014).
12. Kim, D,-H., Lu, N., Ma, R., Kim, Y,-S., Kim, R,-H., Wang, S., Wu, J., Won, S, M., Tao, H., Islam, A., Yu, K, J., Kim, T,-i., Chowdhury, R., Ying, M., Xu, L., Li, M., Chung, H,-J., Keum, H., McCormick, M., Liu, P., Zhang, Y,-W., Omenetto, F, G., Huang, Y., Coleman, T. & Rogers, J, A. Epidermal electronics. *Science* **333**, 838-843 (2011).
13. Kim, J., Lee, M., Shim, H, J., Ghaffari, R., Cho, H, R., Son, D., Jung, Y, H., Soh, M., Choi, C., Jung, S., Chu, K., Jeon, D., Lee, S, T., Kim, J, H., Choi, S, H., Hyeon, T. & Kim, D, H. Stretchable silicon nanoribbon electronics for skin prosthesis. *Nat. Commun.* **5**, 5747 (2014).
14. Sekitani, T., Zschieschang, U., Klauk, H. & Someya, T. Flexible organic transistors and circuits with extreme bending stability. *Nat. Mater.* **9**, 1015-1022 (2010).

15. Kuribara, K., Wang, H., Uchiyama, N., Fukuda, K., Yokota, T., Zschieschang, U., Jaye, C., Fischer, D., Klauk, H., Yamamoto, T., Takimiya, K., Ikeda, M., Kuwabara, H., Sekitani, T., Loo, Y, L. & Someya, T. Organic transistors with high thermal stability for medical applications. *Nat. Commun.* **3**, 723 (2012).

16. Choi, S., Park, J., Hyun, W., Kim, J., Kim, J., Lee, Y, B., Song, C., Hwang, H, J., Kim, J, H., Hyeon, T. & Kim, D, H. Stretchable heater using ligand-exchanged silver nanowire nanocomposite for wearable articular thermotherapy. *ACS Nano* **9**, 6626-6633 (2015).

17. Park, D, W., Schendel, A, A., Mikael, S., Brodnick, S, K., Richner, T, J., Ness, J, P., Hayat, M, R., Atry, F., Frye, S, T., Pashaie, R., Thongpang, S., Ma, Z. & Williams, J, C. Graphene-based carbon-layered electrode array technology for neural imaging and optogenetic applications. *Nat. Commun.* **5**, 5258 (2014).

18. Kuzum, D., Takano, H., Shim, E., Reed, J, C., Juul, H., Richardson, A, G., de, Vries, J., Bink, H., Dichter, M, A., Lucas, T, H., Coulter, D, A., Cubukcu, E. & Litt, B. Transparent and flexible low noise graphene electrodes for simultaneous electrophysiology and neuroimaging. *Nat. Commun.* **5**, 5259 (2014).

19. Khodagholy, D., Gelinas, J, N., Thesen, T., Doyle, W., Devinsky, O.,

Malliaras, G, G. & Buzsáki, G. NeuroGrid: recording action potentials from the surface of the brain. *Nat. Neurosci.* **18**, 310-315 (2015).

20. Williamson, A., Ferro, M., Leleux, P., Ismailova, E., Kaszas, A., Doublet, T., Quilichini, P., Rivnay, J., Rózsa, B., Katona, G., Bernard, C. & Malliaras, G, G. Localized neuron stimulation with organic electrochemical transistors on delaminating depth probes. *Adv. Mater.* **27**, 4405-4410 (2015).

21. Llewellyn, M, E., Thompson, K, R., Deisseroth, K. & Delp, S, L. Orderly recruitment of motor units under optical control in vivo. *Nat. Med.* **16**, 1161-1165 (2010).

22. Kim, T, I., McCall, J, G., Jung, Y, H., Huang, X., Siuda, E, R., Li, Y., Song, J., Song, Y, M., Pao, H, A., Kim, R, H., Lu, C., Lee, S, D., Song, I, S., Shin, G., Al-Hasani, R., Kim, S., Tan, M, P., Huang, Y., Omenetto, F, G., Rogers, J, A. & Bruchas, M, R. Injectable, cellular-scale optoelectronics with applications for wireless optogenetics. *Science* **340**, 211-216 (2013).

23. Tee, B, C., Chortos, A., Berndt, A., Nguyen, A, K., Tom, A., McGuire, A., Lin, Z, C., Tien, K., Bae, W, G., Wang, H., Mei, P., Chou, H, H., Cui, B., Deisseroth, K., Ng, T, N. & Bao, Z. A skin-inspired organic digital mechanoreceptor. *Science* **350**, 313-316 (2015).

24. LaVan, D, A., McGuire, T. & Langer, R. Small-scale systems for in vivo

drug delivery. *Nat Biotechnol.* **21**, 1184-1191 (2003).

25. Son, D., Lee, J., Lee, D, J., Ghaffari, R., Yun, S., Kim, S, J., Lee, J, E., Cho, H, R., Yoon, S., Yang, S., Lee, S., Qiao, S., Ling, D., Shin, S., Song, J, K., Kim, J., Kim, T., Lee, H., Kim, J., Soh, M., Lee, N., Hwang, C, S., Nam, S., Lu, N., Hyeon, T., Choi, S, H. & Kim, D, H. Bioresorbable electronic stent integrated with therapeutic nanoparticles for endovascular diseases. *ACS Nano* **9**, 5937-5946 (2015).

26. Couvreur, P. Drug delivery: replenishing reservoirs in vivo. *Nat. Nanotechnol.* **9**, 874-875 (2014).

27. Brudno, Y., Silva, E, A., Kearney, C, J., Lewin, S, A., Miller, A., Martinick, K, D., Aizenberg, M. & Mooney, D, J. Refilling drug delivery depots through the blood. *Proc. Natl. Acad. Sci. U. S. A.* **111**, 12722-12727 (2014).

28. Cosgrove, B, D., Gilbert, P, M., Porpiglia, E., Mourkioti, F., Lee, S, P., Corbel, S, Y., Llewellyn, M, E., Delp, S, L. & Blau, H, M. Rejuvenation of the muscle stem cell population restores strength to injured aged muscles. *Nat. Med.* **20**, 255-264 (2014).

29. Chong, J, J., Yang, X., Don, C, W., Minami, E., Liu, Y, W., Weyers, J, J., Mahoney, W, M., Van, Biber, B., Cook, S, M., Palpant, N, J., Gantz, J, A., Fugate, J, A., Muskheli, V., Gough, G, M., Vogel, K, W., Astley, C, A.,

Hotchkiss, C, E., Baldessari, A., Pabon, L., Reinecke, H., Gill, E, A., Nelson, V., Kiem, H, P., Laflamme, M. A. & Murry, C, E. Human embryonic-stem-cell-derived cardiomyocytes regenerate non-human primate hearts. *Nature* **510**, 273-277 (2014).

30. Pabbruwe, M, B., Esfandiari, E., Kafienah, W., Tarlton, J, F. & Hollander, A, P. Induction of cartilage integration by a chondrocyte/collagen-scaffold implant. *Biomaterials* **30**, 4277-4286 (2009).

31. Kim, D, W., Jun, I., Lee, T, J., Lee, J, H., Lee, Y, J., Jang, H, K., Kang, S., Park, K, D., Cho, S, W., Kim, B, S. & Shin, H. Therapeutic angiogenesis by a myoblast layer harvested by tissue transfer printing from cell-adhesive, thermosensitive hydrogels. *Biomaterials* **34**, 8258-8568 (2013).

32. Liao, J., Qu, Y., Chu, B., Zhang, X. & Qian, Z. Biodegradable CSMA/PECA/graphene porous hybrid scaffold for cartilage tissue engineering. *Sci. Rep.* **5**, 9879 (2015).

33. Seo, J, M., Kim, S, J., Chung, H., Kim, E, T., Yu, H, G. & Yu, Y, S. Biocompatibility of polyimide microelectrode array for retinal stimulation. *Mater. Sci. Eng. C* **24**, 185-189 (2004).

34. Defrère, S., Mestagdt, M., Riva, R., Krier, F., Van, Langendonckt, A., Drion, P., Jérôme, C., Evrard, B., Dehoux, J, P., Foidart, J, M. & Donnez, J. In vivo biocompatibility of three potential intraperitoneal implants.

Macromol. Biosci. **11**, 1336-1345 (2011).

35. Kim, S, J., Cho, H, R., Cho, K, W., Qiao, S., Rhim, J, S., Soh, M., Kim, T., Choi, M, K., Choi, C., Park, I., Hwang, N, S., Hyeon, T., Choi, S, H., Lu, N. & Kim, D, H. Multifunctional cell-culture platform for aligned cell sheet monitoring, transfer printing, and therapy. *ACS Nano* **9**, 2677-2688 (2015).

36. Bagnaninchi, P. O. & Drummond, N. Real-time label-free monitoring of adipose-derived stem cell differentiation with electric cell-substrate impedance sensing. *Proc. Natl. Acad. Sci. U. S. A.* **108**, 6462-6467 (2011).

37. Han, T, H., Lee, Y., Choi, M, R., Woo, S, H., Bae, S, H., Hong, B, H., Ahn, J, H. & Lee, T, W. Extremely efficient flexible organic light-emitting diodes with modified graphene anode. *Nat. Photonics* **6**, 105-110 (2012).

38. Lacour, S, P., Jones, J., Wagner, S., Li, T. & Suo, Z. Stretchable Interconnects for Elastic Electronic Surfaces. *Proc. IEEE* **93**, 1459-1467 (2005).

39. Bae, S., Kim, H., Lee, Y., Xu, X., Park, J. S., Zheng, Y., Balakrishnan, J., Lei, T., Kim, H. R., Song, Y. I., Kim, Y, J., Kim, K, S., Ozyilmaz, B., Ahn, J, H., Hong, B, H. & Iijima, S. Roll-to-roll production of 30-inch graphene films for transparent electrodes. *Nat. Nanotechnol.* **5**, 574-578 (2010).

40. Stafford, C, M., Harrison, C., Beers, K, L., Karim, A., Amis, E, J.,

VanLandingham, M, R., Kim, H, C., Volksen, W., Miller, R, D. & Simonyi, E, E. A buckling-based metrology for measuring the elastic moduli of polymeric thin films. *Nat. Mater.* **3**, 545-550 (2004).

41. Sawyer, A. A., Hennessy, K. M. & Bellis, S. L. Regulation of mesenchymal stem cell attachment and spreading on hydroxyapatite by RGD peptides and adsorbed serum proteins. *Biomaterials* **26**, 1467-1475 (2005).

42. Kim, D, H., Lu, N., Ghaffari, R. & Rogers, J, A. Inorganic semiconductor nanomaterials for flexible and stretchable bio-integrated electronics. *NPG Asia Mater.* **4**, e15 (2012).

43. Lu, N. & Kim, D, H. Flexible and Stretchable Electronics Paving the Way for Soft Robotics. *Soft Robotics* **1**, 53-62 (2013).

44. Son, D., Koo, J, H., Song, J, K., Kim, J., Lee, M., Shim, H, J., Park, M., Lee, M., Kim, J, H. & Kim D, H. Stretchable carbon nanotube charge-trap floating-gate memory and logic devices for wearable electronics. *ACS Nano* **9**, 5585-5593 (2015).

45. Jeong, G, S., Baek, D, H., Jung, H, C., Song, J, H., Moon, J, H., Hong, S, W., Kim, I, Y. & Lee, S, H. Solderable and electroplatable flexible electronic circuit on a porous stretchable elastomer. *Nat. Commun.* **3**, 977 (2012).

46. Lee, C., Wei, X., Kysar, J, W. & Hone, J. Measurement of the elastic properties and intrinsic strength of monolayer graphene. Science 321, 385-388 (2008).

47. Huh, D., Matthews, B. D., Mammoto, A., Montoya-Zavala, M., Hsin, H. Y. & Ingber, D. E. Reconstituting organ-level lung functions on a chip. *Science* **328**, 1662-1668 (2010).

48. Huh, D., Leslie, D. C., Matthews, B. D., Fraser, J. P., Jurek, S., Hamilton, G. A., Thorneloe, K. S., McAlexander, M. A. & Ingber, D. E. A human disease model of drug toxicity-induced pulmonary edema in a lung-on-a-chip microdevice. *Sci. Transl. Med.* **4**, 159ra147 (2012).

49. Rassier, D, E., MacIntosh, B, R. & Herzog, W. Length dependence of active force production in skeletal muscle. *J. Appl. Physiol.* **86**, 1445-1457 (1999).

50. Jung, S., Kim, J, H., Kim, J., Choi, S., Lee, J., Park, I., Hyeon, T. & Kim, D, H. Reverse-micelle-induced porous pressure-sensitive rubber for wearable human-machine interfaces. *Adv. Mater.* **26**, 4825-4830 (2014).

51. McAdams, E, T., Jossinet, J., Subramanian, R. & McCauley, R, G. Characterization of gold electrodes in phosphate buffered saline solution by impedance and noise measurements for biological applications. *Conf. Proc. IEEE Eng. Med. Biol. Soc.* **1**, 4594-4597 (2006).

52. Fernández, M. & Pallás-Areny, R. Ag-AgCl electrode noise in high-resolution ECG measurements. *Biomed. Instrum. Technol.* **34**, 125-130 (2000).

53. Yang, Z., Zhao, Q., Keefer, E. & Liu, W. Noise characterization, modeling, and reduction for in vivo neural recording. *Adv. Neural Inf. Process. Syst.* **22**, 2160-2168 (2009).

54. Gregory, C, M. & Bickel, C, S. Recruitment patterns in human skeletal muscle during electrical stimulation. *Phys. Ther.* **85**, 358-364 (2005).

55. De, Luca, C, J., Gilmore, L, D., Kuznetsov, M. & Roy, S, H. Filtering the surface EMG signal: Movement artifact and baseline noise contamination. *J. Biomech.* **43**, 1573-1579 (2010).

56. Yeo, W, H., Kim, Y, S., Lee, J., Ameen, A., Shi, L., Li, M., Wang, S., Ma, R., Jin, S, H., Kang, Z., Huang, Y. & Rogers, J, A. Multifunctional epidermal electronics printed directly onto the skin. *Adv. Mater.* **25**, 2773-2778 (2013).

57. Zhao, S., Ting, J, T., Atallah, H, E., Qiu, L., Tan, J., Gloss, B., Augustine, G, J., Deisseroth, K., Luo, M., Graybiel, A, M. & Feng, G. Cell type–specific channelrhodopsin-2 transgenic mice for optogenetic dissection of neural circuitry function. *Nat. Methods* **8**, 745-752 (2011).

58. Lee, H., Lee, Y., Song, C., Cho, H, R., Ghaffari, R., Choi, T, K., Kim, K,

H., Lee, Y, B., Ling, D., Lee, H., Yu, S, J., Choi, S, H., Hyeon, T. & Kim, D, H. An endoscope with integrated transparent bioelectronics and theranostic nanoparticles for colon cancer treatment. *Nat. Commun.* **6**, 10059 (2015).

59. Bruegmann, T., van, Bremen, T., Vogt, C, C., Send, T., Fleischmann, B, K. & Sasse, P. Optogenetic control of contractile function in skeletal muscle. *Nat. Commun.* **6**, 7153 (2015).

60. Pincivero, D, M., Green, R, C., Mark, J, D. & Campy, R, M. Gender and muscle differences in EMG amplitude and median frequency, and variability during maximal voluntary contractions of the quadriceps femoris. *J. Electromyogr. Kinesiol.* **10**, 189-196 (2000).

61. Levenberg, S., Rouwkema, J., Macdonald, M., Garfein, E, S., Kohane, D, S., Darland, D, C., Marini, R., van, Blitterswijk, C, A., Mulligan, R, C., D'Amore, P, A. & Langer, R. Engineering vascularized skeletal muscle tissue. *Nat. Biotechnol.* **23**, 879-884 (2005).

Chapter 4. Electronic-Cell-Culture-Platform for Real-Time Monitoring and Stimulation of Cellular Electrophysiology

4.1 Introduction

Cell culture is a fundamental procedure which is frequently used in biological research and in bio-industry including pharmaceutical and cosmetic companies for various purposes such as stem cell therapy[1,2] and toxicity testing.[3,4] With the high demands of mass production in cell culturing,[5] advancement in cell-culture-platforms has been pursued to acquire effective and efficient way to increase the scalability of cell culture. Although continuous and real-time monitoring of physical and chemical culture parameters for the large number of culturing cells at once can be frequently performed for bioengineering researches,[6,7] conventional analysis such as using microscope hinders to improve the mass production in cell culturing due to the requirements of manpower and time consuming. To overcome these limitations, the cell-culture-platforms have been integrated with soft electronics that are based on biocompatible nanomaterials such as organic materials,[8] carbon nanotubes[9] as well as inorganic nanowires[10,11] for

real-time monitoring and stimulation of culturing cells.

These nanomaterial-based soft electronics can be transferred onto various types of biocompatible substrate. The substrate designed by 3D printer contains spatial advantage in culturing large number of cells within confined space,[12] and also can design the biological structure to mimic the native tissue condition[13,14] that the validity of toxicity testing can be increased. However, a simple integration of electronics on substrates prepared by a 3D printer still has some limitations such as lack of optimization of the substrate structure for preparing multi-layer cell-culture-platform,[15] in which the cells cultured on the lower substrate may die from hypoxia.[15,16] Moreover, the large-area multiplexing by an array of sensors and stimulators for electrophysiological applications in cell-culture-platform is not perfectly realized in previous studies yet.

In this context, we introduce multifunctional electronic-cell-culture-platform (ECCP) composed of three components including, i) patterned graphene oxide (GO) for promoting cellular activities, ii) an array of sensors and stimulators for monitoring and actuating electrophysiological signals from culturing cells, and iii) stackable and biocompatible polylactic acid (PLA) substrate designed by a 3D printer for mass production in culturing cells (**Figure 4.1a**). **Figure 4.1b** shows an exploded view of the individual

platform. The platform can be assembled into multi-layer because of the stackable structure in 3D-printed PLA substrate. Also, the mass production in cell culturing is viable due to the porous design in the substrate. An array of sensors and stimulators monitors and stimulates the activities of the cells cultured on the large area surface of the platform. This electronics on the cell-culture-platform can offer a new pathway in culturing various types of cells for cell therapy or *in vitro* toxicity test.

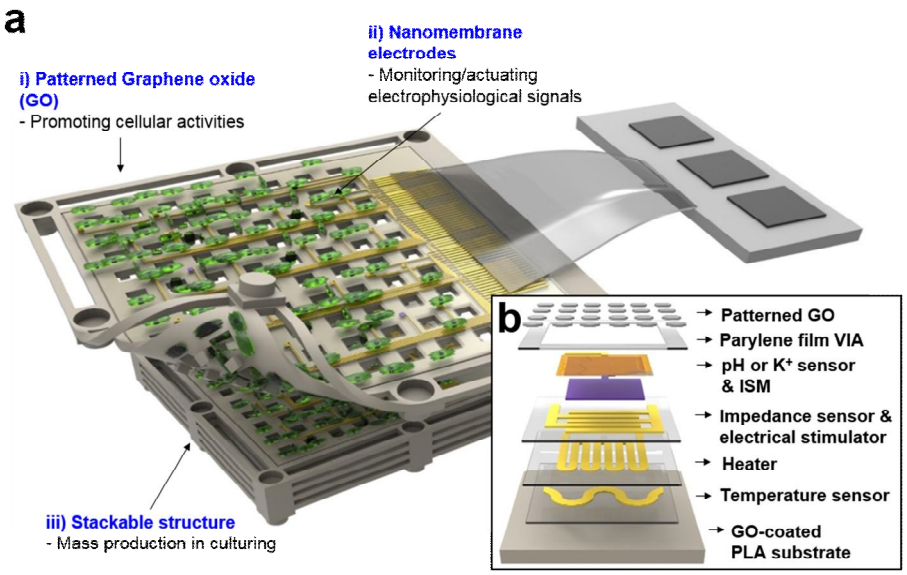

Figure 4.1 Schematic overview of the architecture of the electronic-cell-culture-platform

(a) The electronic-cell-culture-platform is composed of four types of sensors and two types of stimulators on a PLA substrate designed by a 3D printer. Top electronics and bottom polymer substrate are coated with graphene oxide for enhancing cellular activities. This platform have three key functions. (b) Expanded view of each element of the electronic-cell-culture-platform.

4.2 Results and Discussion

4.2.1 Optimization of substrate design

Optimizations of materials and structures of the substrate are important to fabricate multifunctional cell-culture-platform for culturing cells *in vitro*. PLA is a widely used polymer for the research in bioengineering due to its biocompatible and biodegradable properties.[17] While culturing cells on multi-layer substrates can be useful functions for producing numerous cells,[15,16,18] the structure of the substrate for the penetration of culturing medium to exchange gas or nutrient was not sufficiently optimized in previous studies. Recently, the performance of 3D printer has been dramatically increased to prepare a delicate polymer substrate with various types of polymers including biocompatible polymers.[13,19] Therefore, high resolution substrate made of biocompatible materials such as PLA can be designed by a 3D printer for scaffold or cell-culture-platform.

In this study, a biocompatible substrate composed of PLA is fabricated using a 3D printer to construct multifunctional ECCP (**Figure 4.2**). This substrate has seven concave holes and convex pillars on top and bottom planes at the edges so the substrate can be assembled into multi-layer

(**Figure 4.2a,b)**. The cubic pillars at the bottom side work as the structural support of the substrate. The substrate plane has an array of square-shaped pores which facilitate the penetration of medium at the space in between top and bottom substrates of multi-layer structure (**Figure 4.2c**). A monolayer of this substrate is 5 cm × 5 cm, with thickness of 2 mm.

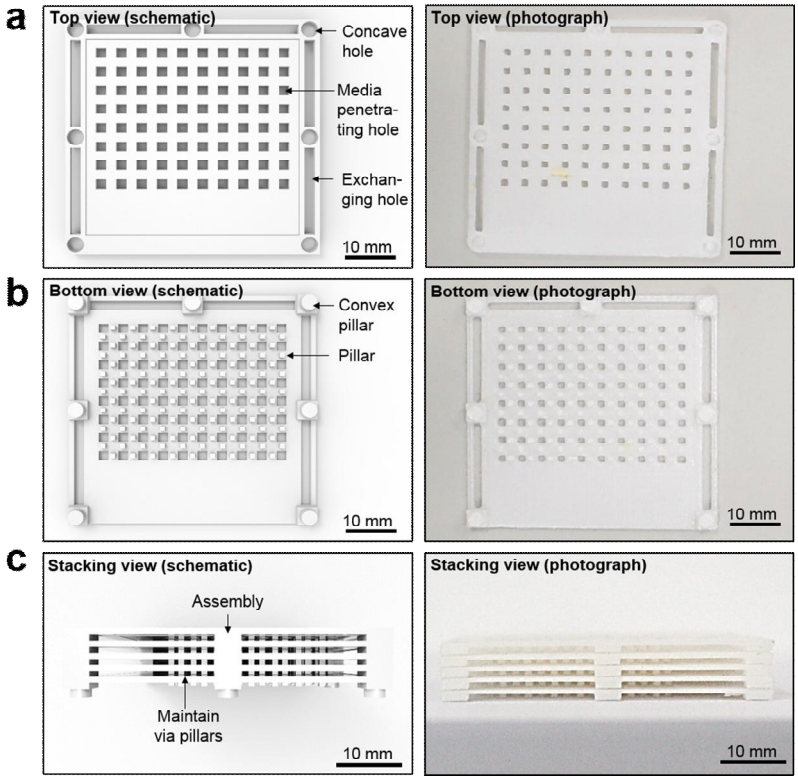

Figure 4.2 Schematic and photographic images for detailed designs of PLA substrates

(a) Top view of the PLA substrate prepared by a 3D printer. The substrate have an array of square holes for the penetration of culturing medium and cells. The concave holes are assembled with convex pillars of the bottom side. (b) Bottom view of the PLA substrate. An array of cubic pillars support each layer of electronic-cell-culture-platform. The convex pillar are assembled with concave holes of the top side to prepare the multi-layer platforms. (c) Side view of the stackable substrates.

4.2.2 Characterization of graphene oxide coated substrate

Recent studies reported that carbon nanomaterials including GO,[20,21] graphene,[22,23] and carbon nanotube[24] promote cellular activities of neural cell and muscle cell. There is no proven theory on how carbon nanomaterials promote cellular activity. However, physical, chemical, and electrical properties of surface materials may play critical roles in regulating the cellular activities. In this study, GO nanoparticle dispersed in ethanol is coated on top and bottom sides of 3D-printed substrate by spraying method[25] (**Figure 4.3a**). **Figure 4.3b** presents Raman spectrometer data of GO coating on PLA substrate.

The homogeneous distributions of GO particle coated on PLA substrate are also observed using atomic force microscope (AFM) and scanning electron microscope (SEM) (**Figure 4.3c,d**). The geometry and chemical/physical properties of surface GO enhance the adhesiveness of C2C12 myoblasts (**Figure 4.4**). Furthermore, the sprayed GO can be patterned into desired design using photolithography. The patterned GO on the soft electronics promote the guidance of cellular alignment and cellular activity.[26] Meanwhile, the lack of conductive property in GO prevents any hindrance on the functions of electronics integrated into ECCP.

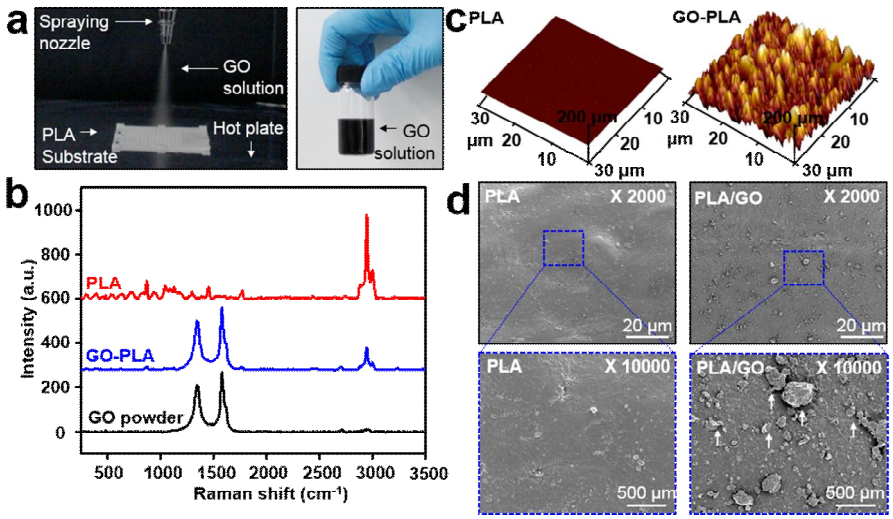

Figure 4.3 Characterization of graphene oxide

(a) Photographic images of experiment setups (left) and graphene oxide solution (right) for coating the graphene oxide on the PLA substrate. (b) Raman spectroscopy data of PLA (red), PLA coated with graphene oxide (GO-PLA; blue), and graphene oxide nanoparticles (GO powder; black). (c,d) Atomic force microscope (AFM) and scanning electron microscope (SEM) images of PLA and GO-PLA. The blue-dotted boxes show magnified views.

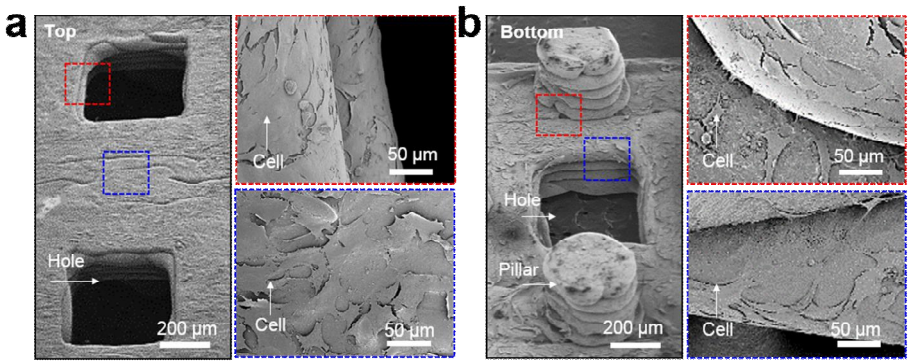

Figure 4.4 Biocompatibility of the PLA substrate coated with graphene oxide

(a) SEM image of C2C12 myoblasts on the top side of GO-PLA substrate. Cells homogeneously adhere on the both plane and hole. The top right red-dotted box shows magnified views of the cells adhered on hole side. The bottom right blue-dotted box shows magnified views of the cells adhered on top plane. (b) SEM image of C2C12 myoblasts on the bottom side of GO-PLA substrate. The top right red-dotted box shows magnified views of the cells adhered on pillar side. The bottom right blue-dotted box shows magnified views of the cells adhered on hole side.

4.2.3 Fabrication of electronic-cell-culture-platform

The fabrication process of ECCP is based on the photolithography and transfer printing technique. All fabrication procedures are graphically illustrated in **Figure 4.5**. An array of sensors including impedance (a total of 16 sensors), pH, potassium (K^+), and temperature sensors, and of stimulators including heater, and electrical stimulator is fabricated with patterned inorganic nanomaterials such as gold (Au) nanomembrane, iridium oxide (IrOx), PEDOT:PSS, and silver/silver chloride (Ag/AgCl) ink and encapsulated with parylene C membrane (An array of sensors are shown in **Figure 4.6**). The 30 nm Ni on a silicon wafer is deposited for sacrificial layer by thermal evaporator. Then, the encapsulation layer is coated with parylene film by CVD method, and then SU-8 film is spin-coated on top. The temperature sensor and heater are composed of 10 nm Cr and 150 nm Au. Other sensors and stimulators are fabricated with 7 nm Cr and 70 nm Au. Similar to the PLA substrate, the electronics are coated with GO nanoparticles by spraying method which is micro-patterned by photolithography for promoting the guidance of cellular alignment. After completing the fabrication of the electronics on Ni-deposited silicon wafer, Ni is etched away for transferring the electronics onto SAM-treated and GO-coated PLA substrate. Then, IrOx is electro-deposited on pH sensor after

connecting anisotropic conductive films (ACFs) to printed circuit boards (PCBs).[27] For K^+ sensor, ion-selective membrane is coated and the reference electrode which is composed of Ag/AgCl is covered with Polyvinyl butyral (PVB) membrane for stability.[28]

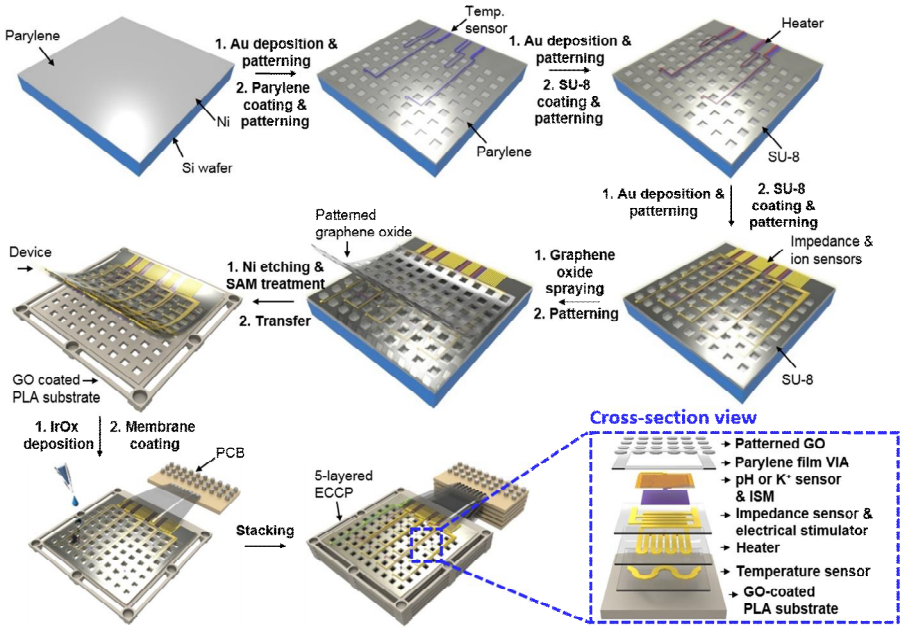

Figure 4.5 Detailed fabrication process of multifunctional electronic-cell-culture-platform

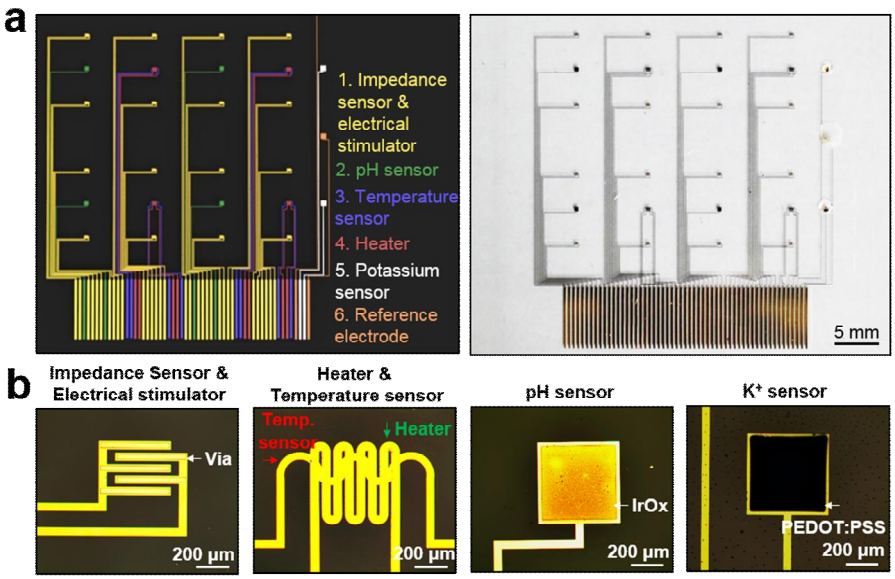

Figure 4.6 Design of sensors and stimulators integrated in the platform

(a) AutoCAD design (left) and photographic image (right) of whole sensors and stimulators of electronic-cell-culture-platform. (b) Microscope images of each sensors and stimulators. Impedance sensor/electrical stimulator (first frame) and heater/temperature sensor (second frame) are made of gold nanomembrane. pH and K^+ sensors (third and last frames) are composed of iridium oxide and PEDOT:PSS deposited by electrochemical reaction on the gold nanomembrane, respectively.

4.2.4 Characterizations and applications of individual sensors

The scheme in **Figure 4.7a** illustrates the measurement principle of sensors including pH, K^+ ion, and impedance sensors. The pH and K^+ ion sensors detect the changes of open circuit potential (OCP),[28,29] and impedance sensor detect the changes of electrolyte-electrode interface impedance in culture medium applied by alternating current (AC).[30] Controlling the pH in growth medium is important for maintaining the homeostasis continuously,[31] and K^+ concentration can affect the electrophysiological features including depolarizations and excitations of skeletal muscle cells. The pH and K^+ ion sensors are composed of Au electrode electroplated with IrOx and PEDOT:PSS, and coated with H^+ and K^+ ion selective membrane, respectively.[28,29] **Figure 4.7b,c** show the changes of relative OCP curves in each K^+ ion and pH sensor. The relative OCP is increased approximately 68% at decrease in pH from 7.94 to 6.94, and also increased approximately 40% at increase in K^+ concentration from 0.125 mM to 2 mM. This high resolution feature of measuring low potassium concentrations is suffice enough to measure the changes of potassium concentration in the extracellular culture medium (~5 mM).[32]

Figure 4.7d shows the change of pH during culturing cells, in

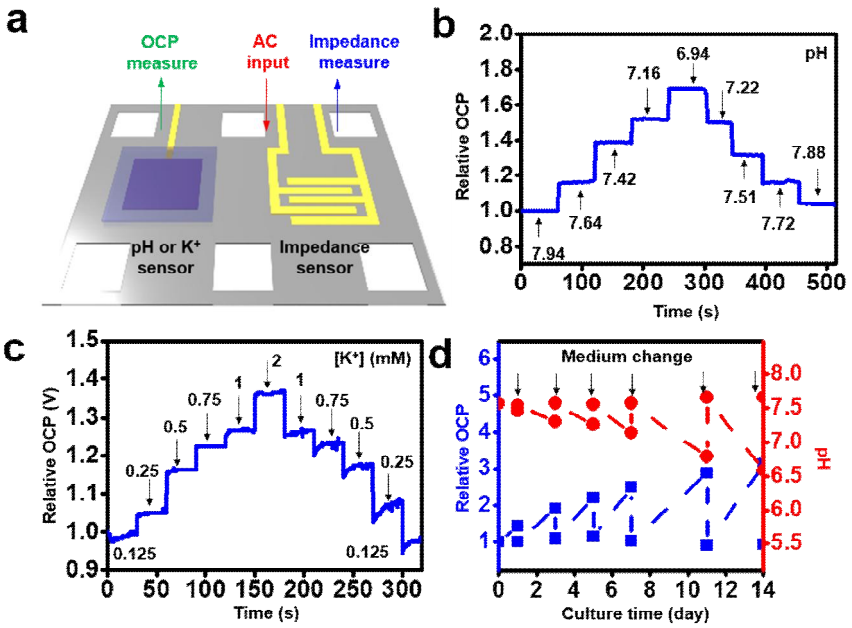

Figure 4.7 pH, K^+ and impedance sensors for monitoring the cellular physiology

(a) Schematic image of measuring method of pH, K^+ and impedance sensors integrated on a PLA substrate. (b,c) The open circuit potential (OCP) responses of the pH (b) and K^+ sensors (c). (d) Measuring pH changes during cluttering cells by both pH sensors of electronic-cell-culture-platform and commercial pH electrode.

which the change is even faster when the cells are proliferated. These extracellular pH changes are induced by changes in gas, ion, and molecular concentration from metabolic state.[33]

Figure 4.8a shows the calibration curve of impe dance sensor in growth medium. While culturing C2C12 myoblast and monitoring with an array of 16 impedance sensors, the impedance increase as the cells proliferate and decrease as the cells differentiate and form conducting tubular structure (**Figure 4.8b,c**). **Figure 4.8d** shows the monitoring of 4 different types of cells including C2C12 myoblast, mouse cardiac muscle cell (HL-1), human dermal fibroblast (hDFB), and human umbilical vein endothelial cells (HUVEC) with time-dependent impedance changes from array of 16 sensors at the given alternating current of 1.2 kHz. Similar to the impedance curve of C2C12 myoblast, the impedance of HL-1 cells increase and decrease during its proliferation and differentiation, respectively.[34] On the other hand, the curve for hDFB which does not form conducting tubular structure[35] and for HUVEC which form tight junctions continuously increased and saturated later.[36] The impedance data and its color map for an array of impedance sensors are shown in **Figure 4.9**.

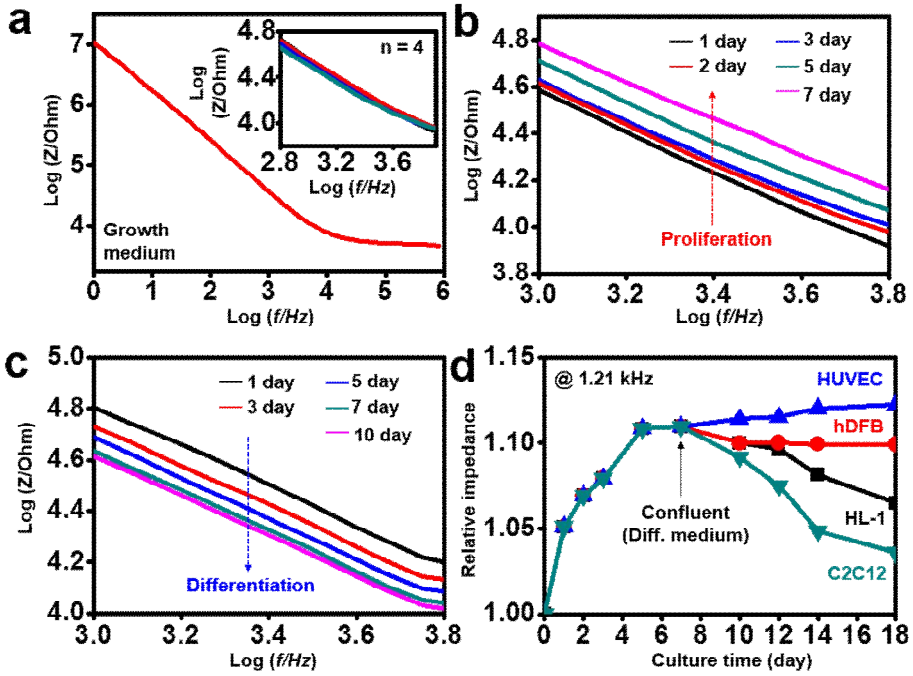

Figure 4.8 Impedance change during culturing cells

(a) Electrochemical characterization of the impedance sensor in the growth medium at 37 °C. Impedance curve measured from 1 Hz to 1 MHz with a bias voltage of 0.01 V. The inset shows the magnified view of the repeated measurements. (b,c) Impedance curve of C2C12 myoblasts according to the proliferation (b) and the differentiation procedures (c). (d) The time-dependent impedance curves of four types of cells including C2C12 myoblasts (C2C12), human dermal fibroblast (hDFB), mouse cardiac muscle cell (HL-1), and human umbilical vein endothelial cells (HUVEC) measured at 1.21 kHz during culture.

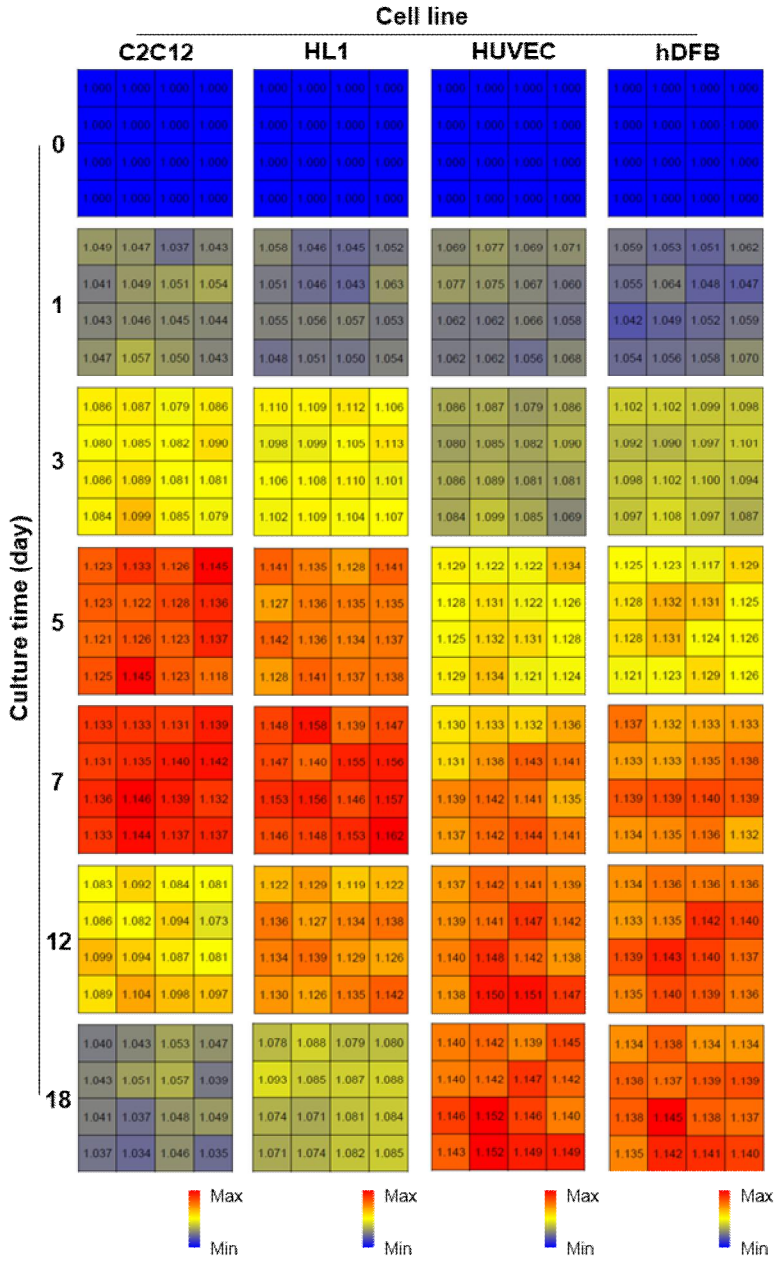

Figure 4.9 Mapping images of impedance data of four types of cells according to the proliferation and differentiation procedures

4.2.5 Characterizations and applications of individual stimulators

Thermal and electrical stimulations by the ECCP can enhance the cellular activities including proliferation and differentiation of skeletal muscle cells.[37,38] The schematic illustration in **Figure 4.10a** presents the measurement principles of heater, temperature sensor, and electrical stimulator. **Figure 4.10b** shows the calibration curve of heater which generates heat of 39 °C in 37 °C CO_2 incubator with the applied voltage of 10 V. The propagation of the heat generated by the heater can be diffused throughout the culturing medium and it can thermally stimulate cells cultured on one or multi-layered ECCP efficiently. **Figure 4.10c** shows the calibration curve of the resistive temperature detect which responds sensitively to the changes in temperature. The calibration curve of electrical stimulator is also presented in **Figure 4.10d**. **Figure 4.11a** schematically illustrates the controlled culture condition for C2C12 myoblast. Thermal stimulation (TS; 41 °C) and monophasic square wave pulse (ES; 3.3 V amplitude, 20 ms duration, and 1 Hz frequency) are applied onto C2C12 myoblast for 1 hour per day for 21 days. The impedance is monitored a day after cell was seeded, and fluorescent microscopy analysis is conducted 10 days later. The myotube formation is detected by immunostaining of myosin heavy chains (MHCs). Highly densed and elongated myotube can be found

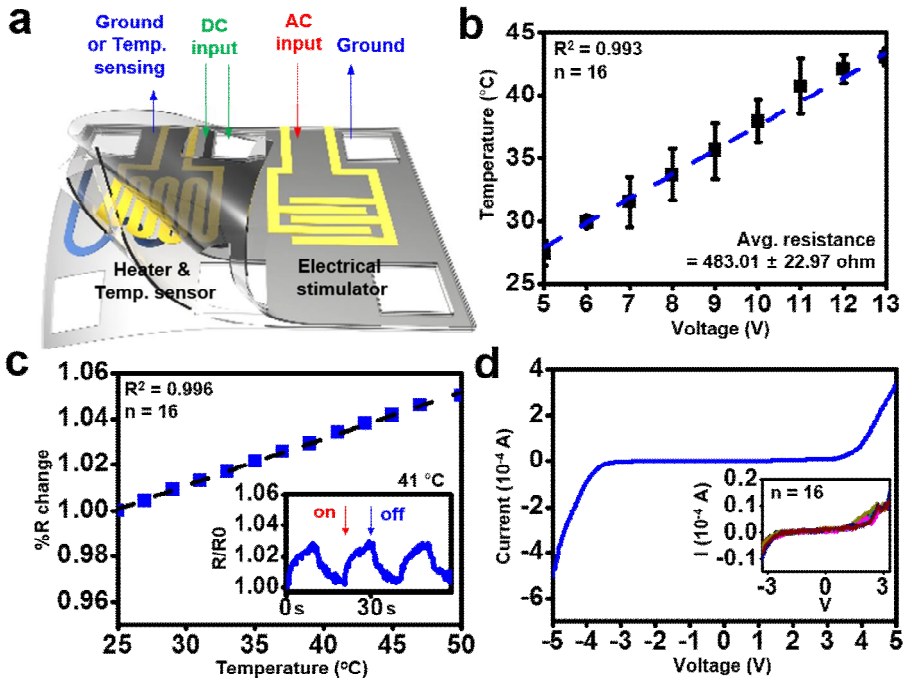

Figure 4.10 Temperature sensor and electrical/thermal stimulators for regulating the cellular physiology

(a) Schematic image of measuring method of temperature sensor, heater and electrical stimulator integrated on a PLA substrate. (b) Calibration curve of heater. (c) Calibration curve of temperature sensor: normalized resistance (% R change) as a function of temperature. The inset indicates the prompt changes of temperature sensor according to heating generated by heater. (d) Calibration curve of electrical stimulator. The inset shows the magnified view. Repeated measurements confirm the stability of the sensor.

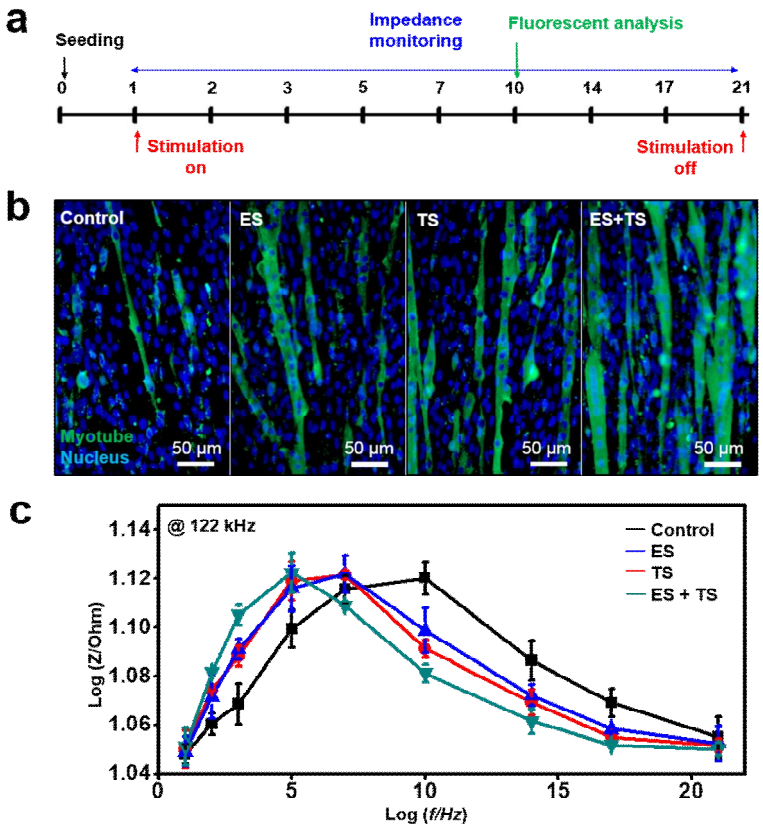

Figure 4.11 Electrical and thermal stimulation of C2C12 myoblasts

(a) Timetable of cell culture. Monophasic square wave pulses are applied with 3.3 V amplitude during 1 h for electrical stimulation (ES). 41 °C heat is applied during 1 h for thermal stimulation (TS). (b) Fluorescence microscope images of aligned and elongated myosin heavy chains of C2C12 myoblasts upon application of three different types of stimulation conditions. (c) The impedance values measured at 122 kHz as the three different stimulations are applied.

in the C2C12 myoblasts that were cultured with both TS and ES, simultaneously (**Figure 4.11b**). **Figure 4.11c** shows the impedance change of C2C12 myoblasts cultured with four different stimulation conditions. Under ES and TS, faster and greater impedance changes are observed.[37] While various ions and hydrated condition of culturing medium can decreases the performances of the integrated sensor and stimulators, the performances of those electronics do not show any hysteresis for 3 weeks in culturing medium at 37 °C (**Figure 4.12**).

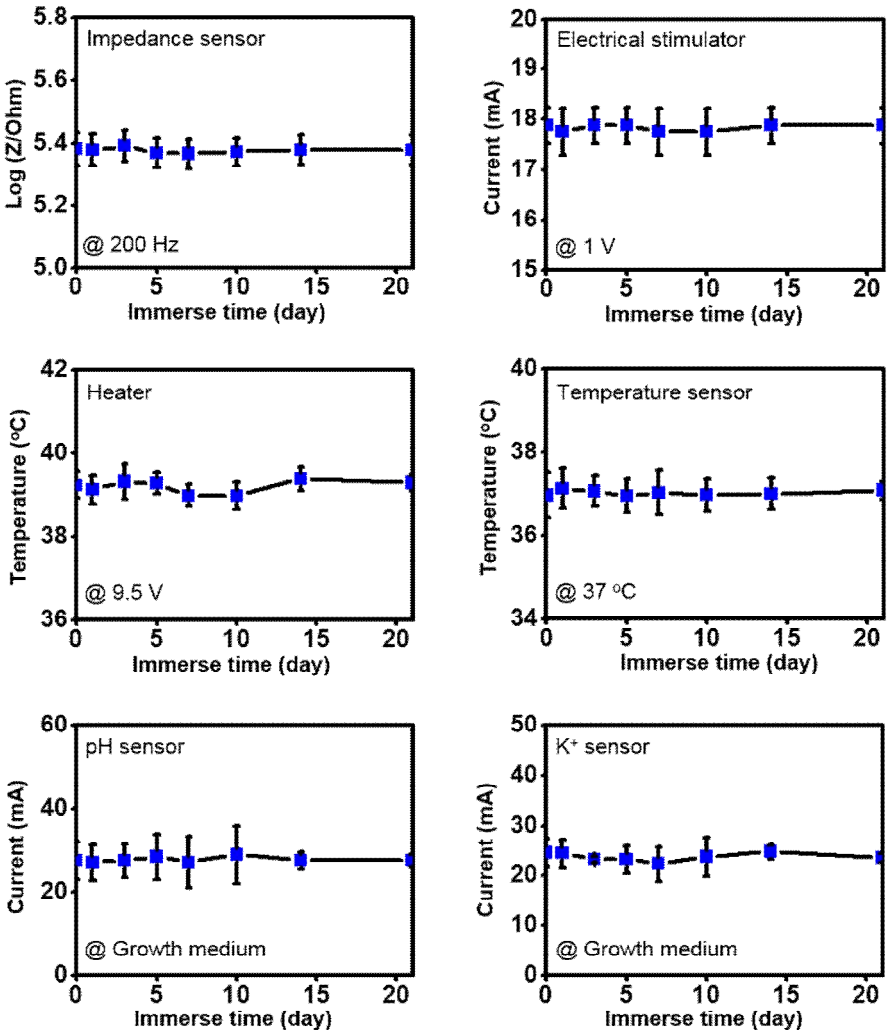

Figure 4.12 Stabilities of sensors and stimulators for 3 weeks. Minimum electrical and electrochemical hysteresis of all sensors and stimulators under immersing in culturing medium is advantage of cell-culture-platform.

4.2.6 Culturing cells on multi-layer platform

Multi-layered ECCP can be easily fabricated by assembling the layers of the ECCPs since the PLA substrate printed by a 3D printer have a stackable structure. Meanwhile, the penetration and depth of culturing medium during cell culturing *in vitro* is important to prevent any cell death by hypoxia. The cells in native tissue need to reside 100 ~ 200 μm between each capillaries for exchanging gas and nutrient.[39] In this study, we conducted an experiment to optimize a porous design, a number of layers, and the medium depth for the PLA substrate (**Figure 4.13a**). The viability of those cells cultured on the designed substrate for up to 5 layers is approximately ~95% (**Figure 4.13b,c**). However, the viability of the cells on the flat substrate (no porosity) is lower than 40%. Furthermore, the viability of cells is continuously decreased when the depth of media is increased for more than 10 mm (**Figure 4.13d**). These results show the porous design of the substrate in ECCP offers great viabilities and activities to culturing cells because the optimized design enable gas and nutrient to penetrate easily. Therefore, we designed our ECCP with a porous PLA substrate for 5 layers and 10 mm of media depth.

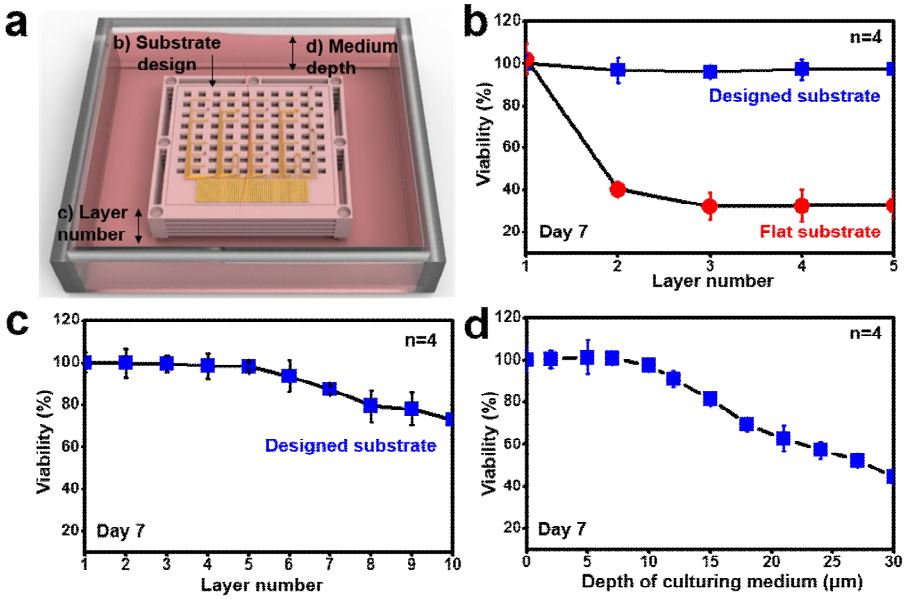

Figure 4.13 Optimization of 3D-printed PLA substrate for multi-layer culturing of C2C12 myoblasts

(a) Schematic image for specifying experiment condtions. (b) Changes cell viability according to substrate design and stacking layers (3D-printed and deisnged PLA substrate (Designed substrate); 3D-printed and flat PLA substrate (Flat substrate)). (b) Changes of cell viability according to stacking layers to ten layers. (c) Changes of cell viability according to medium depth from cells adhered onto the PLA substrate to surface of culturing medium.

4.2.7 Regulation of cellular activities on multi-layer platform

Figure 4.14a presents a scheme for culturing cells on 5-layered ECCP. The assembled 5-layered ECCP is placed on top of sterilized glass and contained within walls prepared by 10:1 PDMS. The impedance monitoring with four cases of stimulations (TS and ES on different points and layers) has been conducted on this multi-layered ECCP. **Figure 4.14b** shows the impedance change in culturing cells without any stimulation. The changes in impedance are similar throughout the platform. In other words, the speed of proliferation or differentiation was similar in all locations within the platform (**Figure 4.15**). The mapping images in **Figure 4.16a-d**, however, shows the different speed of proliferation and differentiation of culturing cells depends on the location of stimulation site. Furthermore, the cellular activities of cells cultured close to the TS site is also clearly promoted. The effectiveness of stimulation is gradually decreased as the distance from the stimulation site is increased. This controlled culturing of the cells, either stem cell or primary cell, may offer a solution to the problem of heterogeneous proliferation or differentiation of cells, especially in mass production in cell culturing.

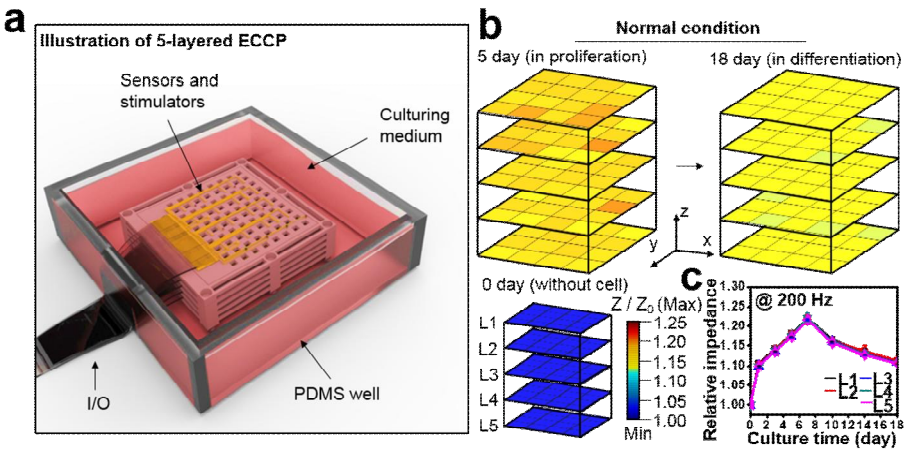

Figure 4.14 Construction of five-layered electronic-cell-culture-platform and culturing cells

(a) Schematic image of setups for monitoring and stimulation of cellular physiological activities by 5-layered electronic-cell-culture-platform. (b) Mapping images from impedance data of 5 and 18 days after culturing C2C12 myoblasts on the platform. Normalized impedance data are used for mapping images. (c) A plot of impedance changes of each layers from impedance data.

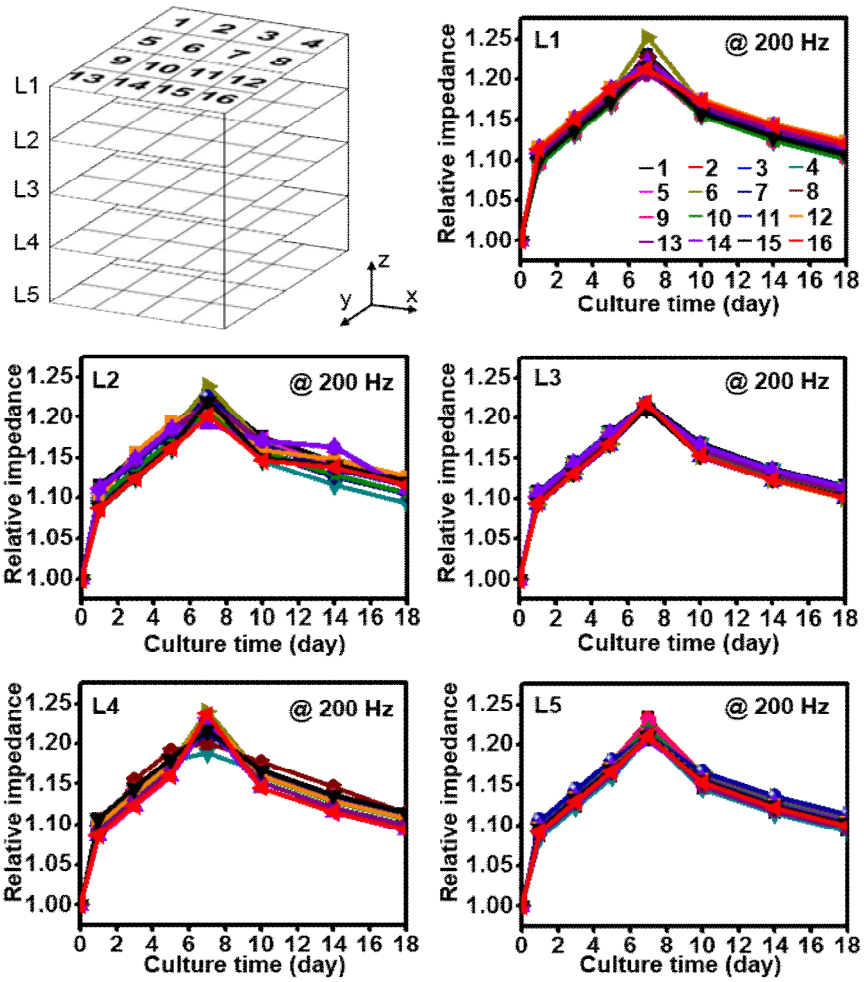

Figure 4.15 Plots of impedance changes from five-layered electronic-cell-culture-platform during culturing cells

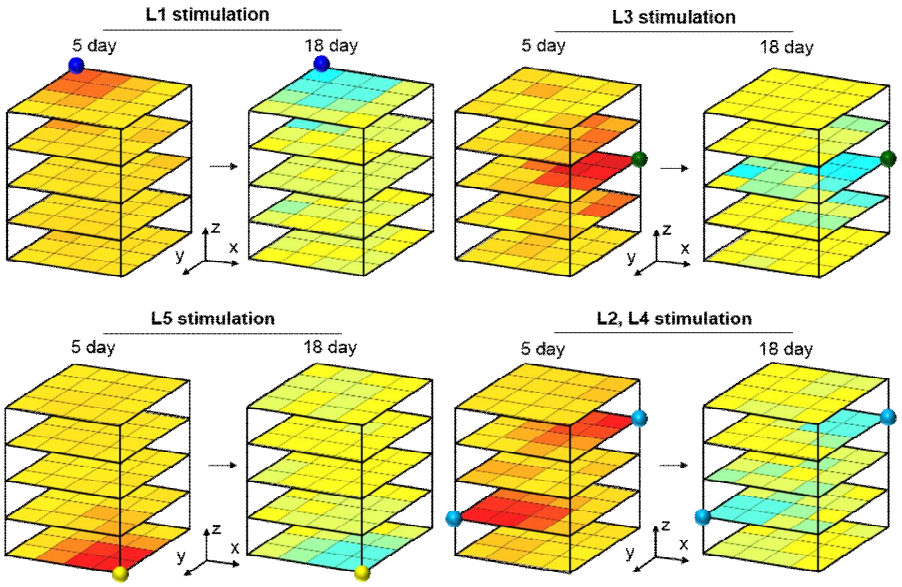

Figure 4.16 Electrical and thermal stimulation of C2C12 myoblasts cultured on the five-layered electronic-cell-culture-platform. Simultaneous and spatiotemporal stimulations using electrical and thermal stimulator on C2C12 myoblasts change impedance of each layer during cultured after 5 and 18 days.

4.3 Conclusion

Our multifunctional electronic-cell-culture-platform composed of an array of various types of sensors and stimulators transferred onto a biocompatible designed PLA substrate provides not only monitoring of cellular activities such as proliferation and differentiation but also stimulation of those activities. The GO nanoparticle coated on the polymer substrate and soft electronics enhance the biocompatibility and cellular affinity of the ECCP. High-performance sensors and stimulators can be sufficiently utilized for monitoring and stimulation of cellular electrophysiological properties. The platform can be assembled into multi-layer because of the stackable structure in 3D-printed PLA substrate and of the optimized porous design for enhancing the viabilities of culturing cells. These characteristics can provide mass production in cell culturing by an array of sensors and stimulators integrated in individual substrates. This electronics-based cell-culture-platform may offer a new pathway in culturing various types of useful cells for cell therapy or *in vitro* toxicity test.

4.4 Experimental

4.4.1 Characterization of graphene oxide

Graphene oxide (GO) nanoparticles were dispersed in absolute ethanol concentrated with 0.4 mg/mL by ultrasonicator for 2 h. And then, GO solution was smoothly sprayed onto the various substrates located on the hot plate under 120 ^{o}C heat. The coated substrate was cooled at room temperature for 30 minute. Raman spectroscopy was used for surface chemical analysis, in which the Raman spectrum were acquired under 30 s of Acq. Time and 1% of ND Filter. For observation of surface morphology of GO coated PLA, an atomic force microscope (AFM, Dimension Icon, Bruker) and a scanning electron microscope (SEM, SUPRA 55VP, Carl Zeiss) analysis were conducted. All AFM experiments were conducted in tapping mode, and all SEM experiments were conducted after 20 nm Pt coating.

4.4.2 Cell culturing

C2C12 myoblasts (CRL-1772; ATCC), human dermal fibroblasts (PCS-201-012; ATCC), HL-1 cardiac muscle cells (Inha university), and human umbilical vein endothelial cells (Lonza) were used for experiments.

C2C12 myoblasts were cultured in two types of media: proliferation medium composed of Dulbecco's modified Eagle's medium (DMEM) supplemented with 10% fetal bovine serum (FBS, Gibco) and 1% penicillin-streptomycin (PS, Gibco); and differentiation medium (to induce myotube formation) composed of DMEM supplemented with 5% horse serum (HS, Gibco) and 1% PS. Human dermal fibroblasts were cultured in DMEM supplemented with 10% FBS and 1% PS. HL-1 cardiac muscle cells were cultured in calycomb medium (Sigma Aldrich) supplemented with 10% FBS and 1% PS. human umbilical vein endothelial cells were cultured in EGM^{TM} growth medium (Lonza). The cells were cultured under the standard culture conditions of 37 °C and 5% CO_2.

4.4.3 Characterization of cellular properties

To observe the myotube formation, the C2C12 myoblasts were immunostained with anti-myosin heavy chain antibodies (1:100 dilution; Abcam) and Alexa Fluor 488 donkey anti-mouse IgG (1:100 dilution; Abcam). DAPI (Vector) is also stained to observe the nucleus of cells. The stained samples were observed and captured by a fluorescence microscope (Eclipse Ti, Nikon). The images were analyzed by Image-Pro Plus software (Media Cybernetics).

4.4.3 Cellular viability test

MTT assay was conducted to observe the viability of culturing cells. Cells were cultured in MTT solution (0.5 mg/mL in growth medium) for 3 h in an incubator under standard culture conditions, in which culturing cells formed MTT formazan. Subsequently, the solution was replaced by DMSO, and then the formazan was dissolved. The absorbance values was measured with multiplate reader at 540 nm wavelength.

4.4.4 Electrochemical analysis

Impedance and open circuit potential were measured by electrochemical workstation (CHI660E, CH Instruments). Measurement of impedance was conducted with two-electrode configuration (0.05 V for amplitude), and open circuit potential was also conducted with two-electrode configuration (IrOx electrode and Ag/AgCl electrode). The impedance data were processed and transferred for drawing color map using MATLAB software (MathWorks).

4.4.5 Electrical analysis

For electrical stimulation, monophasic square wave pulses were

applied to culturing C2C12 myoblasts *via* the Au electrode. The parameters of the pulses, including frequency, duration, and amplitude were controlled by a function generator (33500B, Agilent Technologies). For thermal stimulation, the parameters including amplitude of voltage or current were confirmed by IR thermometer. During electrical and thermal stimulations, the cells were cultured in an incubator under standard culture conditions. For monitoring the impedance changes, the electrodes were connected and measured using an electrochemical workstation (CHI660E, CH Instruments).

4.5 References

1. Trounson, A. & McDonald, C. Stem cell therapies in clinical trials: progress and challenges. *Cell Stem Cell.* **17**, 11-22 (2015).
2. Dimmeler, S., Ding, S., Rando, T, A. & Trounson, A. Translational strategies and challenges in regenerative medicine. *Nat. Med.* **20**, 814-821 (2014).
3. Huh, D., Leslie, D, C., Matthews, B, D., Fraser, J, P., Jurek, S., Hamilton, G, A., Thorneloe, K, S., McAlexander, M, A. & Ingber, D, E. A human disease model of drug toxicity-induced pulmonary edema in a lung-on-a-chip microdevice. *Sci. Transl. Med.* **4**, 159ra147 (2012).
4. Huh, D., Matthews, B, D., Mammoto, A., Montoya-Zavala, M., Hsin, H, Y. & Ingber, D, E. Reconstituting organ-level lung functions on a chip. *Science* **328**, 1662-1668 (2010).
5. Park, Y, H., Yun, J, I., Han, N, R., Park, H, J., Ahn, J, Y., Kim, C., Choi, J, H., Lee, E., Lim, J, M. & Lee, S, T. Mass production of early-stage bone-marrow-derived mesenchymal stem cells of rat using gelatin-coated matrix. *Biomed. Res. Int.* **2013**, 347618 (2013).
6. Kesavan, S, V., Momey, F., Cioni, O., David-Watine, B., Dubrulle, N., Shorte, S., Sulpice, E., Freida, D., Chalmond, B., Dinten, J, M., Gidrol, X. & Allier, C. High-throughput monitoring of major cell functions by means

of lensfree video microscopy. *Sci. Rep.* **4**, 5942 (2014).

7. Guez, J, S., Cassar, J, P., Wartelle, F., Dhulster, P. & Suhr, H. Real time in situ microscopy for animal cell-concentration monitoring during high density culture in bioreactor. *J. Biotechnol.* **111**, 335-343 (2004).
8. Yao, C., Li, Q., Guo, J., Yan, F. & Hsing, I, M. Rigid and flexible organic electrochemical transistor arrays for monitoring action potentials from electrogenic cells. *Adv. Healthc. Mater.* **4**, 528-33 (2015).
9. Kim, T, H., Kwon, C, H., Lee, C., An, J., Phuong, T, T., Park, S, H., Lima, M, D., Baughman, R, H., Kang, T, M. & Kim, S, J. Bio-inspired hybrid carbon nanotube muscles. Sci. Rep. 6, 26687 (2016).
10. Tian, B., Liu, J., Dvir, T., Jin, L., Tsui, J, H., Qing, Q., Suo, Z., Langer, R., Kohane, D, S. & Lieber, C, M. Macroporous nanowire nanoelectronic scaffolds for synthetic tissues. *Nat. Mater.* **11**, 986-994 (2012).
11. Dai, X., Zhou, W., Gao, T., Liu, J. & Lieber, C, M. Three-dimensional mapping and regulation of action potential propagation in nanoelectronics-innervated tissues. *Nat. Nanotechnol.* **11**, 776-782 (2016).
12. Hong, S., Sycks, D., Chan, H, F., Lin, S., Lopez, G, P., Guilak, F., Leong, K, W. & Zhao, X. 3D printing of highly stretchable and tough hydrogels into complex, cellularized structures. *Adv. Mater.* **27**, 4034 (2015).
13. Do, A, V., Khorsand, B., Geary, S, M. & Salem, A, K. 3D Printing of

Scaffolds for Tissue Regeneration Applications. *Adv. Healthc. Mater.* **4**, 1742-1762 (2015).

14. Kang, H, W., Lee, S, J., Ko, I, K., Kengla, C., Yoo, J, J. & Atala, A. A 3D bioprinting system to produce human-scale tissue constructs with structural integrity. *Nat. Biotechnol.* **34**, 312-319 (2016).

15. Pirlo, R, K., Wu, P., Liu, J. & Ringeisen, B. PLGA/hydrogel biopapers as a stackable substrate for printing HUVEC networks via BioLP. *Biotechnol. Bioeng.* **109**, 262-273 (2012).

16. Derda, R., Tang, S, K., Laromaine, A., Mosadegh, B., Hong, E., Mwangi, M., Mammoto, A., Ingber, D, E. & Whitesides, G, M. Multizone paper platform for 3D cell cultures. *PLoS One.* **6**, e18940 (2011).

17. Serra, T., Mateos-Timoneda, M, A., Planell, J, A. & Navarro, M. 3D printed PLA-based scaffolds: a versatile tool in regenerative medicine. *Organogenesis.* **9**, 239-244 (2013).

18. Simon, K, A., Park, K, M., Mosadegh, B., Subramaniam, A, B., Mazzeo, A, D., Ngo, P, M. & Whitesides, G, M. Polymer-based mesh as supports for multi-layered 3D cell culture and assays. *Biomaterials.* **35**, 259-268 (2014).

19. Pati, F., Ha, D, H., Jang, J., Han, H, H., Rhie, J, W. & Cho, D, W. Biomimetic 3D tissue printing for soft tissue regeneration. *Biomaterials.*

62, 164-175 (2015).

20. Kim, J., Choi, K, S., Kim, Y., Lim, K, T., Seonwoo, H., Park, Y., Kim, D, H., Choung, P, H., Cho, C, S., Kim, S, Y., Choung, Y, H. & Chung, J, H. Bioactive effects of graphene oxide cell culture substratum on structure and function of human adipose-derived stem cells. *J. Biomed. Mater. Res. A.* **101**, 3520-3530 (2013).

21. Jeong, J, T., Choi, M, K., Sim, Y., Lim, J, T., Kim, G, S., Seong, M, J., Hyung, J, H., Kim, K, S., Umar, A. & Lee, S, K. Effect of graphene oxide ratio on the cell adhesion and growth behavior on a graphene oxide-coated silicon substrate. *Sci. Rep.* **6**, 33835 (2016).

22. Li, N., Zhang, Q., Gao, S., Song, Q., Huang, R., Wang, L., Liu, L., Dai, J., Tang, M. & Cheng, G. Three-dimensional graphene foam as a biocompatible and conductive scaffold for neural stem cells. *Sci. Rep.* **3**, 1604 (2013).

23. Solanki, A., Chueng, S, T., Yin, P, T., Kappera, R., Chhowalla, M. & Lee, K, B. Axonal alignment and enhanced neuronal differentiation of neural stem cells on graphene-nanoparticle hybrid structures. *Adv. Mater.* **25**, 5477-5482 (2013).

24. Fabbro, A., Prato, M. & Ballerini, L. Carbon nanotubes in neuroregeneration and repair. *Adv. Drug Deliv. Rev.* **65**, 2034-2044 (2013).

25. Son, D., Chae, S, I., Kim, M., Choi, M, K., Yang, J., Park, K., Kale, V, S., Koo, J, H., Choi, C., Lee, M., Kim, J, H., Hyeon, T. & Kim, D, H. Colloidal synthesis of uniform-sized molybdenum disulfide nanosheets for wafer-scale flexible nonvolatile memory. *Adv. Mater.* **28**, 9326-9332 (2016).

26. Yang, K., Lee, J., Lee, J, S., Kim, D., Chang, G, E., Seo, J., Cheong, E., Lee, T. & Cho, S, W. Graphene oxide hierarchical patterns for the derivation of electrophysiologically functional neuron-like cells from human neural stem cells. *ACS Appl. Mater. Interfaces* **8**, 17763-17774 (2016).

27. Son, D., Lee, J., Qiao, S., Ghaffari, R., Kim, J., Lee, J, E., Song, C., Kim, S, J., Lee, D, J., Jun, S, W., Yang, S., Park, M., Shin, J., Do, K., Lee, M., Kang, K., Hwang, C, S., Lu, N., Hyeon, T. & Kim, D, H. Multifunctional wearable devices for diagnosis and therapy of movement disorders. *Nat. Nanotechnol.* **9**, 397-404 (2014).

28. Gao, W., Emaminejad, S., Nyein, H, Y., Challa, S., Chen, K., Peck, A., Fahad, H, M., Ota, H., Shiraki, H., Kiriya, D., Lien, D, H., Brooks, G, A., Davis, R, W. & Javey, A. Fully integrated wearable sensor arrays for multiplexed in situ perspiration analysis. *Nature* **529**, 509-514 (2016).

29. Chung, H, J., Sulkin, M, S., Kim, J, S., Goudeseune, C., Chao, H, Y.,

Song, J, W., Yang, S, Y., Hsu, Y, Y., Ghaffari, R., Efimov, I, R. & Rogers, J, A. Stretchable, multiplexed pH sensors with demonstrations on rabbit and human hearts undergoing ischemia. *Adv. Healthc. Mater.* **3**, 59-68 (2014).

30. Bagnaninchi, P, O. & Drummond, N. Real-time label-free monitoring of adipose-derived stem cell differentiation with electric cell-substrate impedance sensing. *Proc. Natl. Acad. Sci. U. S. A.* **108**, 6462-6467 (2011).
31. Khajah, M, A., Mathew, P, M., Alam-Eldin, N, S. & Luqmani, Y, A. Bleb formation is induced by alkaline but not acidic pH in estrogen receptor silenced breast cancer cells. *Int. J. Oncol.* **46**, 1685-1698 (2015).
32. Engblom, A, C., Johansen, F, F. & Kristiansen, U. Actions and interactions of extracellular potassium and kainate on expression of 13 gamma-aminobutyric acid type A receptor subunits in cultured mouse cerebellar granule neurons. *J. Biol. Chem.* **278**, 16543-16550 (2003).
33. Naciri, M., Kuystermans, D. & Al-Rubeai, M. Monitoring pH and dissolved oxygen in mammalian cell culture using optical sensors. *Cytotechnology* **57**, 245-250 (2008).
34. Bloch, L., Ndongson-Dongmo, B., Kusch, A., Dragun, D., Heller, R. & Huber, O. Real-time monitoring of hypertrophy in HL-1 cardiomyocytes by impedance measurements reveals different modes of growth. *Cytotechnology* **68**, 1897-1907 (2016).

35. Moyer, K, E. & Ehrlich, H, P. Modulation of human fibroblast gap junction intercellular communication by hyaluronan. *J. Cell Physiol.* **196**, 165-170 (2003).

36. Bazzoni, G. & Dejana, E. Endothelial cell-to-cell junctions: molecular organization and role in vascular homeostasis. *Physiol. Rev.* **84**, 869-901 (2004).

37. Yamaguchi, T., Suzuki, T., Arai, H., Tanabe, S. & Atomi, Y. Continuous mild heat stress induces differentiation of mammalian myoblasts, shifting fiber type from fast to slow. *Am. J. Physiol. Cell Physiol.* **298**, C140-148 (2010).

38. Park, H., Bhalla, R., Saigal, R., Radisic, M., Watson, N., Langer, R. & Vunjak-Novakovic, G. Effects of electrical stimulation in C2C12 muscle constructs. *J. Tissue. Eng. Regen. Med.* **2**, 279-287 (2008).

39. Lovett, M., Lee, K., Edwards, A. & Kaplan, D, L., Vascularization strategies for tissue engineering. *Tissue Eng.Part B Rev.* **15**, 353-370 (2009).

Bibliography

1. Multifunctional Cell-Culture Platform for Aligned Cell Sheet Monitoring, Transfer Printing, and Therapy

Seok Joo Kim$^{\perp}$, Hye Rim Cho$^{\perp}$, Kyoung Won Cho$^{\perp}$, Shutao Qiao, Jung Soo Rhim, Min Soh, Taeho Kim, Moon Kee Choi, Changsoon Choi, Inhyuk Park, Nathaniel S. Hwang, Taeghwan Hyeon, Seung Hong Choi*, Nanshu Lu*, and Dae-Hyeong Kim* ($^{\perp}$equal contribution)

ACS Nano ***9***, 2677-2688 (2015)

2. Stretchable and Transparent Biointerface Using Cell-Sheet-Graphene Hybrid for Electrophysiology and Therapy of Skeletal Muscle

Seok Joo Kim$^{\perp}$, Kyoung Won Cho$^{\perp}$, Hye Rim Cho, Liu Wang, Sung Young Park, Seung Eun Lee, Taeghwan Hyeon, Nanshu Lu, Seung Hong Choi*, Dae-Hyeong Kim* ($^{\perp}$equal contribution)

Advanced Functional Materials ***26,*** 3207-3217 (2016)

초 록 (Abstract in Korean)

유연 전자 소자가 융합된 다기능성 세포 배양 기판 개발과 전기생리학적 활용

최근 유연전자 소자의 발전과 함께 조직공학 및 재생의학 분야에 있어서 기존에 개발된 다양한 종류의 생체 재료와의 융합을 통해 차세대 세포배양 및 이식용 지지체 개발을 위한 연구가 활발히 진행되고 있다. 생체 조직에 적합한 낮은 기계적 특성으로 인해 세포 배양 시 세포의 증식과 분화의 활성을 조절할 수 있고, 이식 시에는 굴곡진 생체조직 표면에 잘 달라 붙음으로써 높은 수준의 전기생리학적 신호를 주고받을 수 있는 장점과 더불어 세포 시트 치료 효과 극대화의 특징을 가진다. 본 논문에서는 생체 안정한 고분자 기판 위에 다양한 유·무기 물질을 이용해 제작된 유연 전자 소자를 융합하여 세포 배양 및 이식에 적합한 다기능성 세포배양 지지체를 개발하는 것을 목표로 한다. 먼저 손상된 근육의 세포 치료에 적합한 근육 세포시트를 제작하고 트랜스퍼 프린팅 하기 위한 유연 전자 소자 융합 세포 배양용 지지체에 대해 다룬다. 이러한 소자는 생체 안정한 고분자 고무 위에 임피던스 및 온도

센서가 구성되어 있고, 그 위에 그래핀 나노리본이 구성된다. 그래핀 나노리본에 의해 촉진된 근육 세포의 증식과 분화 상태를 임피던스 센서를 통해 실시간으로 확인하고, 온도 센서를 통해 체온의 변화를 확인하며 세포시트의 생체 내 이식을 통해 세포 치료 가능성을 확인하였다. 다음으로 근육에 직접 이식이 가능한 근육 세포시트가 코팅된 그래핀 전극에 대해 다룬다. 이러한 소자는 유연한 고분자 고무 위에 구불구불한 표면의 고분자 필름 및 그래핀 전극으로 구성되어 있고, 상단에 일방향으로 배열된 세포시트가 구성되어 있다. 세포로 인해 근육 조직과의 높은 계면 상태를 형성함으로써, 그래핀 전극을 통한 효율적인 전기적 신호 자극 및 확인이 가능하며, 동시에 배양된 세포시트를 통한 조직 재생의 가능성을 확인하였다. 마지막으로 다양한 센서 및 자극기가 접목되어있는 다기능성 전자 세포배양기판에 대해 다룬다. 이러한 소자는 배열된 다수의 센서와 자극기로 인해 세포의 활성을 대면적에서 조절하며 배양할 수 있을뿐만 아니라, 조립 가능한 기판으로 인해 효과적인 3차원 세포배양이 가능함을 확인하였다.

주요어: 유연한, 늘어날 수 있는, 전자 소자, 세포배양지지체, 그래핀, 트랜스퍼프린팅, 세포치료

학 번: 2012-31298